

Binary Mixtures Near Solid Surfaces: Wetting and Confinement Phenomena

Von
Diplom-Physiker Dirk Woywod
Demmin

von der Fakultät II - Mathematik und Naturwissenschaften
der Technischen Universität Berlin
zur Erlangung des akademischen Grades

Doktor der Naturwissenschaften
- Dr. rer. nat. -

genehmigte Dissertation.

Prüfungsausschuss

Vorsitzender: Prof. Dr. Reinhard Schomäcker
1. Bericht: Prof. Dr. Martin Schoen
2. Bericht: Prof. Dr. Gerhard H. Findenegg

Tag der mündlichen Prüfung: 10. Dezember 2004

Berlin 2004

D 83

Abstract – German

In dieser Dissertation wird das Phasenverhalten von zweikomponentigen Fluiden im freien Volumen, in Kontakt mit einer homogenen planaren Wand sowie zwischen zwei parallelen Wänden (Schlitzpore) untersucht. Diese Arbeit ist in drei Teile gegliedert.

Der erste Teil beschreibt das verwendete Modell. Ausgehend vom Gittergasmodell wird mit Hilfe der Molekularfeldnäherung ein expliziter Ausdruck der Dichte des großkanonischen Potentials ω hergeleitet, das sowohl von den thermodynamischen Variablen (Temperatur T , Porenweite n_z , chemische Potentiale μ und $\Delta\mu$) und den Wechselwirkungsstärken der Teilchen als auch von den lokalen Dichten der beiden Mischungskomponenten abhängt. Für feste Modellparameter lassen sich durch numerische Minimierung von ω die lokalen Dichten thermodynamisch stabiler Phasen im Gleichgewicht berechnen und so Phasenübergänge sowie die räumliche Struktur der Mischungen bestimmen.

Der zweite Teil behandelt die Ergebnisse theoretischer Studien. Im freien Volumen lassen sich binäre Mischungen je nach Größe der Wechselwirkung zwischen verschiedenartigen Teilchen in drei topologisch verschiedene Typen einteilen. Alle Typen zeigen ein reiches Phasenverhalten im dreidimensionalen Zustandsraum (T - μ - $\Delta\mu$), das in dieser Art noch nicht untersucht wurde. Jedoch stimmen die Ergebnisse mit früheren Studien symmetrischer Mischungen (d.h. $\Delta\mu = 0$) sehr gut überein.

Binäre Gasmischungen in Kontakt mit einer planaren, nichtselektiven Wand weisen eine Vielzahl von Adsorptionsphänomenen auf. Einerseits hängt die Dicke der adsorbierten Filme ähnlich wie bei den einkomponentigen Fluiden von der Stärke der Wandattraktion ϵ_w ab. Andererseits bestimmt der Mischungstyp die Art der Phasenübergänge von ge- zu entmischten Filmen. Zusätzlich werden die Bedingungen für vollständige Benetzung (makroskopisch dicker Film) systematisch untersucht.

Weiterhin werden symmetrische Mischungen in nicht-selektiven Schlitzporen betrachtet. Der durch n_z und ϵ_w charakterisierte Begrenzungseffekt führt zur erwarteten Kapillarkondensation und zur Absenkung der kritischen Gas-Flüssig-Temperatur. Es verändern sich aber auch Struktur und Charakter der flüssigen Phasen: kleine Porenweiten implizieren spontane Entmischung und stark anziehende Porenwände führen sogar zu einer Veränderung des Mischungstyps.

Im dritten Teil werden zwei experimentelle Systeme flüssiger Mischungen in porösen Gläsern (CPG-10) unterschiedlicher Porenweiten modelliert. Zunächst werden die begrenzungsunabhängigen Modellparameter mit Hilfe der experimentellen Ergebnisse im freien Volumen individuell angepasst. Das Konzept des hydraulischen Radius erlaubt es dann, Porenweiten und -geometrien von Modell und Experiment miteinander zu verknüpfen. Die guten Übereinstimmungen zwischen experimentellen Daten und theoretischen Voraussagen zeigen, dass das Modell das Phasenverhalten der Mischungen qualitativ sehr gut reflektiert. Darüberhinaus liefert das Modell die mikroskopische Struktur und erleichtert somit die Interpretation der experimentellen Resultate.

Abstract – English

In this thesis we study the phase behavior of binary fluid mixtures in bulk, near a single solid surface, and confined between two parallel surfaces (slit pore). The thesis is divided into three parts.

Part I introduces a lattice-fluid model. Based upon a mean-field approximation we obtain a closed expression for the density of the grand potential energy ω which depends not only on thermodynamic variables (i.e., temperature T , pore width n_z , chemical potentials μ and $\Delta\mu$) and strengths of intermolecular interactions between the fluid molecules but also on the local densities of the two constitute components of the mixture. For fixed model parameters a subsequent numerical minimization of ω yields the local densities of the thermodynamically stable phase and thus permits us to compute phase transitions and spacial structure of the mixture.

Part II concerns the results of our theoretical studies. In the bulk we find three topologically different types of mixtures depending on the interaction strength between unlike molecules. All three types exhibit a rich phase behavior in the three-dimensional state space (T - μ - $\Delta\mu$) which has not yet been reported in the literature. However, our results are supported by earlier studies of symmetric mixtures for which $\Delta\mu = 0$.

If the gas phase of a binary mixture is in contact with a single nonselective solid substrate, we observe a number of adsorption phenomena. Similar to one-component fluids the thickness of adsorbed films strongly depends on the strength of the fluid–substrate attraction ϵ_w . In addition, the type of the mixture triggers the character and the order of phase transitions from mixed to demixed films. Moreover, criteria for complete wetting to occur are systematically established.

If symmetric binary mixtures are confined to nonselective slit pores we find the expected capillary condensation of the gas phase as well as the depression of the critical gas+mixed liquid temperature. However, the structure and the nature of liquid phases depend on the degree of confinement (i.e., n_z and ϵ_w) so that small pore widths lead to a spontaneous decomposition whereas strongly attractive substrates may even change the type of the mixture.

In Part III we employ our model to two experimental binary mixtures confined to mesoporous matrices (CPG-10). Confinement-independent model parameters are adjusted that the bulk system matches its experimental counterpart as much as possible. By introducing a concept of the hydraulic radius we can link pore widths and pore geometries of the model and of the experimental system. We show that, on the one hand, our model is capable of describing the phase behavior of asymmetric mixtures at least at a qualitative level. On the other hand, the microscopic picture obtained from our theoretical analysis assists the interpretation of the experimental findings.

Contents

1	Introduction	9
I	Theory	15
2	Model	17
2.1	Lattice Fluid	17
2.1.1	Occupation Matrix	17
2.1.2	Hamiltonian	19
2.2	Mean-Field Approximation	21
2.2.1	Hamiltonian and Partition Function	21
2.2.2	Thermodynamic Limit	22
2.2.3	Fluid-Substrate Potential	25
2.3	Units	26
2.4	Phase Coexistence	26
2.4.1	Thermodynamic Conditions	26
2.4.2	Order of Phase Transitions	27

2.4.3	Gibbs' Phase Rule and Dimensionality	28
3	Numerical Treatment	29
3.1	Conditions for Stable Phases	29
3.1.1	Vanishing Temperature	30
3.1.2	Non-Vanishing Temperature	30
3.2	Conditions for Phase Coexistence	31
3.3	Numerical Procedure	32
3.3.1	Starting Solutions at Zero Temperature	32
3.3.2	Search for Stable Phases	33
II	Theoretical Studies	35
4	Bulk Systems	37
4.1	Pure Fluid and Calibration	38
4.1.1	Parameters	38
4.1.2	Pure Fluid	39
4.1.3	Calibration of Critical Points	40
4.2	Phase Behavior of Bulk Mixtures	41
4.2.1	Almost Pure	42
4.2.2	Type-I Mixtures	44
4.2.3	Type-II Mixtures	48
4.2.4	Type-III Mixtures	52
4.2.5	Symmetric Mixtures	55
5	Wetting by Symmetric Mixtures	61
5.1	Preamble and Model Aspects	66
5.1.1	Order Parameters and System Size	66
5.1.2	Scaling Considerations	67
5.2	Pure Fluids	70
5.2.1	Layering Transitions and Excess Coverage	70
5.2.2	Wetting Temperature	73
5.3	Wetting Behavior of Symmetric Mixtures	74
5.3.1	Type-I Mixtures	74
5.3.2	Type-II Mixtures	78
5.3.3	Type-III Mixtures	80
6	Confined Symmetric Mixtures	83
6.1	Phase Behavior of Confined Mixtures	84
6.1.1	Type-I Mixtures	85
6.1.2	Type-II Mixtures	88
6.1.3	Type-III Mixtures	89

6.2	Impact of Confinement	91
6.2.1	Critical Points and Critical End Points	91
6.2.2	State and Decomposition	93
6.2.3	Film Phases	94
III Comparison with Experimental Data		97
7	Confinement Effect on the Adsorption from C₄E₁+H₂O Mixtures	101
7.1	Determination of Model Parameters	102
7.1.1	Interaction Parameters	102
7.1.2	Confinement Parameters	103
7.1.3	Thermodynamic States	104
7.2	Adsorption and Pore Width	105
7.3	Concentration Profiles	106
7.4	Summary of Confined C ₄ E ₁ +H ₂ O Mixtures	108
8	Interpretation of SANS-Data of Confined iBA+D₂O Mixtures	109
8.1	Experimental Details	110
8.2	Determination of Model Parameters	111
8.2.1	Interaction Parameters	111
8.2.2	Confinement Parameters	112
8.2.3	Thermodynamic States	112
8.2.4	Phase Diagram of Bulk Systems	113
8.3	Phase Diagram of Confined Systems	114
8.4	Structure and Contrast Factors	115
8.4.1	D ₂ O-rich Phases	116
8.4.2	iBA-rich Phases	117
8.5	Summary of Confined iBA+D ₂ O Mixtures	119
9	Conclusion	121
	Bibliography	129
	Publications	142

CHAPTER 1

Introduction

Gases and liquids to which we henceforth refer as *fluids* are distinguished from solids in that they always assume the shape of their container. Consequently, fluid properties are not only determined by the interactions between individual molecules but also by the interaction with the container wall. Whereas this latter effect is negligible if the container dimensions are large compared to typical intermolecular forces this is no longer so if the container size becomes comparable to the range of these forces as is the case, for example, if fluids are confined to a nanoporous solid matrix. In this case the interplay and competition between fluid–fluid and fluid–substrate forces has profound consequences even for pure (i.e., one-component) fluids. A well known example is the confinement-induced shift of the gas+liquid critical point caused by the finite (nanoscopic) dimension of the containing matrix [1]. Although confinement to nanoscopic dimensions causes a richer and sometimes peculiar phase behavior of pure fluids compared with the bulk, an even more complex behavior is to be expected for binary (A+B) fluid mixtures. Here we are not only confronted with intermolecular interactions that may differ between A–A, A–B, and B–B pairs of molecules, but also with the selectivity of the container walls, that is an energetic preference of these walls for one molecular species over the other. This thesis is devoted to a comprehensive

study of the phase behavior of binary fluid mixtures interacting with solid surfaces.

Bulk Systems. However, already in cases of (almost) infinite bulk systems and far away from any container wall binary mixtures exhibit a fascinatingly rich phase behavior. This was demonstrated in the pioneering work of van Konynenburg and Scott [2] who introduced a classification scheme for phase-diagram topologies of binary mixtures based upon the (empirically motivated) Van der Waals equation of mixtures [3]. Their work was later extended by Furman and Griffiths [4], Deiters *et al.* [5, 6], and Meijer *et al.* [7, 8]. However, even to date it is not well understood precisely which microscopic features determine a given topology.

The phase diagram of binary mixtures is spanned by three thermodynamic fields or variables, namely the temperature T , the mean chemical potential¹ μ coupling to the total density, and an ordering field $\Delta\mu$ coupling to the relative concentrations of the two fluid components. For a binary mixture, the gas+liquid and the liquid+liquid transitions, triggered by μ and $\Delta\mu$, respectively, were usually studied *separately*. However, it is a valid and interesting question how these transitions influence each other.

In the bulk Wilding and co-workers [9–13] and Kahl *et al.* [14] disclosed the phase behavior of *symmetric* binary mixtures for which the ordering field $\Delta\mu$ vanishes. These authors (e.g. [12]) found three general types (I–III) of symmetric bulk mixtures depending on the interaction strength between unlike molecules. Studies of *asymmetric* bulk mixtures, on the other hand, are scarce [15] and remained incomplete. In this thesis we therefore extend the approach of Wilding *et al.* to the more general case of $\Delta\mu \neq 0$. Even though the three types of binary mixtures are still recovered they exhibit a much richer phase behavior which has not yet been reported in the literature.

Wetting Phenomena. The phase behavior becomes even more complex if the fluid mixture interacts with a solid surface. Such a solid substrate has an important influence on fluid molecules in its vicinity as it exerts on them attractive or repulsive forces (i.e., surface fields). As a consequence novel surface-induced phases and phase transitions usually referred to as *wetting* phenomena arise. That wetting phenomena should be perceived as surface-induced phase transitions was first suggested by Cahn [16].

A fundamental understanding of wetting characteristics is important in a variety of contexts. For example, the wettability of tablets and capsules is an issue in pharmaceutical applications [17]. Wetting also affects the effectiveness of cleaning processes [18], the preservation by impregnation or paint coating [19], the wettability of contact lenses in optics, and that of fibers and fabrics in textiles [20]. Binary mixtures in contact with a solid substrate are of particular importance because their properties are sensible to their composition. Thus, by adding appropriate components to the fluid mixture one can readily modify its wetting behavior.

The study of wetting phenomena of *pure* fluids has a long history going back to the works of Young [21] and Dupré [22] who derived an empirical equation relating the contact angle to various interfacial tensions. More recently, Dash [23] investigated

¹Instead of μ , the pressure P is also frequently used.

complete wetting characterized by a vanishing contact angle in the vicinity of the bulk critical point, whereas Ebner and Saam [24–26] discovered the so-called prewetting transition between microscopically thin and thick films. At the same time, Dash [23] and Sullivan [27] introduced a scheme of wetting classes depending on the fluid–fluid and fluid–substrate interaction strengths. This study was extended and amended by Pandit *et al.* [28], Ball and Evans [29], and Binder and Landau [30], who also elucidated the scope of so-called layering and prewetting transitions. Moreover, Dietrich *et al.* [31, 32], and Fisher and de Gennes [33] investigated the order of wetting transitions as well as critical wetting.

While most of these works involve *pure* fluids, some attention was also paid to wetting by binary mixtures. Experimentally, binary mixtures close to the liquid+liquid coexistence were analyzed by Beysens and Estéve [34, 35], Bennes *et al.* [36], Sellami *et al.* [37], Plech *et al.* [38–40], and Bowers *et al.* [41, 42]. All these authors found prewetting transitions in liquid binary mixtures for selective substrates. These findings were supported by Monte-Carlo simulations of Monson *et al.* [43, 44]. Moreover, spinodal surface-induced decomposition of adsorbed films was studied by Binder *et al.* [45–47].

However, similar to bulk mixtures, wetting scenarios in regions, where all three phases, namely gas and the two demixed liquids, are thermodynamically stable, attracted only little theoretical attention so far. Exceptions are the works by Evans *et al.* [48, 49] who extended the classification scheme of Dash and Sullivan to binary mixtures obeying the Berthelot mixing rule. Later, Schmid and Wilding [50] examined gas adsorption from symmetric binary mixtures by a nonselective wall. More recently, Silbermann *et al.* [51] investigated wetting behavior of slightly asymmetric mixtures as a function of the selectivity of the substrate. On account of the high dimension of the parameter space, the three studies are restricted to a rather narrow range of system parameters.

In contrast, the present study focuses on the interplay between the type of the *symmetric* bulk mixture and the strength of the *nonselective* substrate attraction thereby extending the earlier studies by Schmid and Wilding in a systematic way.

Confined Mixtures. If the fluid interacts with two solid surfaces instead of one the distance between them adds a new relevant length scale if it is of the order of intermolecular (fluid–fluid) forces as is the case, for instance, in nanoporous solid matrices. That is, when the pore size is comparable to the range of the surface-induced effects such as film adsorption, we expect large shifts in phase coexistence curves and a lowering of critical points [52]. Another interesting feature of fluids confined to very narrow pores concerns the variation of the *dimensionality* of the system. For example, slit pores encountered, for instance, in clay soils [53], in the surface force apparatus [54], or in activated carbon fibers [55] may be perceived as nearly two-dimensional systems, whereas small cylindrical pores (e.g. carbon tubes [56]) lead to nearly one-dimensional systems.

A fundamental analysis of phase phenomena in confined fluid mixtures is both

urgent and timely in view of many applications. For example, mesoporous materials are widely used in the chemical, oil and gas, automobile, food and pharmaceutical industries for mixture separation [57], pollution control and as catalysts for chemical reactions [58, 59]. Confinement effects are also important in geology and geophysics because many rock and soil formations are porous and imbibe ground water, oil, gas or pollutants [60]. Therefore, a better understanding of the impact and implications of confinement on the equilibrium phase behavior, on adsorption rates, and on the nature of mixtures could lead to significant and continual improvements in these industrial processes.

Even though confined *pure* fluids are by now fairly well understood (see the review of Gelb *et al.* [52]), a parallel *comprehensive* theoretical study of confined binary mixtures remains challenging on account of the large parameter space governing their properties. However, the effect of confinement on the properties of mixtures near liquid-liquid coexistence was extensively studied both experimentally [61–64] and theoretically [65–68]. In addition, Liu *et al.* [69, 70], Gelb and Gubbins [71], and Binder *et al.* [45, 46] studied the structure and the decomposition of liquid phases supporting the experimental results of Lin *et al.* [72]. Later Kierlik *et al.* [73, 74] and Klapp *et al.* [75] analyzed the role of hysteresis and metastability within porous materials. Most recently, Schöll-Paschinger *et al.* [76, 77] and Sokołowski *et al.* [78, 79] determined the full phase diagram of *symmetric* mixtures confined to *nonselective* porous matrices for a selected range of model parameters. These authors investigated symmetric mixtures as a function of porosity and fluid–substrate attraction strength. Our study comprises a more generic analysis of this subject in that the present thesis extends this earlier work to *asymmetric* mixtures confined to *selectively* adsorbing solid matrices which eventually permits a direct comparison with experimental data [62, 63].

Outline. The thesis is divided into three parts. Part I introduces a lattice-fluid model that we shall employ throughout this study (Chapter 2). Based upon a mean-field approximation for the intrinsic free energy we obtain a closed expression for the grand potential energy which is subsequently minimized numerically in order to obtain the thermodynamically stable phases. In Chapter 2, we also discuss the fundamental thermodynamic concepts including phase equilibria and transitions in the context of binary fluid mixtures. Part I closes with a description of the numerical treatment employed to compute phase diagrams for a given set of model parameters (Chapter 3).

Part II is divided into three chapters where we present the results of our theoretical studies. Chapter 4 comprises a discussion of asymmetric bulk mixtures and focuses on the order of demixing transitions. Wetting phenomena of symmetric binary mixtures in contact with a single nonselective solid substrate are investigated in Chapter 5. Part II concludes with a detailed analysis of the effect of confinement on both the phase-diagram topology and local structure of symmetric binary mixtures (Chapter 6).

In Part III we compare our model calculations with results of two experimental studies (Chapters 7 and 8) which were performed in the group of Findenegg. We show that, on the one hand, our model is capable of describing the phase behavior of confined

asymmetric mixtures at least at a qualitative level. On the other hand, the microscopic picture obtained from theoretical analysis carried out here assists the interpretation of the experimental findings.

A summary of the major results can be found in the concluding Chapter 9 where we also discuss future prospects and perspectives.

Part I
Theory

CHAPTER 2

Model

2.1 Lattice Fluid

We consider a classical binary mixture of $N = N_A + N_B$ equally-sized particles of species A and B contained in a volume V . The particles are assumed spherically symmetric such that intermolecular interactions depend only on the distance r between the centers of mass of a pair of molecules. However, the interaction strength may depend on whether the interacting molecules are an A–A, B–B, or A–B pair. In general, the interaction potential will be repulsive at short but attractive at larger distances regardless of the chemical nature of the interacting pair; in the limit $r \rightarrow \infty$ the interaction potential vanishes.

2.1.1 Occupation Matrix

To proceed we discretize the volume V by a regular lattice of \mathcal{N} cubic cells. If we assume that

- (1) there is not more than one molecule per cell,

- (2) the interaction energy between a pair of molecules depends only on the relative position of their respective cells but is independent of the location of each particle within its cell,

we can simplify the treatment, because now the internal energy of the system depends on the position of the cells regardless of the positions of molecules inside the cells. Condition (1) accounts for an infinitely hard core repulsion. If a lattice site is asso-

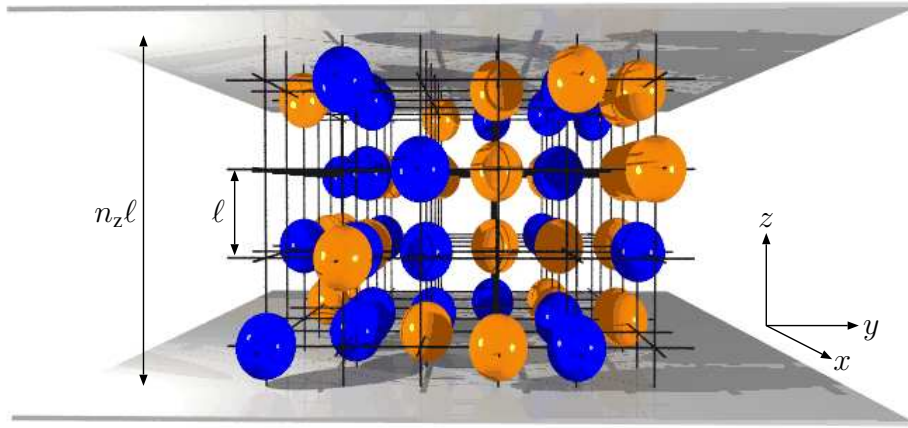


Figure 2.1: Sketch of a lattice fluid with lattice constant ℓ . Nodes of the mesh of solid lines refer to the lattice sites.

ciated with each cell (see Fig. 2.1) the model is referred to as lattice gas or more appropriately *lattice fluid* [80].

Consider now a binary A+B mixture on a simple cubic lattice with $\mathcal{N} = n n_z$ sites, whose lattice constant is ℓ as shown in Fig. 2.1. Then, a lattice site is specified by a pair of integers (k, z) where $1 \leq k \leq n$ labels the position in the x - y plane and $1 \leq z \leq n_z$ determines the position along the z -axis. In order to describe individual configurations in the volume $V = \mathcal{N}\ell^3$, we introduce the $(n \times n_z)$ occupation matrix $\mathbb{S} \equiv \{s_{k,z}\}$ such that

$$s_{k,z} = \begin{cases} +1 & \text{cell occupied by an A molecule} \\ 0 & \text{empty cell} \\ -1 & \text{cell occupied by an B molecule.} \end{cases} \quad (2.1)$$

Thus, a configuration of particles can be described by a specific occupation matrix \mathbb{S} . For a given \mathbb{S} we can easily calculate the total number of cells occupied by molecules

of species A or B as

$$\begin{aligned} N_A(\mathbb{S}) &= \frac{1}{2} \sum_{k=1}^n \sum_{z=1}^{n_z} s_{k,z} (s_{k,z} + 1) \\ N_B(\mathbb{S}) &= \frac{1}{2} \sum_{k=1}^n \sum_{z=1}^{n_z} s_{k,z} (s_{k,z} - 1). \end{aligned} \quad (2.2)$$

2.1.2 Hamiltonian

Since the overall number of possible configurations \mathbb{S} is now finite¹ and configuration space is discretized, we may introduce the partition function of the grand canonical ensemble via [80]

$$\Xi(T, \mathcal{N}, \mu_A, \mu_B) = \sum_{\mathbb{S}} e^{-\beta \mathcal{H}(\mathbb{S})} = \left(\prod_{z=1}^{n_z} \prod_{k=1}^n \sum_{s_{k,z}=-1}^1 \right) e^{-\beta \mathcal{H}(\mathbb{S})} \equiv e^{-\beta \Omega} \quad (2.3)$$

where \mathcal{H} is the Hamiltonian. Here the volume is replaced by the numbers of lattice cells (i.e., $V = \mathcal{N} \ell^3$) and $\beta = 1/k_B T$. Also, the last term in Eq. (2.3) defines the grand potential $\Omega(T, \mathcal{N}, \mu_A, \mu_B)$.

The Hamiltonian depends on the configuration and is therefore a function of the occupation matrix \mathbb{S} . Internal and external contributions to \mathcal{H} are introduced in the following paragraph.

Internal Part. The internal configurational energy is a sum of interaction energies of all molecular pairs. We model such interactions according to square-well potentials where the width of the attractive well is equal to the lattice constant ℓ . Hence we restrict ourselves exclusively to *nearest-neighbor attractions*. Now, for a given occupation configuration \mathbb{S} we can work out expressions for the number N_{AA} (N_{BB}) of A–A (B–B) pairs of interacting (i.e., neighboring) molecules

$$\begin{aligned} N_{AA}(\mathbb{S}) &= \frac{1}{8} \sum_{k=1}^n \sum_{z=1}^{n_z} s_{k,z} (s_{k,z} + 1) \left[s_{k,z+1} (s_{k,z+1} + 1) + s_{k,z-1} (s_{k,z-1} + 1) + \right. \\ &\quad \left. \sum_{m=1}^{\text{NN}(k)} s_{m,z} (s_{m,z} + 1) \right] \\ N_{BB}(\mathbb{S}) &= \frac{1}{8} \sum_{k=1}^n \sum_{z=1}^{n_z} s_{k,z} (s_{k,z} - 1) \left[s_{k,z+1} (s_{k,z+1} - 1) + s_{k,z-1} (s_{k,z-1} - 1) + \right. \\ &\quad \left. \sum_{m=1}^{\text{NN}(k)} s_{m,z} (s_{m,z} - 1) \right] \end{aligned} \quad (2.4)$$

¹However, the number of configurations is still $3^{\mathcal{N}}$ which can be quite large.

where the summation over m extends over the four nearest neighbors $\text{NN}(k)$ of site k in the x - y plane. A slightly more complicated expression obtains for the number of interacting A–B neighbors

$$N_{\text{AB}}(\mathbb{S}) = \frac{1}{8} \sum_{k=1}^n \sum_{z=1}^{n_z} s_{k,z} (s_{k,z} + 1) \left[s_{k,z+1} (s_{k,z+1} - 1) + s_{k,z-1} (s_{k,z-1} - 1) + \sum_{m=1}^{\text{NN}(k)} s_{m,z} (s_{m,z} - 1) \right] + s_{k,z} (s_{k,z} - 1) \left[s_{k,z+1} (s_{k,z+1} + 1) + s_{k,z-1} (s_{k,z-1} + 1) + \sum_{m=1}^{\text{NN}(k)} s_{m,z} (s_{m,z} + 1) \right]. \quad (2.5)$$

Because of the repulsion *felt* by particles at the boundaries, we amend Eqs. (2.4) and (2.5) by the conditions

$$\begin{aligned} s_{k,0} = s_{k,n_z+1} = 0 \quad \forall k \\ s_{0,z} = s_{n+1,z} = 0 \quad \forall z. \end{aligned} \quad (2.6)$$

Using these expressions, we can cast the Hamiltonian as

$$\mathcal{H}(\mathbb{S}) = \epsilon_{\text{AA}} N_{\text{AA}}(\mathbb{S}) + \epsilon_{\text{BB}} N_{\text{BB}}(\mathbb{S}) + \epsilon_{\text{AB}} N_{\text{AB}} + \Phi(\mathbb{S}), \quad (2.7)$$

where the last term on the right side refers to the external part $\Phi(\mathbb{S})$, which is discussed in the next paragraph. In Eq. (2.7), ϵ_{AA} , ϵ_{BB} , and ϵ_{AB} (all ≤ 0) represent the depths of the attractive wells of square-well potentials of interacting A–A, B–B, and A–B pairs, respectively.

External Part. Suppose now, the fluid mixture is confined between two planar homogenous solid substrates parallel to the x - y plane placed at $z = 0$ and $z = n_z + 1$. Then, the interaction between a molecule and the substrates depends only on the z -coordinate of that molecule. Together with the chemical potentials μ_{A} and μ_{B} of species A and B, respectively, the external part of the Hamiltonian in the grand canonical ensemble may be written as

$$\begin{aligned} \Phi(\mathbb{S}) = -\mu_{\text{A}} N_{\text{A}}(\mathbb{S}) - \mu_{\text{B}} N_{\text{B}}(\mathbb{S}) + \\ \frac{1}{2} \sum_{z=1}^{n_z} \sum_{k=1}^n V_{\text{A}}(z) s_{k,z} (s_{k,z} + 1) + V_{\text{B}}(z) s_{k,z} (s_{k,z} - 1) \end{aligned} \quad (2.8)$$

where $V_{\text{A}}(z)$ ($V_{\text{B}}(z)$) determines the attractive potential between the substrates and molecules of species A (B). Note, that the repulsion of the walls is already accounted for by the first set of boundary conditions in Eq. (2.6).

2.2 Mean-Field Approximation

Unfortunately, an analytic calculation of the partition function Ξ (and therefore of the grand potential Ω) is still prevented because in principle the summation over \mathbb{S} involves an astronomically large number of terms (i.e., $\propto 3^N$). One may, however, bypass this problem by replacing the analytic treatment of Eq. (2.3) by a numerical approach such as a Monte-Carlo method [12, 44, 81–84]. However, Monte-Carlo simulations are rather time consuming and a comprehensive picture of fluid phase behavior, especially for confined binary mixtures, becomes prohibitive. For this reason we resort to a mean-field approximation with which a (numerical) treatment of Eq. (2.3) becomes feasible.

2.2.1 Hamiltonian and Partition Function

To proceed we introduce a mean-field approximation for the Hamiltonian given in Eq. (2.7). Assuming a sufficiently large system in the x - and y -direction (i.e., $n \gg n_z$) we replace the occupation numbers across each plane z parallel to the substrates by the average (mean) occupation density associated with that plane. Because of the z -dependence of the substrate potentials this average density changes with z . Hence, we introduce the mean local densities of A and B molecules in plane z via

$$\begin{aligned}\rho_z^A &= \frac{1}{2n} \sum_{k=1}^n s_{k,z} (s_{k,z} + 1) \equiv \frac{n_z^A}{n} \\ \rho_z^B &= \frac{1}{2n} \sum_{k=1}^n s_{k,z} (s_{k,z} - 1) \equiv \frac{n_z^B}{n}\end{aligned}\tag{2.9}$$

as convenient alternative order parameters at mean-field level. In the limit $n \rightarrow \infty$, ρ_z^A and ρ_z^B (in units of ℓ^3) are continuous on the interval $[0, 1]$ but are constrained by the condition $\rho_z^A + \rho_z^B \leq 1$.

From a strictly mathematical view point the mean-field approximation consists of mapping the $(n \times n_z)$ occupation matrix \mathbb{S} onto the two z -dimensional vectors $\boldsymbol{\rho}^A = (\rho_1^A, \dots, \rho_{n_z}^A)$ and $\boldsymbol{\rho}^B = (\rho_1^B, \dots, \rho_{n_z}^B)$. That is, the specific arrangement of molecules of species A or B in the x - y planes is neglected or averaged out. Thus, the transformation $\mathbb{S} \rightarrow (\boldsymbol{\rho}^A, \boldsymbol{\rho}^B)$ is bijective if and only if all mean densities (i.e., ρ^A and ρ^B) are either zero or unity, that is *all* sites in the same plane are either empty or filled by one or the other species which is the case in the limit $T = 0$ (see also Sec. 3.1.1).

To derive the mean-field analog of Eq. (2.7) we replace the sums over k in Eqs.

(2.2), (2.4) and (2.5) according to Eq.(2.9) and obtain

$$\begin{aligned} \mathcal{H}_{\text{mf}}(\boldsymbol{\rho}^{\text{A}}, \boldsymbol{\rho}^{\text{B}}) = n \sum_{z=1}^{n_z} \left\{ \frac{\epsilon_{\text{AA}}}{2} \rho_z^{\text{A}} (\rho_{z+1}^{\text{A}} + \rho_{z-1}^{\text{A}} + 4\rho_z^{\text{A}}) + \frac{\epsilon_{\text{BB}}}{2} \rho_z^{\text{B}} (\rho_{z+1}^{\text{B}} + \rho_{z-1}^{\text{B}} + 4\rho_z^{\text{B}}) \right. \\ \left. + \frac{\epsilon_{\text{AB}}}{2} (\rho_z^{\text{A}} (\rho_{z+1}^{\text{B}} + \rho_{z-1}^{\text{B}} + 4\rho_z^{\text{B}}) + \rho_z^{\text{B}} (\rho_{z+1}^{\text{A}} + \rho_{z-1}^{\text{A}} + 4\rho_z^{\text{A}})) \right. \\ \left. + V_{\text{A}}(z)\rho_z^{\text{A}} + V_{\text{B}}(z)\rho_z^{\text{B}} - \mu_{\text{A}}\rho_z^{\text{A}} - \mu_{\text{B}}\rho_z^{\text{B}} \right\}. \end{aligned} \quad (2.10)$$

As mentioned above, the transformation $\mathbb{S} \rightarrow (\boldsymbol{\rho}^{\text{A}}, \boldsymbol{\rho}^{\text{B}})$ is not bijective in general since one set of $(\boldsymbol{\rho}^{\text{A}}, \boldsymbol{\rho}^{\text{B}})$ may represent different configurations. The combinatorial factor

$$\begin{aligned} \Theta(\boldsymbol{\rho}^{\text{A}}, \boldsymbol{\rho}^{\text{B}}) &= \prod_{z=1}^{n_z} \binom{n}{n_z^{\text{A}} + n_z^{\text{B}}} \binom{n_z^{\text{A}} + n_z^{\text{B}}}{n_z^{\text{A}}} \\ &= \prod_{z=1}^{n_z} \binom{n}{n(\rho_z^{\text{A}} + \rho_z^{\text{B}})} \binom{n(\rho_z^{\text{A}} + \rho_z^{\text{B}})}{n\rho_z^{\text{A}}} \end{aligned} \quad (2.11)$$

accounts for this degeneracy of a particular microstate at mean-field level. If Θ assumes one then the mean-field treatment is exact. Equations (2.10) and (2.11) permit us to write down the mean-field analog of Eq. (2.3), namely

$$\Xi_{\text{mf}}(T, \mathcal{N}, \mu_{\text{A}}, \mu_{\text{B}}) = \left(\prod_{z=1}^{n_z} \sum_{\rho_z^{\text{A}}=0}^1 \sum_{\rho_z^{\text{B}}=0}^{1-\rho_z^{\text{A}}} \right) \Theta(\boldsymbol{\rho}^{\text{A}}, \boldsymbol{\rho}^{\text{B}}) e^{-\beta \mathcal{H}_{\text{mf}}(\boldsymbol{\rho}^{\text{A}}, \boldsymbol{\rho}^{\text{B}})}, \quad (2.12)$$

where the summation over the densities, ρ_z^{A} and ρ_z^{B} , is performed in steps of $\Delta\rho = 1/n$.

2.2.2 Thermodynamic Limit

Taking our system now to the thermodynamic limit, that is $n \rightarrow \infty$ and thus $\mathcal{N} \rightarrow \infty$ whereas n_z remains finite, the summation increment $\Delta\rho = \frac{1}{n}$ in Eq. (2.12) becomes infinitesimal. Hence ρ_z^{A} and ρ_z^{B} become continuous on the interval $[0, 1]$. This allows us to replace the two sums by double integrals via

$$\sum_{\rho_z^{\text{A}}=0}^1 \sum_{\rho_z^{\text{B}}=0}^{1-\rho_z^{\text{A}}} \rightarrow n^2 \int_0^1 d\rho_z^{\text{A}} \int_0^{1-\rho_z^{\text{A}}} d\rho_z^{\text{B}}. \quad (2.13)$$

Because of the somewhat cumbersome limits of integration (i.e., the constraint $\rho_z^{\text{A}} + \rho_z^{\text{B}} \leq 1$) it is convenient to change variables by introducing the total local density

$$\rho_z \equiv \rho_z^{\text{A}} + \rho_z^{\text{B}} \quad \forall z \quad (2.14)$$

and the local *miscibility* m_z ,

$$m_z \rho_z \equiv \rho_z^A - \rho_z^B \quad \forall z \quad (2.15)$$

as alternative order parameters. Note that the transformation $(\rho^A, \rho^B) \rightarrow (\rho, \mathbf{m})$ is bijective where $\rho = (\rho_1, \dots, \rho_{n_z})$ and $\mathbf{m} = (m_1, \dots, m_{n_z})$ and we can express

$$\begin{aligned} \rho_z^A &= \frac{1}{2} \rho_z (1 + m_z) \\ \rho_z^B &= \frac{1}{2} \rho_z (1 - m_z) \end{aligned} \quad \forall z \quad (2.16)$$

in terms of the new order parameters ρ_z and m_z which are continuous where $0 \leq \rho_z \leq 1$ in units of ℓ^3 and $-1 \leq m_z \leq 1$. Note, that $m_z < 0$ implies a B-rich fluid whereas $m_z > 0$ characterizes an A-rich fluid. Moreover, the chemical potentials μ_A and μ_B are replaced by the total chemical potential $\bar{\mu}$ and the incremental chemical potential $\Delta\mu$ according to

$$\begin{aligned} \bar{\mu} &\equiv \frac{1}{2} (\mu_A + \mu_B) \\ \Delta\mu &\equiv \frac{1}{2} (\mu_A - \mu_B). \end{aligned} \quad (2.17)$$

Partition Function. Using Eq. (2.13) and the Jacobian for the transformation given in Eqs. (2.14) and (2.15) we finally cast Eq. (2.12) as

$$\begin{aligned} \Xi_{\text{mf}}(T, \mathcal{N}, \bar{\mu}, \Delta\mu) &= \int \rho \, d\rho \int \mathbf{m} \frac{n^{2n_z}}{2^{n_z}} \underbrace{\Theta(\rho, \mathbf{m}) e^{-\beta \mathcal{H}_{\text{mf}}(\rho, \mathbf{m}, \bar{\mu}, \Delta\mu)}}_{\left(e^{-\beta \omega(T, \mathcal{N}, \bar{\mu}, \Delta\mu; \rho, \mathbf{m})} \right)^{\mathcal{N}}} \\ &\equiv \int \rho \, d\rho \int \mathbf{m} \frac{n^{2n_z}}{2^{n_z}} \left(e^{-\beta \omega(T, \mathcal{N}, \bar{\mu}, \Delta\mu; \rho, \mathbf{m})} \right)^{\mathcal{N}}. \end{aligned} \quad (2.18)$$

The last term of Eq. (2.18) *defines* the energy density ω as

$$\omega(T, \mathcal{N}, \bar{\mu}, \Delta\mu; \rho, \mathbf{m}) \equiv -\frac{\ln \Theta(\rho, \mathbf{m})}{\beta \mathcal{N}} + \frac{\mathcal{H}_{\text{mf}}(\rho, \mathbf{m})}{\mathcal{N}} \quad (2.19)$$

which represents an energy hyperplane in the $2n_z$ -dimensional order-parameter space $\{\rho, \mathbf{m}\}$. We note in passing that ω is an energy per unit cell (not per unit volume).

Free Energy Density. In the limit $n \rightarrow \infty$ the binominal coefficients in Eq. (2.11) may be approximated by Stirling's formula [85] yielding

$$\Theta(\rho, \mathbf{m}) \stackrel{n \rightarrow \infty}{\equiv} \prod_{z=1}^{n_z} \frac{n^n}{(n(1-\rho_z))^{n(1-\rho_z)} \left(n\rho_z \frac{1+m_z}{2}\right)^{n\rho_z \frac{1+m_z}{2}} \left(n\rho_z \frac{1-m_z}{2}\right)^{n\rho_z \frac{1-m_z}{2}}}. \quad (2.20)$$

From that expression one can show that $\ln \Theta \propto n$ for large n . Since \mathcal{H}_{mf} in Eq. (2.10) is also proportional to n , Eq. (2.19) reveals that ω is independent of n for fixed n_z because $\mathcal{N} = n n_z$. Thus, in the limit $n \rightarrow \infty$, ω remains finite and depends only on n_z .

In general, the function $\omega(T, n_z, \bar{\mu}, \Delta\mu; \boldsymbol{\rho}, \mathbf{m})$ may have many extrema in $\boldsymbol{\rho}$ - \mathbf{m} space for given $T, n_z, \bar{\mu}$ and $\Delta\mu$. However, if $n \rightarrow \infty$ the integral in Eq. (2.18) is determined only by the global maximum of $e^{-\beta\omega}$, that is the global minimum of ω . Assuming now that ω has such a global minimum at $(\boldsymbol{\rho}^*, \mathbf{m}^*)$, we obtain

$$\Xi_{\text{mf}} \stackrel{n \rightarrow \infty}{=} e^{-\beta\omega(\boldsymbol{\rho}^*, \mathbf{m}^*)} \mathcal{N} \quad (2.21)$$

which allows us to cast ω as the grand potential energy density,

$$\omega(T, n_z, \bar{\mu}, \Delta\mu; \boldsymbol{\rho}^*, \mathbf{m}^*) = \frac{\Omega_{\text{mf}}}{\mathcal{N}} = -\frac{1}{\beta \mathcal{N}} \ln \Xi_{\text{mf}} \quad (2.22)$$

Equilibrium Phase. From the above expressions the final expression of the grand potential energy density follows as

$$\begin{aligned} \omega(T, n_z, \mu, \Delta\mu; \boldsymbol{\rho}, \mathbf{m}) = & \\ & \frac{1}{n_z} \sum_{z=1}^{n_z} \left\{ k_{\text{B}} T \left[\rho_z \ln \rho_z + (1 - \rho_z) \ln(1 - \rho_z) + \right. \right. \\ & \quad \left. \left. \frac{\rho_z}{2} \left((1 + m_z) \ln(1 + m_z) + (1 - m_z) \ln(1 - m_z) \right) \right] + \right. \\ & \quad \frac{\epsilon_{\text{AA}}}{8} \left[\rho_{z+1}(1 + m_{z+1}) + \rho_{z-1}(1 + m_{z-1}) + 4\rho_z(1 + m_z) \right] \rho_z(1 + m_z) + \\ & \quad \frac{\epsilon_{\text{BB}}}{8} \left[\rho_{z+1}(1 - m_{z+1}) + \rho_{z-1}(1 - m_{z-1}) + 4\rho_z(1 - m_z) \right] \rho_z(1 - m_z) + \\ & \quad \frac{\epsilon_{\text{AB}}}{4} \left[\rho_{z+1}(1 - m_z m_{z+1}) + \rho_{z-1}(1 - m_z m_{z-1}) + 4\rho_z(1 - m_z^2) \right] \rho_z + \\ & \quad \left. \frac{V_{\text{A}}(z)}{2} \rho_z(1 + m_z) + \frac{V_{\text{B}}(z)}{2} \rho_z(1 - m_z) - \mu \rho_z - \Delta\mu \rho_z m_z \right\} \end{aligned} \quad (2.23)$$

where $\mu \equiv \bar{\mu} + T \ln 2$ is the auxiliary chemical potential, which is introduced to eliminate the trivial entropy contribution due to different *colors* (i.e., labels *A* and *B*) of molecules (see also Sec. 2.3). Also, for confined mixtures we need to modify the boundary conditions in Eq. (2.6) according to

$$\begin{aligned} \rho_0 = \rho_{n_z+1} &= 0 \\ m_0 = m_{n_z+1} &= 0. \end{aligned} \quad (2.24)$$

In order to obtain the thermodynamically *stable* phase, ω has to be minimized *globally* with respect to $\boldsymbol{\rho}$ and \mathbf{m} . All other local minima are referred to as *metastable*. Note, that the term *phase* \mathcal{P} is used for a certain set of order parameters $(\boldsymbol{\rho}, \mathbf{m})$ where ω is locally minimal.

So far we did not introduce the attractive potential between the mixture and the two confining substrates. Because we employ two different types of interactions we defer this to the next section.

2.2.3 Fluid-Substrate Potential

Short-Range Interaction. A simple way to model substrate attraction is to employ short-range square-well potentials for the interaction between walls and molecules of species A (B) where the width of the attractive well is ℓ and ϵ_{WA} (ϵ_{WB}) is its depth. Thus, we have

$$\begin{aligned} V_{\text{A}}(z) &= -\epsilon_{\text{WA}}(\delta_{1z} + \delta_{n_z z}) \\ V_{\text{B}}(z) &= -\epsilon_{\text{WB}}(\delta_{1z} + \delta_{n_z z}) \end{aligned} \quad (2.25)$$

with Kronecker's symbol δ . Figure 2.2 shows this schematically.

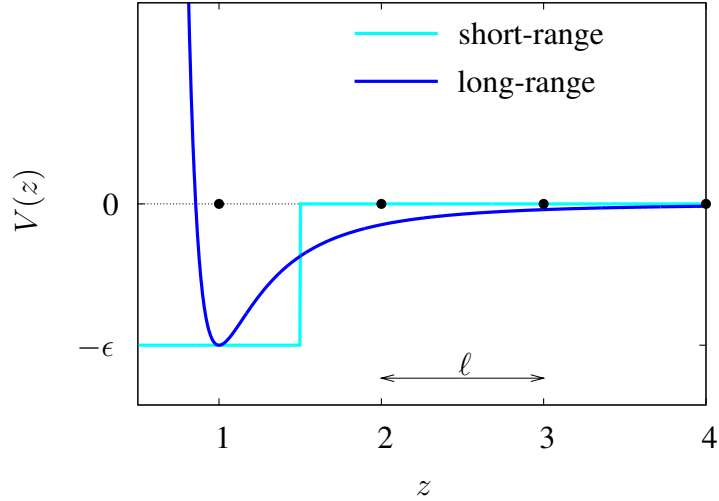


Figure 2.2: Short- and long-range interactions between molecules and one substrate as a function of the distance z . Dots indicate the positions of lattice cells which a particle may occupy.

Long-Range Interaction. Long-range fluid–substrate interactions are somewhat more realistic with respect to experimental systems. To take this into account we consider a solid substrate as a semi-finite homogenous plane. We integrate the usual Lennard-Jones potential over this substrate and obtain the so called 3-9 potential [86]

$$V(z) = \epsilon \left(\frac{2}{15} \frac{1}{z^9} - \frac{1}{z^3} \right) \quad z = 1, \dots, n_z. \quad (2.26)$$

However, in a confined system (i.e., slit pore) both substrates may interact with a single molecule. Thus, we can express the long-range wall potentials by

$$\begin{aligned} V_A(z) &= \epsilon_{WA} \left(\frac{2}{15} \frac{1}{z^9} - \frac{1}{z^3} + \frac{2}{15} \frac{1}{(n_z + 1 - z)^9} - \frac{1}{(n_z + 1 - z)^3} \right) \\ V_B(z) &= \epsilon_{WB} \left(\frac{2}{15} \frac{1}{z^9} - \frac{1}{z^3} + \frac{2}{15} \frac{1}{(n_z + 1 - z)^9} - \frac{1}{(n_z + 1 - z)^3} \right) \end{aligned} \quad z = 1, \dots, n_z. \quad (2.27)$$

2.3 Units

In order to compare our findings with other models or experimental results, it is convenient to introduce dimensionless or reduced parameters. Thus, dividing Eq. (2.23) by $|\epsilon_{AA}|$ we may express temperature, attraction strengths and external fields in dimensionless units indicated by an asterisk “*”, namely

$$\begin{aligned} T^* &\equiv \frac{k_B T}{|\epsilon_{AA}|} & \omega^* &\equiv \frac{\omega}{|\epsilon_{AA}|} \\ \mu^* &\equiv \frac{\mu}{|\epsilon_{AA}|} & \Delta\mu^* &\equiv \frac{\Delta\mu}{|\epsilon_{AA}|} \\ \epsilon_{BB}^* &\equiv \frac{\epsilon_{BB}}{\epsilon_{AA}} \quad (\geq 0) & \epsilon_{AB}^* &\equiv \frac{\epsilon_{AB}}{\epsilon_{AA}} \quad (\geq 0) \\ \epsilon_{WA}^* &\equiv \frac{\epsilon_{WA}}{|\epsilon_{AA}|} \quad (\geq 0) & \epsilon_{WB}^* &\equiv \frac{\epsilon_{WB}}{|\epsilon_{AA}|} \quad (\geq 0). \end{aligned} \quad (2.28)$$

Note, that the dimensionless attraction strengths are positive or zero henceforth. Additionally, the length along the z -direction is given in units of the lattice constant ℓ (i.e., z itself is dimensionless). The energy density ω^* as well as all densities ρ_z are given per unit cell. To convert to volume densities one should multiply by ℓ^3 .

Recalling the definition of the auxiliary chemical potential, $\mu = \bar{\mu} + T \ln 2$, of Sec. 2.2.2, we obtain the state of the *one*-component fluid with its real chemical potential μ by simply setting $\epsilon_{AB}^* = \epsilon_{BB}^* = 1$ and $\Delta\mu = 0$. The entropic contribution due to the (still) different *colors* of the particles is included.

2.4 Phase Coexistence

2.4.1 Thermodynamic Conditions

In the grand canonical ensemble the thermodynamic potential of a fluid confined to a slit pore is given by $\Omega = -P_{\parallel} V$ [87] which leads to

$$\omega(T, n_z, \mu, \Delta\mu) = \frac{\Omega}{\mathcal{N}} = -P_{\parallel}(T, V, \mu, \Delta\mu) \ell^3 = -P_{\parallel}(T, n_z, \mu, \Delta\mu) \ell^3 \quad (2.29)$$

where we use $V = \mathcal{N}\ell^3$. The pressure component parallel to the substrates, P_{\parallel} , is equal to the negative first two diagonal terms of the stress tensor (i.e., $-T_{xx} = -T_{yy}$) and depends only on the pore width n_z . The conditions for phase coexistence between two different² phases, say \mathcal{P}_1 and \mathcal{P}_2 , are written as

$$\begin{aligned} T(\mathcal{P}_1) &= T(\mathcal{P}_2) \\ \mu(\mathcal{P}_1) &= \mu(\mathcal{P}_2) \\ \Delta\mu(\mathcal{P}_1) &= \Delta\mu(\mathcal{P}_2) \\ P_{\parallel}(\mathcal{P}_1) &= P_{\parallel}(\mathcal{P}_2). \end{aligned} \tag{2.30}$$

Hence, all thermodynamically intensive variables of the two coexisting phases have to be equal. One can see that in the grand canonical ensemble the first three equalities in Eq. (2.30) hold as μ , $\Delta\mu$ and T are the natural variables. Since the volume is also fixed, the pressure condition in Eq. (2.30) is equivalent to $\omega(\mathcal{P}_1) = \omega(\mathcal{P}_2)$ (see Eq. (2.29)). Therefore, *coexistence* of two stable phases corresponds to a global double minimum of ω (see subsequent Sec. 2.2.2), that is $\omega(\mathcal{P}_1) = \omega(\mathcal{P}_2)$.

2.4.2 Order of Phase Transitions

Let us now classify the order of phase transitions. In general, Ehrenfest's classification scheme [88, 89] defines as r th-order phase transition one in which there is a finite discontinuity in the $(r - 1)$ th derivative of the relevant order parameter with respect to the corresponding field; all lower derivatives (including the 0th derivative, that is the order parameter itself) remain continuous. Here the term *field* refers to the natural thermodynamic variable conjugated to the order parameter, for example the field μ for the order parameter ρ . Fisher [90] proposed a classification of just two categories, *first-order* and *continuous* (or *higher-order*). We follow this latter classification in the following. In this sense phase coexistence as discussed in Sec. 2.4 refers to a first-order transition because of the different order parameters of the two coexisting phases.

In this work, Eq. (2.23) shows that the order parameters ρ and \mathbf{m} are coupled to the *fields* (i.e., chemical potentials) μ and $\Delta\mu$ respectively. Thus, we have a *first-order* transition when we observe a discontinuity in at least one of the order parameters while changing the corresponding fields. When observing discontinuities in some of the first derivatives with respect to fields (i.e., μ or $\Delta\mu$), we shall use the term *second-order* phase transition. Normally, first-order coexistence ends at a critical point at which both phases become identical but where the first derivative diverges (see also Sec. 2.4). Thus, a critical point denotes a second-order phase transition.

²i.e., in order parameters (ρ , \mathbf{m})

2.4.3 Gibbs' Phase Rule and Dimensionality

In this section we consider the dimensionality of sets of points of coexistence in thermodynamic state space. Based upon Gibbs' phase rule (e.g. in [80]) we may write

$$(\text{dimension}) = (\text{number of components}) + 2 - (\text{coexisting phases}), \quad (2.31)$$

where "dimension" is the geometrical dimension of the set of phase coexistences. For a binary mixture the number of components is two. Therefore, all points of coexistence of two phases define a two-dimensional surface. Moreover, triple points, that is points where three phases coexist, form lines which we shall call triple lines.

Since we have *one* sufficient condition for coexistence of two phases (i.e., $\omega(\mathcal{P}_1) = \omega(\mathcal{P}_2)$), all points of coexistence fall onto a *two*-dimensional surface in the *three*-dimensional variable space $(\mu, \Delta\mu, T)$. This is different in the case of one-component fluids where phase coexistences are lines in T - μ space. Since at critical points (see above) we have one more sufficient condition (i.e., the first derivative with respect to fields must vanish), critical points which may border surfaces of phase coexistence become lines in binary mixtures. Exceptions are tricritical *points* where three phases become critical (i.e., two conditions more) which may be found as isolated points. Finally, we may observe critical end points which are triple points, but with two of the three coexistent phases being critical. Table 2.1 gives an overview of the dimensionality of various sets of coexistences in $(\mu, \Delta\mu, T)$ space.

	Coexistent Phases			Critical Phases		Critical End Point
	2	3	4	2	3	
Geometrical Dimension	2	1	0	1	0	0
Object	coexistence surface	triple line	quadruple point	critical line	tricritical point	cep

Table 2.1: Sets of phase coexistences for binary mixtures.

Moreover, the preceding discussion leads to the introduction of a *phase diagram* as an union of all phase coexistence points. The numerical procedure and the algorithm to obtain phase diagrams for certain sets of model parameters are described in the following chapter.

CHAPTER 3

Numerical Treatment

In this chapter we describe the numerical treatment for calculating phase diagrams of a given set of model parameters and thermodynamic variables. First, we derive conditions for obtaining single stable phases corresponding to global minima of the free energy density ω . From this it is possible to search for points at which two or more phases are at coexistence which is explained in detail in the subsequent section. Finally, we introduce an algorithm to implement such a procedure in a numerically.

3.1 Conditions for Stable Phases

The state of our model system depends on thermodynamic variables T^* , n_z , μ^* , and $\Delta\mu^*$, as well as on interaction parameters ϵ_{BB}^* , ϵ_{AB}^* , ϵ_{WA}^* , ϵ_{WB}^* and on the *type* of the substrate potential. For a given set of such *model parameters*, we are able to calculate the local order parameters (ρ, \mathbf{m}) of thermodynamically stable phases which is described in this section. At thermodynamic equilibrium the grand potential energy per cell, ω , assumes a global minimum with respect to variations of ρ and \mathbf{m} for fixed model parameters (see Sec. 2.2.2).

3.1.1 Vanishing Temperature

In the limit $T \rightarrow 0$, the entropic part of ω (i.e., the first two lines in Eq. (2.23)) vanishes. As discussed in Sec. 2.2 the mean-field approximation becomes exact for $T = 0$ where all entropic contributions in the occupation matrix \mathbb{S} vanish in accordance with the third law of thermodynamics. On account of the x - y symmetry of all external fields this can be the case if and only if all cells in one x - y plane at position z are equally occupied, assuming one of the three values: empty ($\rho_z = 0, m_z = 0$), occupied by A-molecules ($\rho_z = 1, m_z = 1$), or B-molecules ($\rho_z = 1, m_z = -1$). For all three scenarios Eq. (2.20) yields $\Theta = 1$. Thus, the entropic term of ω in Eq. (2.19), which is proportional to $\ln \Theta$, vanishes.

3.1.2 Non-Vanishing Temperature

For $T > 0$, the local densities and miscibilities are no longer discrete as before for $T = 0$ but continuous on *open* intervals $(0, 1)$ and $(-1, 1)$, respectively. From this, the *necessary* conditions for the existence of a global minimum in ω may be stated as

$$\begin{aligned} \frac{\partial \omega}{\partial \rho_z} &= 0 & \forall z \\ \frac{\partial \omega}{\partial m_z} &= 0 & \forall z. \end{aligned} \quad (3.1)$$

From Eq. (2.23) conditions (3.1) can be rewritten as

$$\begin{aligned} \frac{\partial \omega}{\partial \rho_z} = \frac{1}{n_z} \left\{ k_B T \left[\ln \frac{\rho_z}{1 - \rho_z} + \frac{1}{2} \left((1 + m_z) \ln(1 + m_z) + (1 - m_z) \ln(1 - m_z) \right) \right] + \right. \\ \frac{\epsilon_{AA}}{4} \left[\rho_{z+1}(1 + m_{z+1}) + \rho_{z-1}(1 + m_{z-1}) + 4\rho_z(1 + m_z) \right] (1 + m_z) + \\ \frac{\epsilon_{BB}}{4} \left[\rho_{z+1}(1 - m_{z+1}) + \rho_{z-1}(1 - m_{z-1}) + 4\rho_z(1 - m_z) \right] (1 - m_z) + \\ \frac{\epsilon_{AB}}{2} \left[\rho_{z+1}(1 - m_z m_{z+1}) + \rho_{z-1}(1 - m_z m_{z-1}) + 4\rho_z(1 - m_z^2) \right] + \\ \left. \frac{V_A(z)}{2} (1 + m_z) + \frac{V_B(z)}{2} (1 - m_z) - \mu - \Delta\mu m_z \right\} = 0 \end{aligned} \quad (3.2)$$

$$\begin{aligned}
\frac{\partial \omega}{\partial m_z} = \frac{1}{n_z} \left\{ k_B T \frac{\rho_z}{2} \ln \frac{1+m_z}{1-m_z} + \right. \\
\frac{\epsilon_{AA}}{4} \rho_z \left[\rho_{z+1}(1+m_{z+1}) + \rho_{z-1}(1+m_{z-1}) + 4\rho_z(1+m_z) \right] + \\
\frac{\epsilon_{BB}}{4} \rho_z \left[\rho_{z+1}(1-m_{z+1}) + \rho_{z-1}(1-m_{z-1}) + 4\rho_z(1-m_z) \right] + \\
\frac{\epsilon_{AB}}{2} \rho_z \left[-\rho_{z+1}m_{z+1} - \rho_{z-1}m_{z-1} - 4\rho_z m_z \right] + \\
\left. \frac{V_A(z)}{2} \rho_z - \frac{V_B(z)}{2} \rho_z - \Delta\mu \rho_z \right\} = 0.
\end{aligned} \tag{3.2'}$$

Equations (3.2) may have many solutions which can be classified as maxima, saddle points and minima. Since ρ - \mathbf{m} space is open, that solution with the lowest ω corresponds to the *global* minimum and therefore to the *stable* phase. Again, we shall use the term *phase* \mathcal{P} to refer to a given set of order parameters (ρ, \mathbf{m}) for which ω is minimal *locally*.

3.2 Conditions for Phase Coexistence

Following Sec. 2.4.2 we may observe phase coexistence of *two* phases below the critical point when changing the external fields (i.e., μ or $\Delta\mu$). Hence, we are interested in solutions of Eq. (3.2) satisfying the additional condition

$$\omega(\mu_{12}, \Delta\mu_{12}; \mathcal{P}_1) = \omega(\mu_{12}, \Delta\mu_{12}; \mathcal{P}_2) \tag{3.3}$$

for fixed temperature and pore width n_z . This equation then defines the chemical potentials μ_{12} and $\Delta\mu_{12}$ at coexistence of phases \mathcal{P}_1 and \mathcal{P}_2 .

Such coexistence corresponds to an intersection between the grand potentials of the two phases when plotted as a function of μ while holding $\Delta\mu$ constant (Fig. 3.1(a)) or, accordingly, as a function of $\Delta\mu$ for constant μ (Fig. 3.1(b)). Note, that for each μ and $\Delta\mu$, ω has to be minimized to obtain the solutions of Eq. (3.2) corresponding to phases \mathcal{P}_1 and \mathcal{P}_2 . In both Figs. 3.1(a) and (b), \mathcal{P}_1 is stable at points left of the intersection μ_{12} and $\Delta\mu_{12}$, whereas \mathcal{P}_2 is only metastable. To the right of the fields at coexistence, \mathcal{P}_2 becomes stable and hence \mathcal{P}_1 is only metastable. At μ_{12} or $\Delta\mu_{12}$ the two phases are simultaneously stable and therefore obey the conditions (2.30), that is they are *coexisting*.

In order to compute the intersections, we may calculate the first derivatives of ω

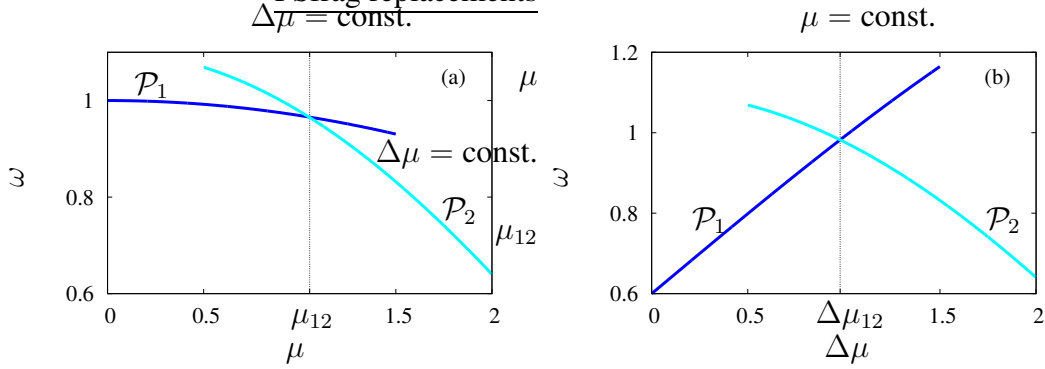


Figure 3.1: Schematic dependence of grand potentials ω of two phases, \mathcal{P}_1 and \mathcal{P}_2 , (a) on the chemical potential μ and (b) on the incremental chemical potential $\Delta\mu$. Fields of coexistence are represented by μ_{12} and $\Delta\mu_{12}$. Note, that all plotted points are local minima of ω .

with respect to μ and $\Delta\mu$, which represent the slopes of plots in Fig. 3.1

$$\begin{aligned} \frac{d\omega}{d\mu} &= \frac{\partial\omega}{\partial\mu} + \sum_{z=1}^{n_z} \frac{\partial\omega}{\partial\rho_z} \frac{d\rho_z}{d\mu} + \frac{\partial\omega}{\partial m_z} \frac{dm_z}{d\mu} \\ \frac{d\omega}{d\Delta\mu} &= \frac{\partial\omega}{\partial\Delta\mu} + \sum_{z=1}^{n_z} \frac{\partial\omega}{\partial\rho_z} \frac{d\rho_z}{d\Delta\mu} + \frac{\partial\omega}{\partial m_z} \frac{dm_z}{d\Delta\mu}. \end{aligned} \quad (3.4)$$

Since the two phases are local minima of ω (i.e., Eq. (3.1) holds) the sums on the right hand side in Eq. (3.4) vanish. From Eq. (2.23) we obtain

$$\begin{aligned} \frac{d\omega}{d\mu} &= \frac{\partial\omega}{\partial\mu} = -\frac{1}{n_z} \sum_{z=1}^{n_z} \rho_z \equiv -\rho \\ \frac{d\omega}{d\Delta\mu} &= \frac{\partial\omega}{\partial\Delta\mu} = -\frac{1}{n_z} \sum_{z=1}^{n_z} \rho_z m_z \equiv -\rho m, \end{aligned} \quad (3.5)$$

where ρ is the (total) mean density on the entire lattice and m measures the total miscibility of the lattice fluid.

3.3 Numerical Procedure

3.3.1 Starting Solutions at Zero Temperature

Consider first a binary mixture at $T = 0$. As already described in Sec. 3.1.1 the overall number of *possible* phases (i.e., local extrema of ω) is finite and easily obtained by

putting $(\rho_z = 0, m_z = 0)$, $(\rho_z = 1, m_z = 1)$, or $(\rho_z = 1, m_z = -1)$ for each lattice layer at z . Then, Eq. (2.23) for $T = 0$ and given n_z, μ and $\Delta\mu$ permits us to calculate ω for each *possible* phase. The lowest value of ω refers to the stable phase.

Since ρ and m are constant for $T = 0$, plots analogous to those in Fig. 3.1 are straight lines (see Eq. (3.5)). Thus, we can determine all intersections easily in order to get the phase coexistences at $T = 0$.

3.3.2 Search for Stable Phases

For $T > 0$ we use Newton's method for solving Eq. (3.2): to find a zero of an one-dimensional function, say $f(x) \equiv 0$, we introduce an iteration scheme

$$x_{i+1} = x_i - \frac{f(x_i)}{f'(x_i)}, \quad (3.6)$$

where a suitable initial guess x_0 is supposed to be available. Now suppose a phase \mathcal{P} corresponds to the solution (ρ, \mathbf{m}) of Eq. (3.1) for a given model parameter set, that is for fixed $T^*, n_z, \mu^*, \Delta\mu^*$ and $\epsilon_{\text{BB}}^*, \epsilon_{\text{AB}}^*, \epsilon_{\text{WA}}^*, \epsilon_{\text{WB}}^*$, we are seeking a solution (ρ', \mathbf{m}') of Eq. (3.1) for a slight variation of this set (e.g. for $T^{*'} = T^* + \delta T$ or $\epsilon_{\text{AB}}^{*'} = \epsilon_{\text{AB}}^* + \delta\epsilon_{\text{AB}}$). If these changes are sufficiently small, (ρ, \mathbf{m}) can be taken as initial guesses for obtaining (ρ', \mathbf{m}') . In other words, we need to trace the local minimum of ω along that variation of the model parameter set. This will be explained in more detail in the following paragraph.

Two-Dimensional Search. Analyzing Eq. (3.2) for a certain value of z , we see that $\partial\omega/\partial\rho_z$ and $\partial\omega/\partial m_z$ are functions of ρ_z, m_z and $\rho_{z\pm 1}, m_{z\pm 1}$. Since the dependence on $\rho_{z\pm 1}$ and $m_{z\pm 1}$ is quadratic at most, $\partial\omega/\partial\rho_z$ and $\partial\omega/\partial m_z$ vary slowly with $\rho_{z\pm 1}$ and $m_{z\pm 1}$. Thus, replacing $\rho_{z\pm 1}$ and $m_{z\pm 1}$ by their initial values from \mathcal{P} gives us good starting solutions to find those values of ρ_z and m_z for which $\partial\omega/\partial\rho_z = \partial\omega/\partial m_z = 0$. This two-dimensional search in ρ_z and m_z for zeros of the two functions (i.e., the minimum of ω) is done by the following iterative procedure in which the values of $\rho_{z\pm 1}$ and $m_{z\pm 1}$ remain fixed.

We calculate the gradient $(g_1, g_2) \equiv (\partial\omega/\partial\rho_z, \partial\omega/\partial m_z)$ at initial values of ρ_z and m_z , which is generally not $(0, 0)$ and compute the zero of $g_1(\rho_z, m_z)$ along the gradient's direction, because it points in the direction of steepest descent of ω . There we use Newton's method given in Eq. (3.6). At this point $g_1 = 0$ and along the direction perpendicular to the gradient of g_1 with respect to (ρ_z, m_z) g_1 remains nearly constant at its value of 0. Thus, we compute the zero of g_2 along the direction $(\partial g_1/\partial m_z, -\partial g_1/\partial \rho_z)$ and find a solution of (ρ_z, m_z) at which $g_2 = 0$. With the new values of (ρ_z, m_z) we solve $g_1 = 0$ along $(\partial g_2/\partial m_z, -\partial g_2/\partial \rho_z)$ by using Newton's method which preserves the value of g_2 at least in first-order terms. Starting again by solving $g_2 = 0$ along $(\partial g_1/\partial m_z, -\partial g_1/\partial \rho_z)$ introduces an iteration scheme which we follow until the two functions, g_1 and g_2 , are simultaneously zero within a precision of 10^{-10} . However,

the iteration scheme Eq. (3.6) and directions require first derivatives of g_1 and g_2 (i.e., second derivatives of ω) with respect to ρ_z and m_z which are given by

$$\begin{aligned}
\frac{\partial g_1}{\partial \rho_z} &= \frac{\partial^2 \omega}{\partial \rho_z^2} = \frac{1}{n_z} \left\{ k_B T \frac{1}{\rho_z - \rho_z^2} + \epsilon_{AA}(1 + m_z)^2 + \epsilon_{BB}(1 - m_z)^2 + \right. \\
&\quad \left. 2\epsilon_{AB}(1 - m_z^2) \right\} \\
\frac{\partial g_1}{\partial m_z} &= \frac{\partial g_2}{\partial \rho_z} = \frac{\partial^2 \omega}{\partial \rho_z \partial m_z} = \\
&\quad \frac{1}{n_z} \left\{ \frac{k_B T}{2} \ln \frac{1 + m_z}{1 - m_z} + \right. \\
&\quad \frac{\epsilon_{AA}}{4} \left[\rho_{z+1}(1 + m_{z+1}) + \rho_{z-1}(1 + m_{z-1}) + 8\rho_z(1 + m_z) \right] + \\
&\quad \frac{\epsilon_{BB}}{4} \left[-\rho_{z+1}(1 - m_{z+1}) - \rho_{z-1}(1 - m_{z-1}) - 8\rho_z(1 - m_z) \right] + \\
&\quad \frac{\epsilon_{AB}}{2} \left[-\rho_{z+1}m_{z+1} - \rho_{z-1}m_{z-1} - 8\rho_z m_z \right] + \\
&\quad \left. \frac{V_A(z)}{2} - \frac{V_B(z)}{2} - \Delta\mu \right\} \\
\frac{\partial g_2}{\partial m_z} &= \frac{\partial^2 \omega}{\partial m_z^2} = \frac{1}{n_z} \left\{ k_B T \frac{\rho_z}{1 - m_z^2} + (\epsilon_{AA} - \epsilon_{BB} - 2\epsilon_{AB})\rho_z^2 \right\}.
\end{aligned} \tag{3.7}$$

Iteration Scheme. The two-dimensional search described above is carried out for all x - y planes, that is for $z = 1, \dots, n_z$, one after another. Unfortunately after that, not all of the *coupled* equations in (3.1) are still satisfied. However, the new values of (ρ, \mathbf{m}) are somewhat closer to the solution. Using them as new initial guesses, we repeat the whole procedure until all $2n_z$ equations in (3.1) are solved simultaneously within a precision of 10^{-10} . This procedure converges because the coupling of the equations is rather weak and if the initial guess of \mathcal{P} is good enough, which can be achieved by making changes in the parameter set (e.g. δT or $\delta\epsilon_{AB}$) sufficiently small. This is very important near critical points where two (or more) minima (i.e., different phases) of ω are very close to each other. Near criticality we limit the search to changes of model parameters to less than 10^{-8} in dimensionless units. This algorithm is used throughout this work.

Search for Phase Coexistences. Suppose now we have a pair of phases, \mathcal{P}_1 and \mathcal{P}_2 , for given initial fields μ and $\Delta\mu$ and fixed T and n_z , we can then trace \mathcal{P}_1 and \mathcal{P}_2 along μ or $\Delta\mu$ which leads to graphs similar to Fig. 3.1. In order to evaluate the intersections, that are points of coexistence, we employ again Newton's method of Eq. (3.6) with $x \equiv \mu$ (or $\Delta\mu$) and $f(x) \equiv \omega(\mathcal{P}_1) - \omega(\mathcal{P}_2)$. Since we know the first derivatives of $f(x)$ from Eq. (3.5) it is easy to employ the iteration scheme given in Eq. (3.6) until the field of coexistence, that is μ_{12} or $\Delta\mu_{12}$, is calculated within a precision of 10^{-10} .

Part II

Theoretical Studies

CHAPTER 4

Bulk Systems

We begin this part with bulk mixtures because their phase behavior is already quite complex on account of the number of parameters by which it is governed. Moreover, bulk mixtures play an important role as a reference for fluids near a single solid wall (see Chapter 5) as well as for confined systems (see Chapter 6). Bulk phase equilibria in mixtures are frequently investigated by means of equations of state. In 1980 van Konynenburg and Scott [2] showed in their pioneering computer work that almost all fluid phase equilibria (gas+liquid, liquid+liquid and even gas+gas) can be generated by the van der Waals equation of state for binary mixtures [3, 91].

In agreement with Furman and Griffiths [4, 92], van Konynenburg and Scott introduced five principal classes of phase diagrams depending on the relative sizes of the molecules and the strengths of their intermolecular interactions. Boshkov [93] (Ree equation), Deiters *et al.* [5, 6] (Redlich-Kwong and Carnahan-Starling-Redlich-Kwong equation), Meijer *et al.* [7, 94] (lattice fluid), Pelt *et al.* [95] (simplified perturbed hard chain theory) extended this classification scheme by introducing a sixth principal class for dipolar mixtures together with a number of subclasses. Although the various possible topologies of phase diagrams were carefully identified, it is not understood precisely which *microscopic* features are responsible for a certain topol-

ogy. Even though more detailed studies were carried out to clarify this issue [10, 12–14, 80, 96–99], these attempts were all limited to rather narrow ranges of molecular parameters by a number of authors. For example, most of these works focused on the behavior of *symmetric* binary mixtures, that is $\epsilon_{\text{BB}}^* = 1$ (i.e., $\epsilon_{\text{AA}} = \epsilon_{\text{BB}}$) and $\Delta\mu = 0$ (i.e., $\mu_{\text{A}} = \mu_{\text{B}}$).

Since the Ising model and the lattice fluid are strongly related to each other [80] one may expect similar phase behavior of the two systems. Studies on ferromagnetic and dipolar fluids showed that this is indeed the case [83, 100–108]. In addition, the impact of polydispersity on the phase behavior of fluid mixtures was discussed [109–111]. Moreover, similar characteristics, such as tricritical or quadruple points, were found in other models [11, 101, 112–114].

Since the parameter space is vast, in this part we only consider binary mixtures characterized by

$$\epsilon_{\text{BB}}^* = 1, \quad (4.1)$$

that is $\epsilon_{\text{AA}} = \epsilon_{\text{BB}}$. In what follows we shall vary only the attraction strength between unlike molecules, ϵ_{AB}^* , as well as the thermodynamic variables T , μ , and $\Delta\mu$. Results for *symmetric* mixtures with $\Delta\mu = 0$ are included in this study for the sake of completeness and will be compared with earlier studies. Before going into more details, the reader should realize that the special case $\epsilon_{\text{BB}}^* = 1$ causes ω in Eq. (4.3) to be invariant with respect to the simultaneous transformation $m \rightarrow -m$ and $\Delta\mu \rightarrow -\Delta\mu$. This symmetry is reflected by all the phase diagrams presented this in chapter.

4.1 Pure Fluid and Calibration

4.1.1 Parameters

To realize a binary bulk mixture, we set $\epsilon_{\text{WA}} = \epsilon_{\text{WB}} = 0$ and $n_z = 1$ and replace the boundary conditions in Eq. (2.24) by the periodic conditions

$$\begin{aligned} \rho &= \rho_0 = \rho_{n_z+1} = \rho_1 \\ m &= m_0 = m_{n_z+1} = m_1 \end{aligned} \quad (4.2)$$

in Eqs. (2.23), (3.2), and (3.7). This yields the grand potential energy density for the bulk mixture

$$\begin{aligned} \omega(T, \mu, \Delta\mu; \rho, m) &= k_{\text{B}}T \left[\rho \ln \rho + (1 - \rho) \ln(1 - \rho) + \right. \\ &\quad \left. \frac{\rho}{2} \left((1 + m) \ln(1 + m) + (1 - m) \ln(1 - m) \right) \right] + \\ &\quad \frac{3\epsilon_{\text{AA}}}{4} \rho^2 (1 + m)^2 + \frac{3\epsilon_{\text{BB}}}{4} \rho^2 (1 - m)^2 + \frac{3\epsilon_{\text{AB}}}{2} \rho^2 (1 - m^2) \\ &\quad - \mu \rho - \Delta\mu \rho m. \end{aligned} \quad (4.3)$$

Dividing this equation by $|\epsilon_{AA}|$ we characterize a binary bulk mixture in the grand canonical ensemble by the interaction parameter ϵ_{AB}^* and by thermodynamic variables T^* , μ^* and $\Delta\mu^*$. We reemphasize that we restrict the study of this entire part to mixtures obeying $\epsilon_{BB}^* = 1$.

4.1.2 Pure Fluid

To model a *pure* bulk fluid (i.e., an one-component fluid) we reduce the number of parameters even further by setting

$$\begin{aligned} \Delta\mu &= 0, \\ \epsilon_{BB}^* &= \epsilon_{AB}^* = 1 \quad (\text{i.e., } \epsilon_{BB} = \epsilon_{AB} = \epsilon_{AA} \equiv \epsilon_{\text{ff}}). \end{aligned} \quad (4.4)$$

Equation(4.3) then simplifies to

$$\omega = k_{\text{B}}T(\rho \ln \rho + (1 - \rho) \ln(1 - \rho)) + 3 \epsilon_{\text{ff}} \rho^2 - \mu\rho, \quad (4.5)$$

where ρ is the (homogenous) density and μ is the chemical potential of the pure fluid. For $\mu/\epsilon_{\text{ff}} = -3$, Eq. (4.5) has a symmetry in $\rho \leftrightarrow (1 - \rho)$, referring to a phase transition from a low-density phase to a high-density phase as long as both phases remain distinguishable, that is as long $\rho \neq 1 - \rho$. Exactly at $\rho_c = 0.5$ this first-order phase transition becomes critical (i.e., of second-order). It is then straightforward to identify $T_c^* = k_{\text{B}}T_c/\epsilon_{\text{ff}} = 1.5$ as the associated critical temperature [115].

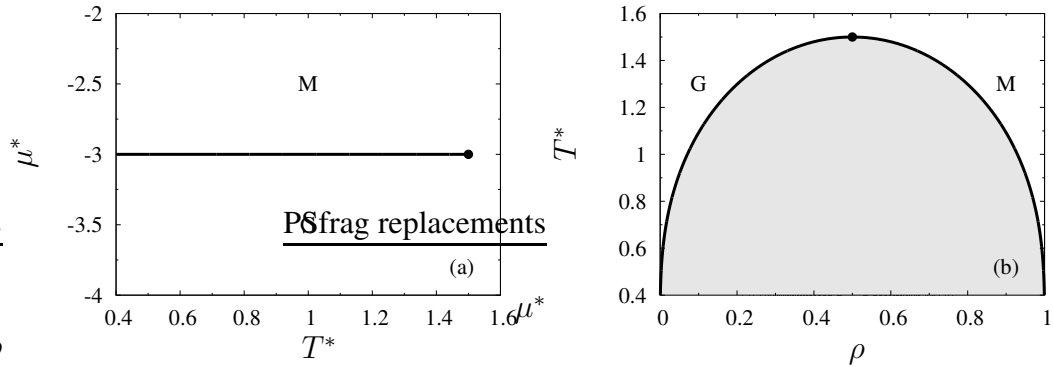


Figure 4.1: Phase diagram of the pure fluid where the solid line refers to phase coexistences between gaseous (G) and liquid (M) phases : (a) T - μ projection; (b) ρ - T projection where the region of phase coexistence is shaded. The critical point (\bullet) is located at $\mu_c^* = -3$, $T_c^* = 1.5$, and $\rho_c = 0.5$.

Using the numerical procedure described in Chapter 3 we can calculate the phase diagram of the pure bulk fluid which is shown in Fig. 4.1 in two different projections. The shaded area in Fig. 4.1(b) is the two-phase region, in which the fluid phase-separates into gaseous (G) and liquid (M) phases. We find that the location of the

critical point is in complete accord with the results obtained by the above symmetry considerations. The symmetry $\rho \leftrightarrow (1 - \rho)$ is also illustrated by Fig. 4.1(b). Figure 4.1(a) shows the corresponding projection of the phase diagram onto the T - μ plane (i.e., the thermodynamic state space). For $T^* < 1.5$ gas and liquid coexist along the horizontal line $\mu^* = -3$ but become indistinguishable at and above the critical point (•).

4.1.3 Calibration of Critical Points

Assuming now the *binary mixture* to be in the mixed state (gas or liquid), that is $m \equiv 0$, we can rewrite Eq. (4.3) in the form of Eq. (4.5) but with

$$\epsilon_{\text{ff}} = \frac{\epsilon_{\text{AA}} + \epsilon_{\text{AB}}}{2}. \quad (4.6)$$

Thus, the mean intermolecular attraction between a pair of molecules of a mixed fluid is given by ϵ_{ff} . This is just the mean value of ϵ_{AA} and ϵ_{BB} because in a perfectly mixed fluid a molecule (A or B) interacts with an equal number of A and B molecules at mean-field level. In this sense ϵ_{ff} , which is given by Eq. (4.6), determines a sensible *natural* energy scale for mixed liquid and gas phases. From the previous discussion of the pure fluid [115] we infer that the coexistence between gas (G) and mixed liquid (M) in the bulk can be mapped onto that between *pure* gas and liquid as long as the condition $m = 0$ is satisfied. Hence, the coexistence line of gas and mixed liquid in the T - μ projection will be a horizontal line parallel to the T -axis for $\mu/\epsilon_{\text{ff}} = -3$ and $\Delta\mu = 0$ ending at $k_{\text{B}}T/\epsilon_{\text{ff}} = 1.5$. Any deviation from this line can therefore be attributed to deviations from perfect miscibility of the pure components. Consequently, we shall express chemical potentials and temperatures in units of $|\epsilon_{\text{ff}}|$ (see Eq. (4.6)), indicated by the plus symbol according to

$$T^+ = \frac{k_{\text{B}}T}{|\epsilon_{\text{ff}}|}, \quad \mu^+ = \frac{\mu}{|\epsilon_{\text{ff}}|}, \quad \Delta\mu^+ = \frac{\Delta\mu}{|\epsilon_{\text{ff}}|}. \quad (4.7)$$

A quantity like ϵ_{AB} , on the other hand, will be expressed in units of ϵ_{AA} following our previously defined units (see Sec. 2.3) and indicated by an asterisk as a superscript (*). The transformation between both energy scales is effected by

$$x^* \rightarrow x^+ = \frac{2}{1 + \epsilon_{\text{AB}}^*} x^*. \quad (4.8)$$

Moreover, we obtain critical temperature and chemical potential of the gas+mixed liquid transition as

$$T_c^+ = 1.5, \quad \mu_c^+ = -3. \quad (4.9)$$

Thus, we stress that for $\epsilon_{\text{BB}}^* = 1$ *all* binary mixtures, that exhibit a gas+mixed liquid critical point, become critical at $T_c^+ = 1.5$ and $\mu_c^+ = -3$ regardless of the values of ϵ_{AB} and ϵ_{AA} .

We note in passing that $\epsilon_{AB}^* > 1$ implies that the attraction between unlike particles is larger than that between like molecules. Hence, the stable state of the fluid is always mixed along the $\Delta\mu = 0$ -axis. That is, the fluid behaves like a pure fluid which is not of central interest in this work. Therefore, we focus exclusively on mixtures characterized by $\epsilon_{AB}^* \leq 1$.

4.2 Phase Behavior of Bulk Mixtures

The aforementioned works by Furman *et al.* [4, 92] revealed that the phase behavior of binary mixtures is rather complex even for the present case of $\epsilon_{BB}^* = 1$. These authors pointed out that this special choice of ϵ_{BB} leads to a complicated phase topology. They called this region *shield region* indicating mixtures which possess tricritical and quadruple points. Additionally, there are a number of different possibilities to present phase diagrams for given model-parameter sets. One possibility is the μ - $\Delta\mu$ - T projection which we discussed already in Sec. 2.4.3. There we found two-dimensional surfaces consisting of points of first-order coexistences between two phases bordered by critical or triple lines. The intersections between such lines or between lines and surfaces are special points, for example tricritical or quadruple points.

Additionally, it is interesting to realize that for $\Delta\mu \rightarrow +\infty$ ($-\infty$) one recovers the phase behavior of the one-component A (B) fluid because the other component is entirely depleted. The corresponding gas+liquid critical points of the one-component A and B fluids are demarcated as C_A and C_B , respectively. From C_A and C_B two critical lines will start when $\Delta\mu$ either decreases from $+\infty$ or increases from $-\infty$, respectively.

In order to identify and characterize phases we also present the ρ - m - T projection which involves the order parameters of coexisting phases. To enhance the clarity of the discussion we will also show isothermal cuts through the phase diagram for selected temperatures. Before we turn to our results we introduce the following color scheme which applies to the remainder of this chapter. Table 4.1 shows the abbreviations

Phase	Gas	Liquid		
		mixed	A-rich	B-rich
Abbreviation	G	M	A	B
Color in ρ - m - T	grey	orange	blue	light blue

Table 4.1: Color and abbreviation scheme for single phases.

of possible single phases used throughout the entire thesis and the correspondingly assigned colors in the order-parameter projection, that is in ρ - m - T space. Since we only present phase coexistences in the phase diagrams, it is then easy to figure out

the character of the involved phases. On the other hand, Table 4.2 introduces the color

Phase coexistence	G+A	G+B	G+M	A+M	B+M	A+B	critical line	tricritical point
Color in μ - $\Delta\mu$ - T	grey		orange			blue	yellow	red dot

Table 4.2: Color scheme for phase coexistences and significant objects based on the abbreviation code for single phases in Table 4.1.

code for conceivable phase coexistences in the μ - $\Delta\mu$ - T projection. Note, that the color codes *vary* between μ - $\Delta\mu$ - T and ρ - m - T projections.

The next four sections are devoted to a discussion of phase diagrams for different values of ϵ_{AB}^* . We label these topologically different types as I, II, and III throughout the remainder of this work. However, it should be noted that this labeling is not in accord with the classification scheme of van Konynenburg and Scott [2] (vKS). However, we shall employ their classification scheme in the following as well for the sake of completeness. In addition, *symmetric* mixtures (i.e., $\Delta\mu = 0$) of all three types are analyzed in the concluding section.

4.2.1 Almost Pure

This trivial case is discussed briefly because it may be considered as a point between the pure fluid and the binary mixture. The only difference between the present case (i.e., $\epsilon_{AB}^* = 1$) and a pure fluid is that for the former $\Delta\mu \neq 0$ whereas $\Delta\mu = 0$ for the latter. Note that in addition we have $\epsilon_{ff} = \epsilon_{AA}$ so that the two energy scales (see Sec. 4.1.3) are identical, that is $T^* = T^+$ etc. Since all interaction-energy terms depending on m in Eq. (4.3) cancel, Eq. (4.3) simplifies to

$$\begin{aligned} \omega(T, \mu, \Delta\mu; \rho, m) &= k_B T (\rho \ln \rho + (1 - \rho) \ln(1 - \rho)) + 3 \epsilon_{ff} \rho^2 - \mu_{art} \rho \\ \text{with } \mu_{art} &\equiv \frac{k_B T}{2} \left((1 + m) \ln(1 + m) + (1 - m) \ln(1 - m) \right) \\ &\quad + \mu - \Delta\mu m \end{aligned} \quad (4.10)$$

which has again the form of Eq. (4.5) but with an artificial chemical potential μ_{art} . Nevertheless this system exhibits phase separation if and only if μ_{art}/ϵ_{ff} assumes a constant value of -3 (see Sec. 4.1.2). Thus, if for certain values of μ , $\Delta\mu$ and m , μ_{art}/ϵ_{ff} equals -3 , the system behaves like a pure fluid at coexistence and the coexisting ρ 's are independent of μ , $\Delta\mu$ and m .

Let us now analyze this latter case in some detail. Figure 4.2 shows the phase diagram in two different projections. In Fig. 4.2(a) we have a *two*-dimensional surface in *three*-dimensional $(\mu, \Delta\mu, T)$ space corresponding to two-phase coexistences between

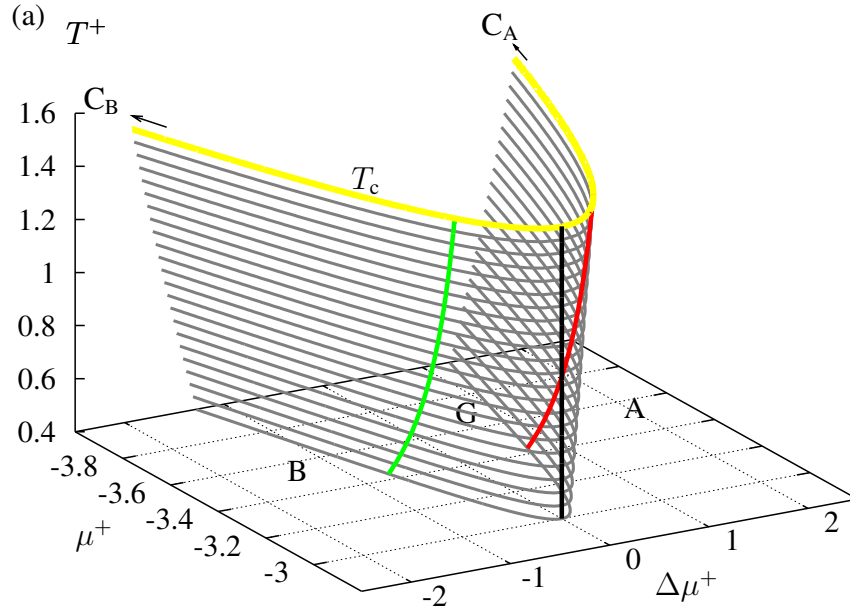


Figure 4.2: Ctnl.

G and either A ($\Delta\mu > 0$) or B ($\Delta\mu < 0$). The upper boundary of that surface is the critical line (yellow) at which both coexisting phases become identical. As mentioned above, for large $|\Delta\mu|$ two critical lines (starting at C_A and C_B , respectively) begin. They represent lines of critical points of one-component fluids consisting of molecules A and B, respectively. The two lines merge at $\Delta\mu^+ = 0$. We see that this line is always parallel to the μ - $\Delta\mu$ plane implying that all critical temperatures assume the same value of $T_c^+ = 1.5$. As expected no liquid+liquid phase transition is found because for the latter to arise asymmetry in the interaction potentials is a necessary prerequisite which is not the case here (i.e., $\epsilon_{AB} = 1$).

The corresponding order-parameter projection (i.e., ρ - m - T) is displayed in Fig. 4.2(b) where gas phases (grey lines) coexist with A-rich (blue lines) or B-rich (light blue lines) liquids. The surface of coexistence points in Fig. 4.2(b) is shaped like a half pipe parallel to the m -axis, thus reflecting that indeed densities of coexisting phases are independent of μ , $\Delta\mu$, and m but still depend on temperature.

In both graphs three examples for systems with constant $\Delta\mu^+$ values of -0.7 , 0 , and 0.7 are indicated by green, black, and red lines, respectively. These lines help to visualize an arbitrary cut at constant $\Delta\mu$ which is the case studied previously [10, 12–14, 84, 109]. The most common approximation is the case of $\Delta\mu = 0$ corresponding to a pure fluid represented by the black line for which $\mu^+ = -3$ and $T_c^+ = 1.5$ (see

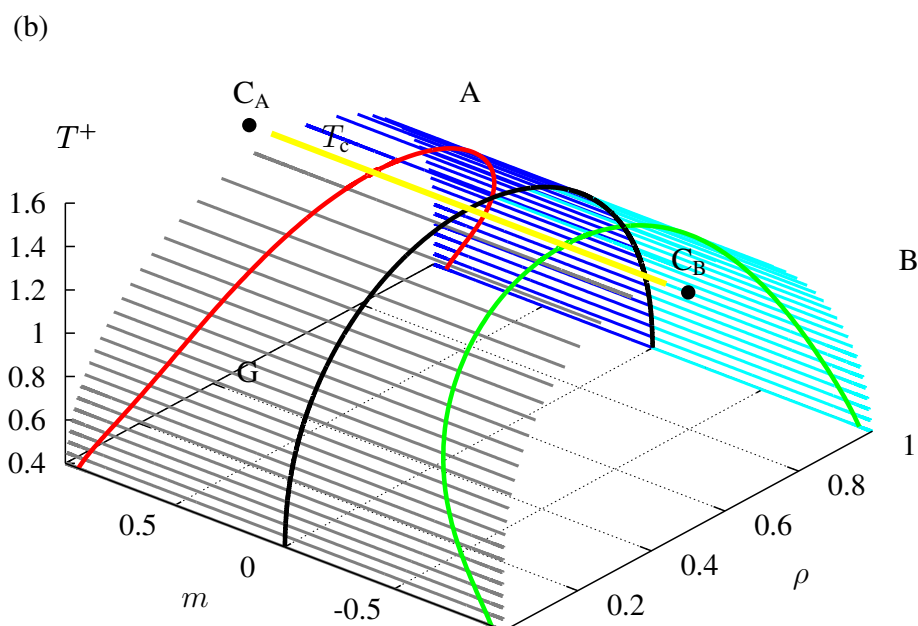


Figure 4.2: Phase diagram of the mixture with $\epsilon_{AB}^* = 1$ where grey and blue lines are isotherms indicating phase coexistences between gas (G), A-rich (A) and B-rich (B) liquids. The yellow line displays the critical line (T_c). (a) μ - $\Delta\mu$ - T projection (color code according to Table 4.2); (b) ρ - m - T projection (color code according to Table 4.1). For three fixed values of $\Delta\mu^+$, namely -0.7 (green), 0 (black) and 0.7 (red), the coexistence lines are shown in both graphs.

Figs. 4.2(a) and 4.1(a)). Accordingly, the corresponding black lines in Figs. 4.2(a) and (b) agree with those in Figs. 4.1(a) and (b), respectively.

Such mixtures belong to the class I of vKS where we find one critical line connecting the two gas+liquid critical points of the pure A and B fluids (i.e., connecting C_A and C_B in Fig. 4.2(a)) in accord with the work of Deiters and Pegg (see Fig. 1 in [5]). In experiments class-I mixtures are usually characterized by $\epsilon_{AB}^* \geq 1$ and therefore remain mixed even at low temperatures. Examples are CO_2+O_2 , $\text{Ar}+\text{Kr}$, N_2+O_2 but of course here $\epsilon_{BB}^* \neq 1$ and the mixtures may be polydisperse, too [116, 117].

4.2.2 Type-I Mixtures

We now introduce a tendency to demix by decreasing ϵ_{AB}^* to a value of 0.6. The resulting phase diagram is shown in Fig. 4.3 in two projections. Again grey and blue lines indicate isotherms of phase coexistences. Let us focus on Fig. 4.3(a) where the μ - $\Delta\mu$ - T projection displays a new first-order phase transition between A-rich and B-

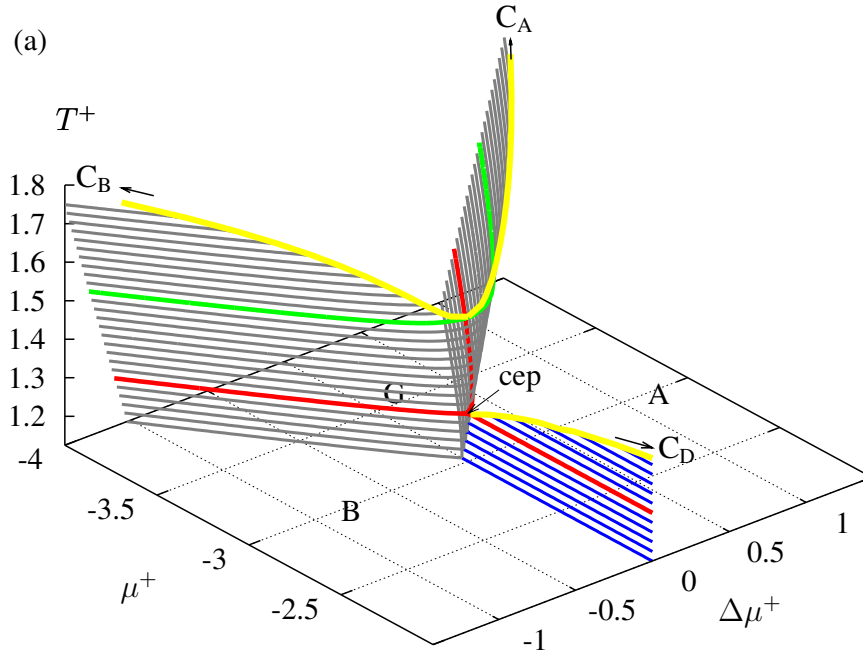


Figure 4.3: Ctnl.

rich liquids for low temperatures indicated by the blue lines. The yellow line above the blue lines demarcates a line of A+B critical points. On account of the symmetry of ω with respect to $\Delta\mu$, this surface of liquid+liquid phase coexistence lies in the plane at $\Delta\mu^+ = 0$. The surface connects to the surface of gas+liquid coexistences (grey lines). Thus, the line of intersections of the two surfaces defines triple points where gas, A- and B-rich liquids are coexisting simultaneously. This triple line ends at the critical end point (cep) at $T_{\text{cep}}^+ = 1.25$, $\mu_{\text{cep}}^+ = -3$ and $\Delta\mu_{\text{cep}}^+ = 0$. There, the A+B coexistence becomes critical but the gas+liquid coexistence remains of first-order. The cep is also the end point of the liquid+liquid (A+B) critical line (starting at C_D) from which this technical term originated.

One should note that for $\epsilon_{AB}^* < 1$ and $\mu \rightarrow \infty$ we always find a liquid+liquid critical point at $\Delta\mu^* = 0$ indicated by C_D because for large μ the gas phase is entirely depleted. Above the liquid+liquid coexistence temperatures (blue lines), the gas+liquid coexistence surface is similar to that for $\epsilon_{AB}^* = 1$ (see Fig. 4.2(a)), but its critical line (upper yellow line from C_A to C_B) has now a minimum at $T^+ = 1.5$ (green isotherm), $\mu^+ = -3$, and $\Delta\mu^+ = 0$, that is critical temperatures of gas+liquid coexistences now depend on both μ and $\Delta\mu$.

This is also apparent when turning to the corresponding order-parameter projection in Fig. 4.3(b) where we see that the former half-pipe shaped gas+liquid coexistence

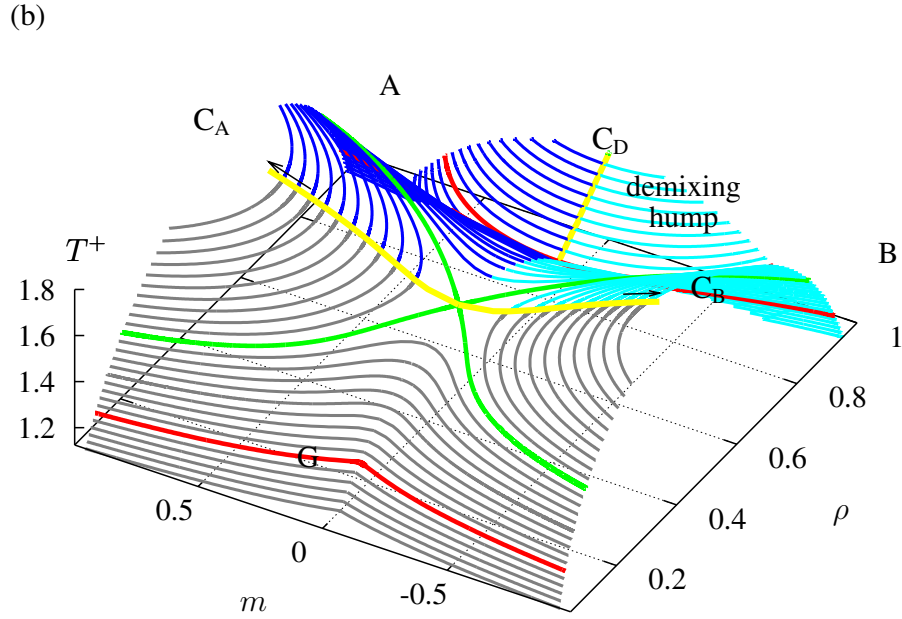


Figure 4.3: As Fig. 4.2 but for $\epsilon_{AB}^* = 0.6$ and two critical lines in yellow. The critical end point (cep) temperature is marked in red. The green line indicates the temperature at which gas+liquid coexistence for $\Delta\mu = 0$ becomes critical. (a) μ - $\Delta\mu$ - T projection; (b) ρ - m - T

surface of Fig. 4.2(b) exhibits an indentation around $m = 0$ indicating that the critical line (yellow line connecting C_A and C_B) varies in temperature. Note, that the saddle point lies at $T^+ = 1.5$, $\mu^+ = -3$, and $\Delta\mu^+ = 0$, and demarcates the critical point of the gas+perfectly mixed liquid coexistence. The isotherm $T^+ = 1.5$ is shown in green in the two projections.

In contrast to Fig. 4.2(b) we observe a demixing ‘‘hump’’ for large densities ρ , where A-rich and B-rich liquids are coexisting (dark and light blue lines in the back of Fig. 4.3(b)). This coexistence surface is symmetric with respect to $m = 0$ as mentioned above and corresponds to the A+B coexistence surface in Fig. 4.3(a). The liquid+liquid transitions are of first-order but become critical at the critical line which lies in the $m = 0$ -plane (yellow line from C_D to cep). The demixing hump touches the gas+liquid surface at the critical end-point temperature of $T_{cep}^+ = 1.25$. The isotherm $T_{cep}^+ = 1.25$ is marked in red in both projections. The cep is also shown in Fig. 4.4(b) where a cut through the ρ - m - T phase diagram for $T_{cep}^+ = 1.25$ is presented. Below this temperature the gas phases at $m = 0$ (cusps of grey lines in Fig. 4.3(b)) coexist with the A-rich (vertexes of blue lines) and the B-rich (vertexes of light blue lines) liquid

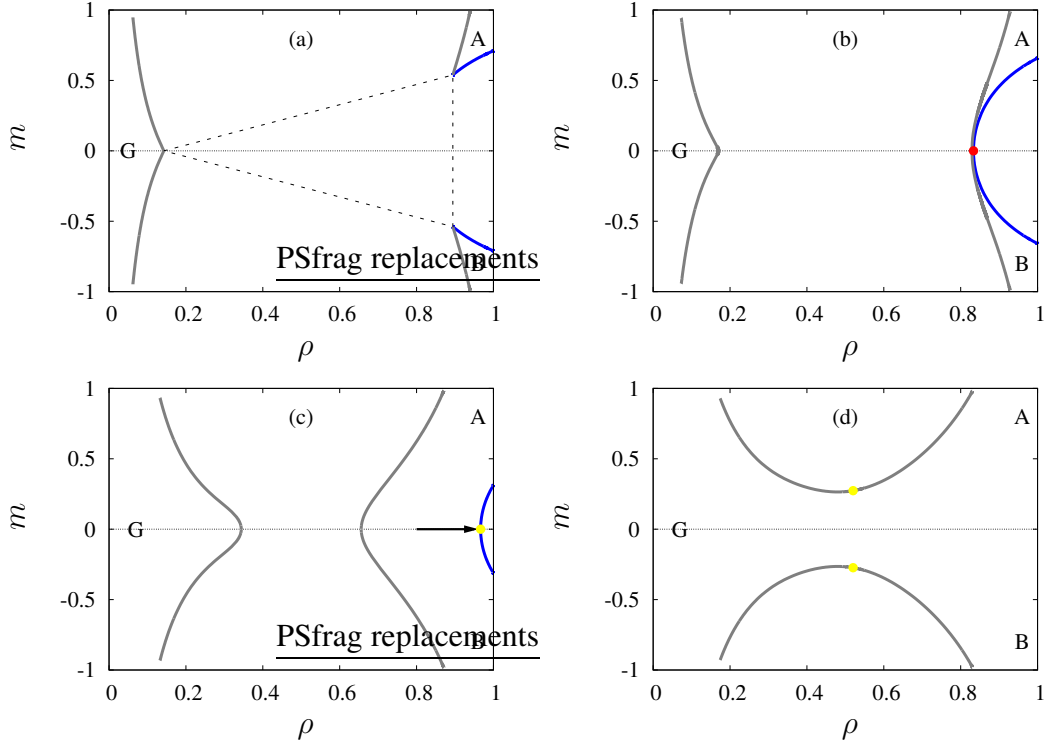


Figure 4.4: Temperature cuts through the phase diagram of $\epsilon_{AB}^* = 0.6$ in Fig. 4.3(b) for (a) $T^+ = 1.20$; (b) $T_{\text{cep}}^+ = 1.25$ where the red dot denotes the cep; (c) $T^+ = 1.45$; and (d) $T^+ = 1.55$. The color code is taken from Table 4.2, where coexistent phases have same colors. Vertices of the dashed triangle indicate coexisting phases at a triple point.

phases. An exemplary triple point is indicated as a dashed triangle in Fig. 4.4(a) for a temperature $T^+ = 1.20$. With increasing temperature those triple points form the triple line (see above). Above $T_{\text{cep}}^+ = 1.25$ the liquid+liquid coexistence (demixing “hump”) detaches from the gas+liquid coexistence and eventually vanishes (above C_D in Fig. 4.3(b)) whereas the gas+liquid coexistences become critical (as can be also seen in Fig. 4.4(c,d)). We shall henceforth refer to such mixtures as type I.

This topology is characteristic for the range $1 > \epsilon_{AB}^* > 0.58$ and belongs to the *symmetric II-A* class of vKS. The van der Waals equation [2] yields such a behavior for $1 > \epsilon_{AB}^* \geq 0.6522$ (see also Fig. 1 in [5]). Based upon a mean-field approach for symmetric mixtures, Wilding *et al.* [12] found this type for mixtures of $1 > \epsilon_{AB}^* \geq 0.72$. More recently, a Monte-Carlo study of Wilding [13] verified this type of mixture for $\epsilon_{AB}^* = 0.7$. An experimental example for a class II-A mixture is the system $\text{CO}_2 + \text{C}_2\text{H}_6$, although the low temperature C_D -cep critical line (see Fig. 4.3(a)) is not seen because it is below the melting curve [116, 117].

Order of Demixing. In experiments, mixtures are normally studied near liquid+liquid coexistence. Therefore, it is interesting to study the transition from mixed to demixed liquid in more detail. Especially, the order of the transition is crucial for classifying real mixtures. In the literature [12, 15] the *order of demixing* refers to a process during which a mixed liquid is compressed until it eventually demixes. Compression-induced decomposition of this sort may be perceived either as a discontinuous (first-order) or continuous (second-order) phase transition. We note that compressing the mixed liquid (i.e., $\Delta\mu = 0$) is equivalent to increasing μ while holding $\Delta\mu = 0$ constant at fixed temperature. This is because the thermodynamic field μ couples to the overall particle density $\rho^A + \rho^B$ whereas $\Delta\mu$ couples to the relative concentration $\rho^A - \rho^B$. Thus, an increase of μ leads to a larger number of molecules per unit volume which can also be perceived as a decrease of the volume while holding the number of molecules fixed.

For $\epsilon_{AB}^* = 0.6$ such an isothermal “compression” is sketched in Fig. 4.4(c) by the arrow. The starting point at $\rho = 0.8$ is the perfectly mixed liquid (i.e., large ρ and $m = 0$). By compression the density increases until one hits the critical (yellow) point of A+B liquid coexistence. Because this critical transition is continuous, the liquid starts to demix gradually along the A+B coexistence curve (blue line). Demixing of second-order is typical for mixtures of $\epsilon_{BB}^* = 1$ that exhibit a critical end point because a first-order mixed+demixed liquid transition at $\Delta\mu = 0$ is never apparent.

This scenario agrees with the qualitative approach of Antonevych *et al.* (see Fig. 3 in [15]), except below T_{cep}^+ their gas+liquid coexistence line at the triple point is not bent as it should (see Fig. 4.4(a) left grey line). Furthermore, Antonevych and co-workers carried out model calculations for symmetric Lennard-Jones mixtures, but did not find continuous (i.e. second-order) demixing even for large $\epsilon_{AB}^* \approx 0.8$ in contrast to our results. We believe their assumed mixed+demixed liquid transition at $T^* = 1$ in [15] is rather a gas+demixed liquid transition which indeed is of first-order in our model as well as Fig. 4.4(a) indicates. Wilding [13] also used Monte-Carlo simulation for symmetric mixtures of $\epsilon_{AB}^* = 0.7$ and verified the appearance of a critical end point which supports our result.

4.2.3 Type-II Mixtures

We now turn to mixtures of type II where we observe a fourth stable bulk phase, namely the mixed liquid state in addition to the previously discussed gaseous, A-rich, and B-rich liquid phases. Let us begin with the phase diagram for $\epsilon_{AB}^* = 0.5$ in the μ - $\Delta\mu$ - T projection shown in Fig. 4.5(a). As before for $\epsilon_{AB}^* = 0.6$ in Fig. 4.3(a), we observe an A+B (liquid+liquid) coexistence (blue lines) along the $\Delta\mu = 0$ -plane contacting the gas+liquid coexistence surface (grey lines) to the left. The line at which the two surfaces intersect represents the line of triple points (G+A+B). This triple line does not end at a critical end point (as for $\epsilon_{AB}^* = 0.6$ in Fig. 4.3(a)) but splits into three new triple lines at a quadruple point marked by the green dot in Fig. 4.5(a). Fig. 4.6(a)

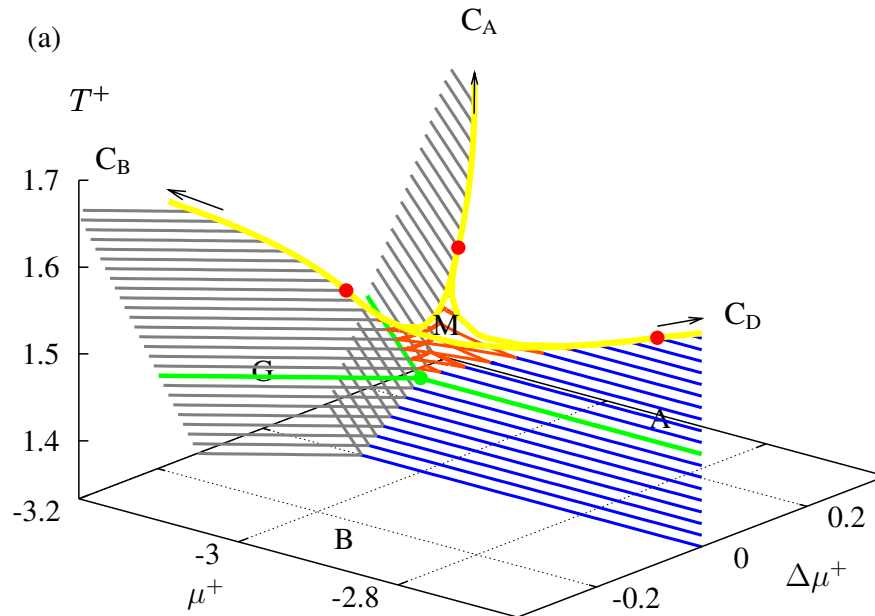


Figure 4.5: Ctnl.

shows an isothermal cut through the quadruple point in the ρ - m projection where gas, A-rich and B-rich liquids coexist with the mixed liquid (M). The three triple lines in Fig. 4.5(a) represent therefore lines of triple points between G+M+A, G+M+B, and M+A+B, respectively. Thus, the orange surface refers to first-order phase transitions between mixed liquid and either gas, A-rich or B-rich liquid. Figure 4.5(a) also shows that each triple line ends at a corresponding tricritical point (red dots) where all three phases become critical simultaneously. Above the tricritical temperature all coexistences involving M vanish. But below, first-order A+M and B+M phase transitions distinguish this mixture from one of type I. This complex phase behavior is also reflected by the interplay of the critical lines. Each critical line starting at the limiting points, namely C_A , C_B , and C_D , bifurcates into two other critical lines at the corresponding tricritical points (red dots in Fig. 4.5(a)).

The equivalent phase diagram in the ρ - m - T projection is shown in Fig. 4.5(b). Four cuts through this projection are given in Fig. 4.6. Because of the decrease of ϵ_{AB}^* to 0.5, the demixing “hump” (A+B) is enlarged whereas the gas+liquid “half pipe” is even more distorted at $m = 0$ compared to Fig. 4.3(b). Thus, between both surfaces a valley emerges (orange) in which a new mixed liquid phase (M) is thermodynamically stable. The term *mixed liquid* is used for M because $|m|$ is always small and ρ is fairly large (see for example Fig. 4.6(b)). The minimum of that valley marks the quadruple point’s

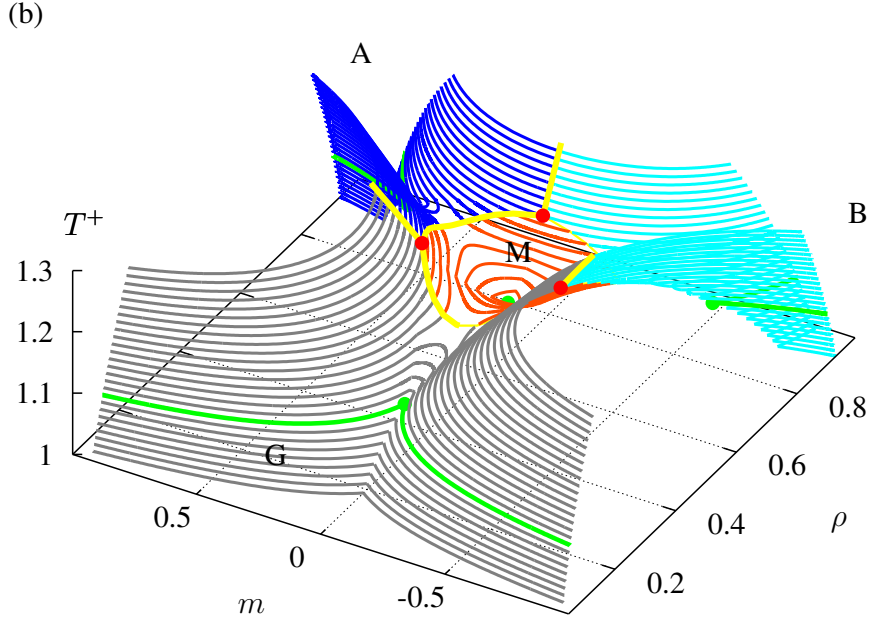


Figure 4.5: As Fig. 4.3 but with $\epsilon_{AB}^* = 0.5$. Red dots show tricritical points. The green lines indicates the quadruple point's temperature. (a) μ - $\Delta\mu$ - T projection with additional M+G, M+A, M+B (all in orange) first-order phase transitions. The green dot (intersection of green lines) represents the quadruple point. (b) ρ - m - T projection with the mixed liquid in orange.

temperature at $T_{\text{qua}}^+ = 1.44$. The quadruple point, which is shown in Fig. 4.6(a) by the dashed lines, is also indicated by four green points in Fig. 4.5(b). Below its temperature (green line in Fig. 4.5(b)) we see phase transitions between gas (G) and demixed liquids (A or B) similar to those observed for $\epsilon_{AB}^* = 0.6$, whereas above that green line in Fig. 4.5(b) we have three different phase transitions surfaces, namely G+M, M+A, and M+B, which become critical at the yellow (critical) lines, respectively. Each pair of such critical lines ends at one of the three tricritical points (red dots) all at $T_{\text{tcp}}^+ = 1.55$. Above that tricritical temperature the mixed liquid cannot be distinguished from neither gas, A-rich nor B-rich liquids. In addition, above $T_{\text{tcp}}^+ = 1.55$ we observe phase coexistences only for strong fields (i.e., large $|\Delta\mu|$ or $|\mu|$ in Fig. 4.5(a)). For $\Delta\mu \rightarrow \pm\infty$, we observe the one-component A and B fluids with their critical points at C_A and C_B , respectively. For $\Delta\mu = 0$ and $\mu \rightarrow \infty$, on the other hand, we have dense liquid A+B coexistence.

Type-II mixtures pertain to the *symmetric III-A** class of vKS. However, from [5] such a mixture can also be considered as a transition state between subclasses IV* and

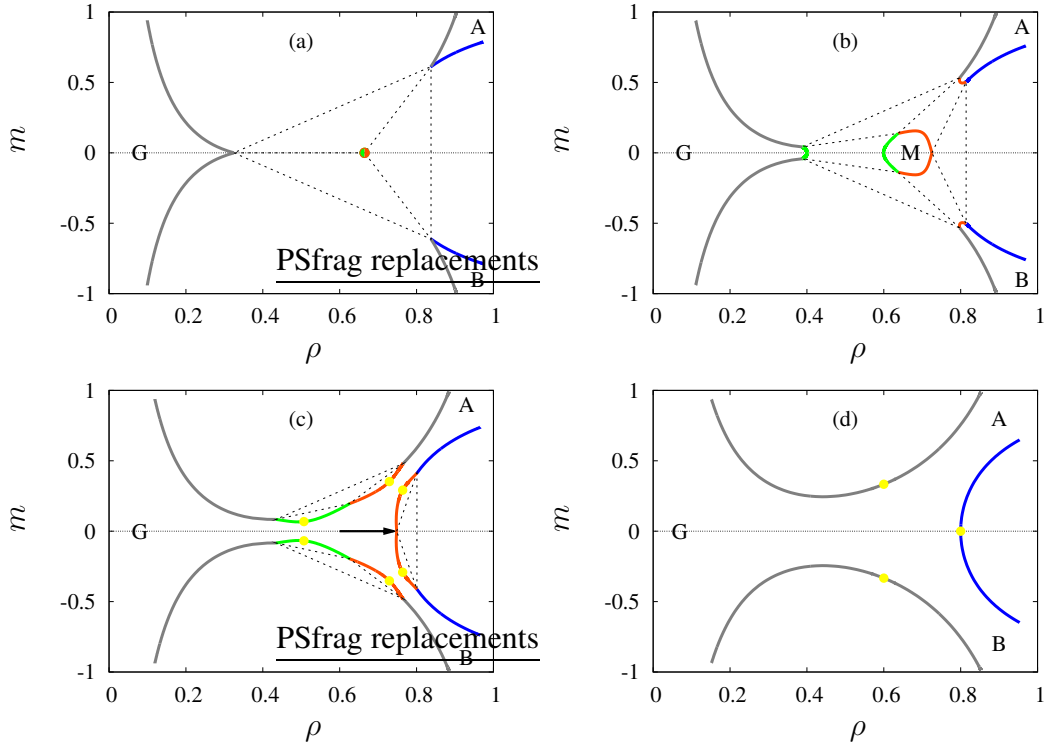


Figure 4.6: As Fig. 4.4 but for $\epsilon_{AB}^* = 0.5$ (color code from Table 4.2), (a) $T_{\text{qua}}^+ = 1.44$; (b) $T^+ = 1.48$; (c) $T^+ = 1.51$; and (d) $T^+ = 1.6$.

IV₄ as Fig. 14 in [5] shows. We observe this type for values of $0.58 \geq \epsilon_{AB}^* > 0.4$ in accordance with Wilding *et al.* [12] who reported type-II mixtures for the range $0.71 > \epsilon_{AB}^* \geq 0.605$. Experimental examples for classes III and III_m are He+Xe, Ne+Kr, CH₄+*n*-C₇H₁₆, and CO₂+*n*-C₁₃H₂₈ which of course may be highly asymmetric [116, 117].

Order of Demixing. Further inspection of Fig. 4.5 reveals that a mixed liquid (M) apparently coexists with other phases only above the quadruple point, that is at $T > T_{\text{qua}}^+ = 1.44$. This isotherm is represented by green lines in Fig. 4.5. An isothermal compression of the mixed liquid is then effected by changing its thermodynamic state along (and in the direction of) the arrow shown in Fig. 4.6(c) at $T^+ = 1.51$. At the point where it intersects the two coexistence lines of M+A and M+B, that is at the triple point marked by the dashed triangle, the mixture decomposes spontaneously into A- and B-rich liquids as indicated by the discontinuous change in both ρ and m at this triangle. Further compression leads to the usual A+B coexistence along the blue lines in Fig. 4.6(c).

A qualitatively similar scenario was suggested by Antonevych *et al.* (see Fig. 4(a) in [15]) who, however, missed the M+A+B triple point. Antonevych *et al.* also surmised that critical end points may be found for $\Delta\mu \neq 0$ and larger temperatures (see

Fig. 4b in [15]). Our results do not support that notion. Instead the situation seems more likely to be similar to that depicted in Fig. 2 of the paper by Antonevych *et al.* .

For temperatures above the tricritical point $T_{\text{tcp}}^+ = 1.55$ (see Fig. 4.6(d)) the situation is similar to that of $\epsilon_{\text{AB}}^* = 0.6$ (see Fig. 4.4(c)) where the demixing transition is of second-order. All mixtures showing first-order liquid+liquid *and* gas+mixed liquid transitions pertain to the type II.

4.2.4 Type-III Mixtures

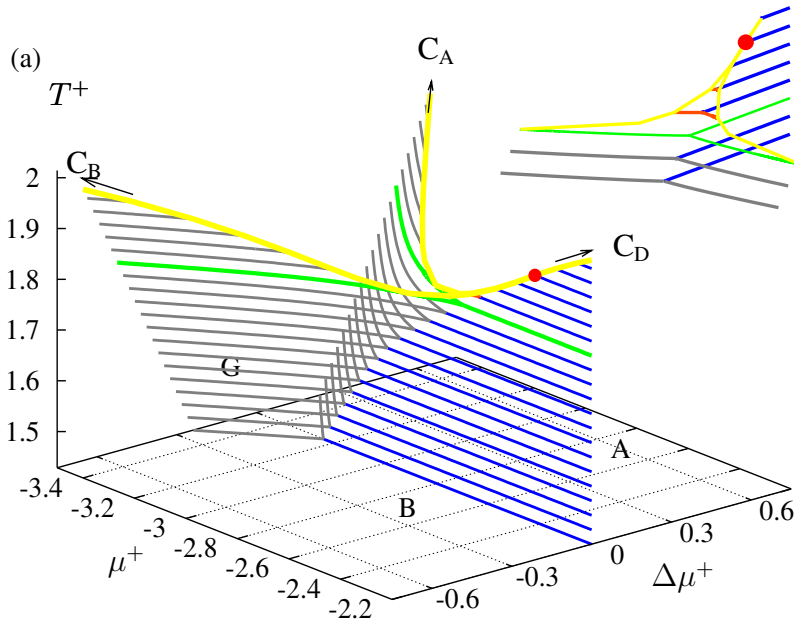


Figure 4.7: Ctnnd.

Consider now an even smaller value of $\epsilon_{\text{AB}}^* = 0.4$ for which binary mixtures exhibit a strong tendency to decompose even for low densities. Analyzing the phase diagram in the μ - $\Delta\mu$ - T projection in Fig. 4.7(a), we see that the liquid+liquid coexistence surface (blue lines) reaches values far below $\mu^+ = -3$, at which the pure fluid is already in the gas phase. In addition, we do not observe any mixed liquid phase for moderate temperatures below $T^+ = 1.8$ marked by green lines. For $T^+ \leq 1.8$ we have gas+demixed liquid coexistences (grey lines) and A+B coexistences (blue lines). The intersection between the two surfaces defines a triple line similar to the previously discussed cases $\epsilon_{\text{AB}}^* = 0.6$ and $\epsilon_{\text{AB}}^* = 0.5$. However, here the triple line appears to

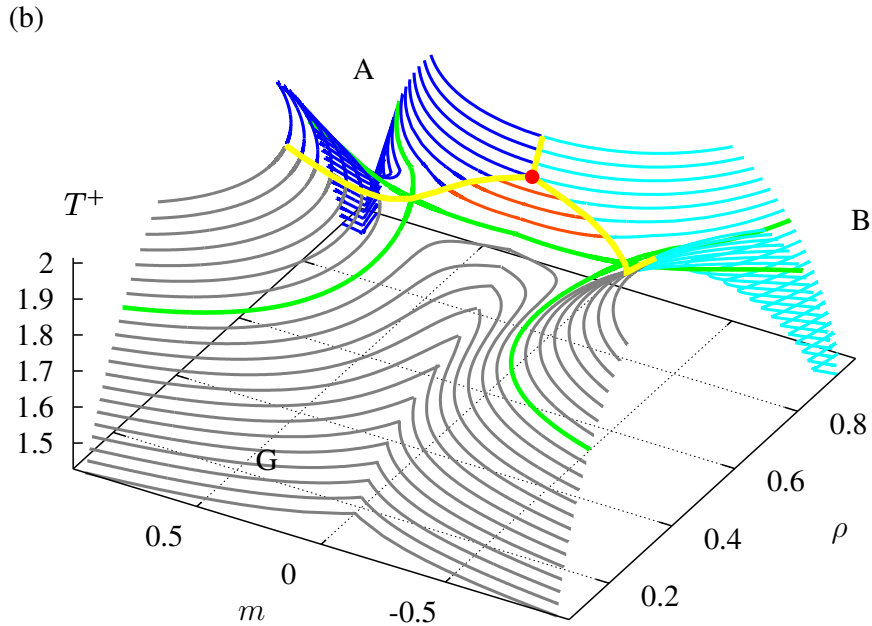


Figure 4.7: As Fig. 4.3 but with $\epsilon_{AB}^* = 0.4$ and the tricritical point in red. The green line marks the lowest critical temperature. (a) μ - $\Delta\mu$ - T projection, where the region near the tricritical point is turned and enlarged above; (b) ρ - m - T projection.

be more bent. Two examples of such temperatures are shown in Figs. 4.8(a) and (b) (i.e., $T^+ = 1.6$ and $T^+ = 1.79$, respectively) which point out the character of the triple points, namely G+A+B. Nevertheless, in Fig. 4.7(a) the triple line ends at the tricritical point at $T_{\text{tcp}}^+ = 1.91$ (red dot) where also the two gas+demixed liquid critical lines (yellow lines coming from C_A and C_B) meet and become a single liquid+liquid critical line as μ^+ increases above $\mu_{\text{tcp}}^+ = -2.4$ (yellow line bounding the blue surface from above). At the tricritical point the three critical lines coming from C_A , C_B and C_D have a common tangent which is unique for this type.

The enlargement in Fig. 4.7(a) reveals that for a short temperature range (between the green isotherm and the tricritical temperature) mixed+demixed liquid coexistences (orange) appear. This can be seen more clearly in Fig. 4.7(b). Moreover, the demixing “hump” in Fig. 4.7(b) is even more enlarged so that the valley pertaining to mixed liquid phases (orange in Fig. 4.5(b)) has disappeared because the mixed liquid phase is metastable at most except for the small orange area. However, the G+M critical point vanishes. The two dominant G+A and G+B coexistences become critical at the yellow lines for $m \neq 0$, both having a minimum at $T^+ = 1.8$ (green isotherm). Above $T^+ = 1.8$ the two G+A and G+B coexistences detach (see also Fig. 4.8(c)) so that four

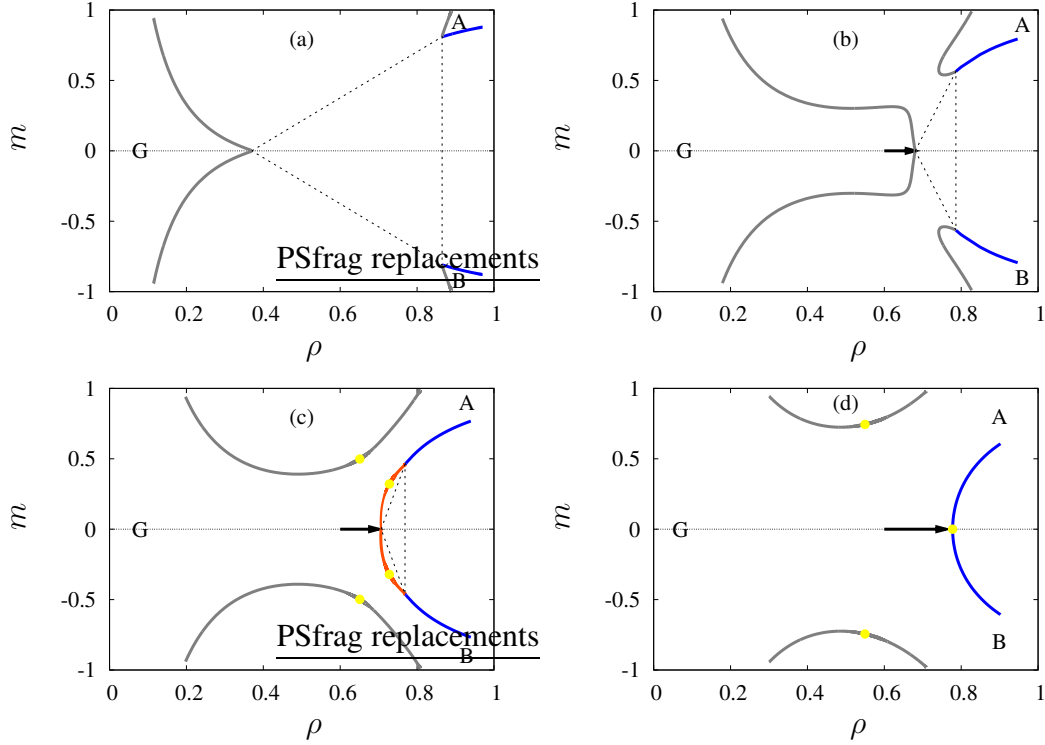


Figure 4.8: As Fig. 4.6 but for $\epsilon_{AB}^* = 0.4$. (a) $T^+ = 1.6$; (b) $T^+ = 1.79$; (c) $T^+ = 1.83$; and (d) $T^+ = 2$.

critical points for fixed temperature appear. For higher temperatures those two lying at the demixing “hump” join the A+B critical line from below at the tricritical point (red dot in Fig. 4.7(b)), that is $m = 0$ and $T_{icp}^+ = 1.9$ as discussed above.

Such a phase behavior is also found by Keskin *et al.* in Figs. 1 and 5 in [7] for $\epsilon_{AB}^* = 0.333$, and by Wilding *et al.* [12] for $0.605 \geq \epsilon_{AB}^*$. It corresponds to the *symmetric III-HA* class (or *III-HA_m*) of vKS. A qualitatively similar phase behavior was reported by Deiters and Pegg [5]. In Fig. 7 in [5] these authors considered this type of mixture as a transition point between classes II and III of vKS. They called the tricritical point “symmetric” because it is only found for $\Delta\mu = 0$ and $\epsilon_{BB}^* = 1$. Such mixtures which do not show a stable gas+mixed liquid critical point refer to mixtures of type III according to our classification scheme. In the present thesis we find type-III mixtures for $0.4 \geq \epsilon_{AB}^* \geq 0$.

Order of Demixing. This mixture does not exhibit a gas+mixed liquid coexistence but gas at coexistence with A and B at $m \approx 0$ becomes continuously denser with rising temperature as can be seen in Figs. 4.8(a) and (b). For example the mixed phase (i.e., $m = 0$) at the triple point (dashed triangle) in (b) has a density of 0.68 which is already a liquid. Isothermal compression of such mixed liquid phase as indicated by the arrows in Figs. 4.8(b) and (c) leads to a decomposition into A-rich and B-rich liquids at the

triple point. Thus, we observe demixing of first-order. However, above the tricritical temperature of $T_{\text{tcp}}^+ = 1.9$ this transition becomes second-order as shown in Fig. 4.8(d), similar to cases of $\epsilon_{\text{AB}}^* = 0.6$ (see Fig. 4.4(c)) and $\epsilon_{\text{AB}}^* = 0.5$ (see Fig. 4.6(d)).

4.2.5 Symmetric Mixtures

The *symmetric* binary mixture may be perceived as a special case of the systems previously discussed. It is realized by imposing the symmetry constraint

$$\Delta\mu = 0, \quad (4.11)$$

that is setting $\mu_{\text{A}} = \mu_{\text{B}}$. This condition leads phase coexistences to be represented by lines rather than surfaces in the T - μ space similar to pure fluids. In other words, we focus on cuts along $\Delta\mu = 0$ through the previously discussed three-dimensional μ - $\Delta\mu$ - T phase diagrams. Condition (4.11) also implies symmetry of ω with respect to $m \leftrightarrow -m$ (see Eq. (4.3)). It is important to realize that therefore a (demixed) A-rich phase \mathcal{P} (i.e., $m(\mathcal{P}) > 0$) with density ρ coexists *always* with its analog (demixed) B-rich phase \mathcal{P}' of the same density but $m(\mathcal{P}') = -m(\mathcal{P}) < 0$. Thus, we use the term *demixed* phase for a first-order phase coexistence of A-rich and B-rich phases (A+B).

Phase diagrams may be plotted in various projections. The most common ones are those in T - μ , and ρ - T space equivalent to the pure fluid (see Fig. 4.1). The disadvantage of the ρ - T projection is that the order parameter m (i.e., the miscibility) is not shown so that liquid+liquid coexistences are not fully characterized. The T - μ phase diagram, on the other hand, is easily obtained by taking a cut $\Delta\mu = 0$ through the previously discussed (general) phase diagrams. Because the resulting ρ - T projection is slightly more complex we display also the full ρ - m - T diagram for $\Delta\mu = 0$ in order to illustrate demixed phases.

Type-I Mixtures. We begin with mixtures for which $\epsilon_{\text{AB}} = 0.6$ (see Fig. 4.3) and show results for the symmetric mixture in Fig. 4.9. In Fig. 4.9(b) we see the T - μ projection where for temperatures below the critical end point (thin line) the gas (G) coexists with the demixed liquid (A+B) along the dashed triple line. All order parameters, ρ and m , of the three phases are shown in (c) where one can see that the densities of the liquids along the triple line are the same, but that they differ in m . However, the A+B coexistences above the critical end point are not shown in Fig. 4.9(c) for the sake of clarity. They can be inferred from Fig. 4.3(b) as the demixing “hump” above the red isotherm. Only the critical line of that A+B coexistence is shown as the dotted λ -line.

The usual ρ - T graph in Fig. 4.9(a), which is a two-dimensional projection of Fig. 4.9(c) omitting the m -axis, also visualizes this triplet coexistence. Above the cep the liquid phase (M) coexisting with the gas is now mixed (i.e., $m = 0$) and we have only two-phase coexistence (solid line). This follows because for $\epsilon_{\text{AB}}^* = 0.6$ mixing of liquid phases is favorable already for low temperatures where the liquid+liquid coexistence (A+B) become critical along the λ -line represented by the dotted line in Fig. 4.9 (see

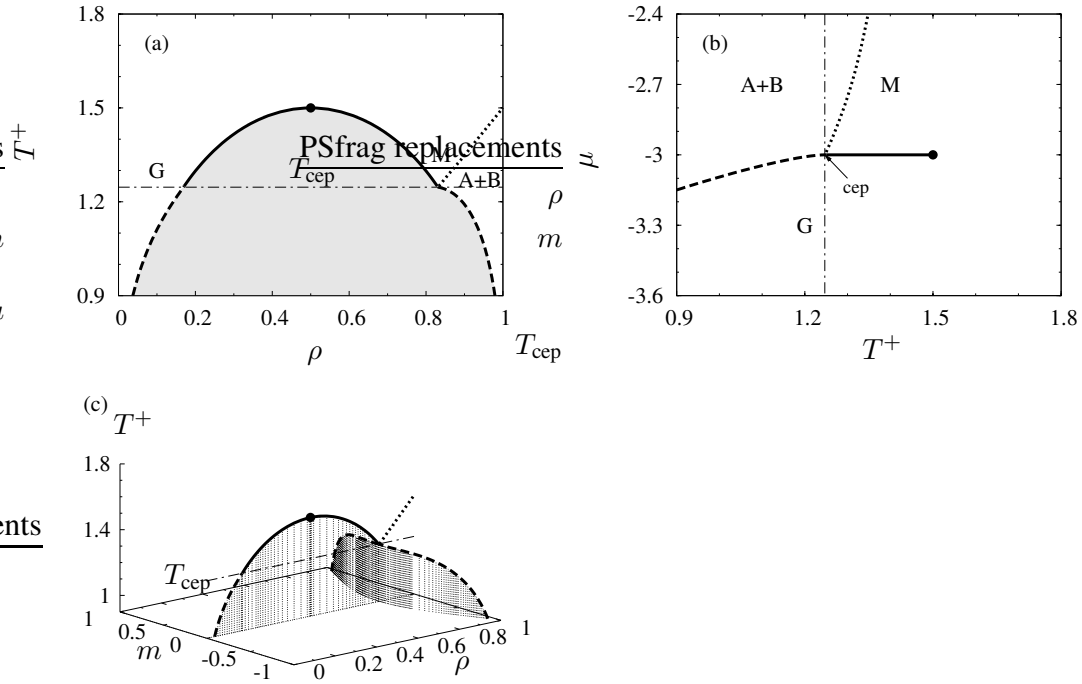


Figure 4.9: Phase diagram of a symmetric mixture with $\epsilon_{AB}^* = 0.6$. Solid and dashed lines refer to first-order coexistences between two and three phases, respectively. The critical line (λ -line) is dotted. The thin line marks the critical end point temperature. The dot represents the gas+mixed liquid critical point. (a) ρ - T projection; (b) T - μ projection; (c) ρ - m - T projection, where first-order A+B coexistences are omitted above T_{cep} .

also the yellow line above the blue ones in Fig. 4.3(a)). Thus, an isothermal transition from mixed to demixed liquid (i.e., by crossing the λ -line) is always second-order. Mixtures that only exhibit demixing of second-order are of type I. This type of mixture resembles the one discussed by Wilding *et al.* in their Fig. 2(a) [12] and agrees with the results of Kahl *et al.* [14] and Dietrich *et al.* [32]. The interesting critical end point behavior was studied by Fisher [118, 119] and Wilding [9, 10, 13] because at this point two phases (i.e., A and B) are critical but coexist with a non-critical gas. Additionally, mixtures with critical end points are also observed in dipolar mixtures [106].

Type-II Mixtures. We now turn to mixtures where we already observed a quadruple point for the case of $\epsilon_{AB}^* = 0.5$ in Sec. 4.2.3. Fig. 4.10 shows three projections of the phase diagram which differ qualitatively from the previous ones in Fig. 4.9. In Fig. 4.10(b) the triple line (dashed) of G+A+B coexistence ends at the quadruple point (quad), whose temperature T_{quad} is demarcated by the thin line, and bifurcates into the M+A+B triple line and the solid line which represents the two-phase coexistence of gas and mixed liquid. The latter G+M coexistence ends at the critical point (\bullet).

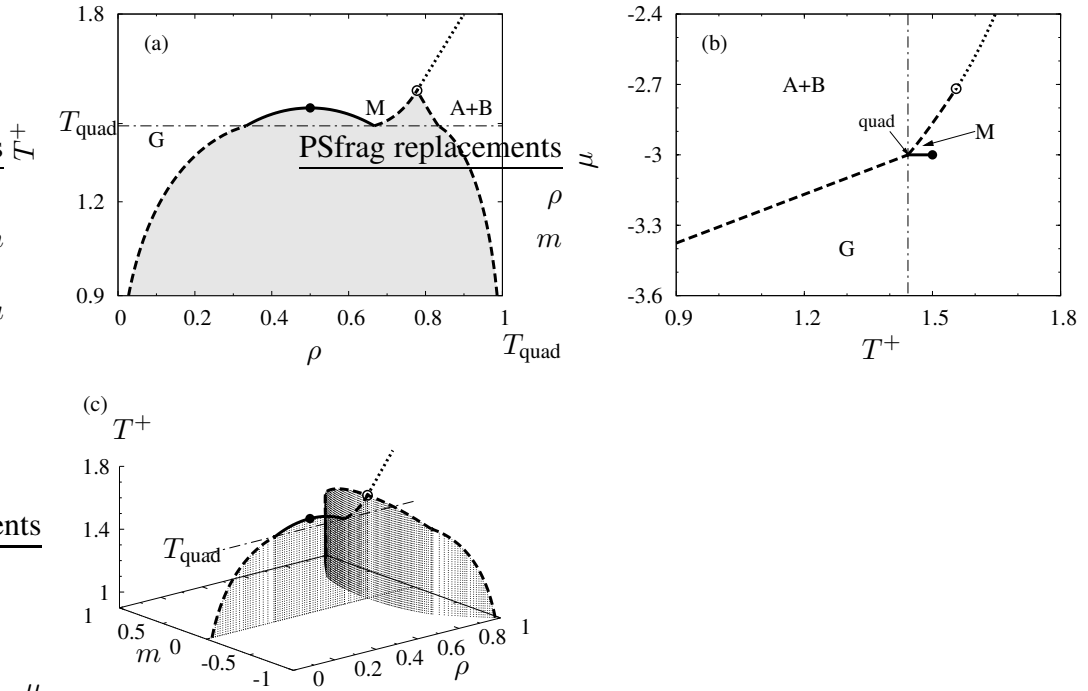


Figure 4.10: As Fig. 4.9 but for $\epsilon_{AB}^* = 0.5$. The thin line marks the temperature of the quadruple point. The tricritical point is indicated by the open dot (\circ).

On the other hand, the three coexisting phases (M, A, and B) are in the liquid state, because their densities are larger than 0.5 (see Fig. 4.10(a)) and become all critical at the tricritical point (\circ). Above its temperature only dense demixed liquids are in coexistence and mix via second-order transitions indicated by the dotted λ -line.

For this type of mixtures we observe first-order demixing below the tricritical point. These results agree with other studies [12, 14, 77, 120]. Again, dipolar mixtures show a similar behavior including a gas-liquid critical point and a disordered+ordered transition for dense liquids [106] similar to the mixed+demixed transition in this work.

Type-III Mixtures. Finally, we discuss those mixtures that do not exhibit a gas+mixed liquid phase transition. We focus on $\epsilon_{AB}^* = 0.4$ as in Sec. 4.2.4 for which the resulting cuts of phase diagrams along $\Delta\mu = 0$ are shown in Fig. 4.11. The rather unspectacular behavior is a consequence of the strong tendency to demix which leads to an absence of dense mixed phases. In Fig. 4.11(b) we see that for temperatures below the tricritical point (\circ) the gas coexists with the A- and B-rich liquids along the dashed triple line. The now metastable gas+mixed liquid critical point (\bullet), which is again at $T_c^+ = 1.5$ and $\mu^+ = -3$, is buried deep inside the demixed liquid region. This can also be seen in the other projections. At the tricritical point all three phases become critical and the triple line is converted into a critical line of A- and B-rich liquid

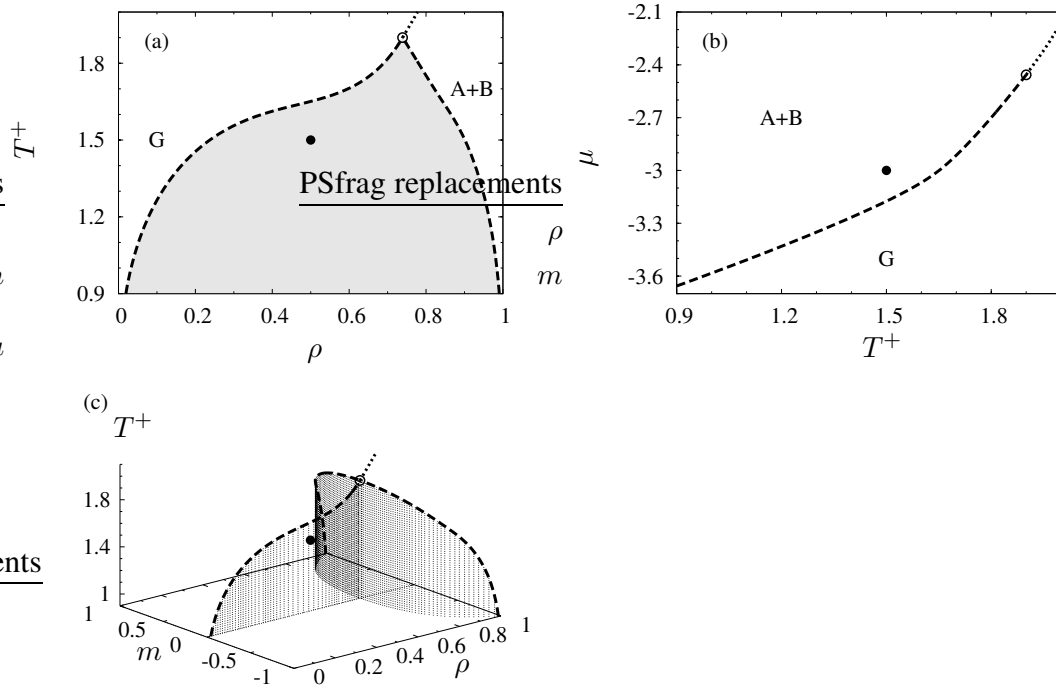


Figure 4.11: As Fig. 4.9 but for $\epsilon_{AB}^* = 0.4$. The gas+liquid critical point (\bullet) is now metastable.

coexistence (dotted λ -line).

These mixtures of type III are found frequently. Our results agree with the theoretical findings of Wilding *et al.* [12] as well as with experimental results for $^3\text{He}+^4\text{He}$ liquid mixtures [121, 122] which exhibit such behavior, too. In the latter case superfluid ^4He -liquid corresponds to our demixed liquid (A+B) and the $^3\text{He}+^4\text{He}$ coexistence to the gas+demixed liquid. The λ -line represent super-fluid transitions¹

In 1977 Hemmer and Imbro [100] showed that a tricritical point may be found in ferromagnetic fluids. Ferroelectric (ordered) liquids (i.e., spin up and down) without external magnetic field can be mapped as coexistence of demixed (A- and B-rich) fluids in the present context whereas isotropic phases correspond to the mixed ones in this study. Therefore, extensive studies on Stockmayer [83, 101, 102, 108] and Heisenberg fluids [103, 105–107] showed that these fluids indeed exhibit a similar phase behavior [83, 101–103, 105–108] not even to type-III mixtures but also to type I and II (see [106] for a review).

Our results for symmetric binary bulk mixtures provide a basis for the next two Chapters. For example, in Chapter 5 we shall discuss wetting of a single, nonselective solid wall by a symmetric binary mixture. It is noteworthy that here the phase diagram

¹The shape of the heat capacity peak in pure ^4He when passing the superfluid transition gave rise to the term “ λ -line”, e.g. in [121].

does not change because the system is still (semi-)infinite. However, film phases adsorbed at the wall arise that depend on the type of the mixture (I-III) and the strength of the fluid–wall attraction. In Chapter 6, on the other hand, we study symmetric binary mixtures *confined* by nonselective solid substrates (slit pore). There we discuss the influence of the degree of confinement (i.e., pore width and fluid–substrate interaction strength) on the phase behavior of binary mixtures.

Wetting of a Planar Solid Surface by Fluids Near Gas+Liquid Coexistence

The study of wetting phenomena has a long history going back all the way to the works by Young [21] and later on by Dupré [22] who analyzed the interaction of fluids with solid surfaces from a macroscopic perspective. In their analyses the contact angle θ (see Fig. 5.1(a)) of a sessile droplet on a solid surface was linked to various interfacial tensions such that if $\theta = 0$ one has *complete* wetting (Fig. 5.1(b)), that is a *macroscopic* film of liquid spreading over the entire substrate. If, on the other hand, one is dealing with stable droplets, $0 < \theta < \pi$ which is the case usually referred to as *partial* wetting (Fig. 5.1(a)). Since then a lot of experimental and theoretical work was devoted to study the wetting of solid surfaces by fluid matter (for reviews see [28, 123–127])¹.

Wetting Classes. Imagine now a film adsorbed at the surface. Then the local density ρ depends only on z eventually approaching the bulk gas density ρ_{bulk} for sufficiently large z . Besides the film thickness a commonly used *integral* order parameter which measures the amount of adsorbed particles is the excess coverage Γ . For a fixed ther-

¹for fundamental experimental studies see these reviews

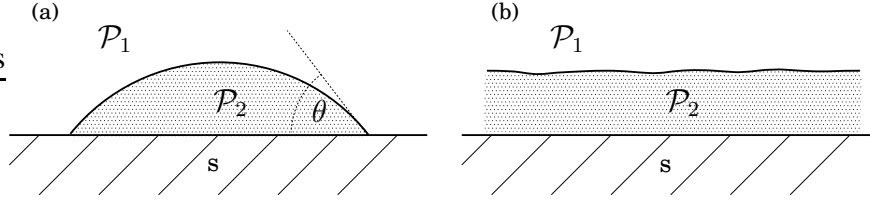


Figure 5.1: Sketch of a contact angle θ between two phases \mathcal{P}_1 and \mathcal{P}_2 in contact with a solid substrate: (a) partial, (b) complete wetting.

modynamic state it is defined by

$$\Gamma \equiv \int_0^\infty (\rho(z) - \rho_{\text{bulk}}) dz \quad (5.1)$$

and is frequently measured in experimental studies [62]. Note that $\Gamma \approx \rho_{\text{liq}} l$, where ρ_{liq} is the bulk liquid density, and thus Γ is of the order of the number of adsorbed layers l ($\rho_{\text{liq}} \approx 1$).

One of the first attempts to classify systems with respect to their wetting behavior is the study by Dash, who analyzed experimental sorption isotherms of physisorbed gases [23]. Since Dash [23] first showed that the amount of adsorption Γ is specific with regard to a given experimental system, pressure P , and temperature T , the introduction of a classification scheme of wetting scenarios is sensible. Such a scheme comprises three main classes (see Fig. 5.2(a)). In class-1 systems gas pressure isotherms rise

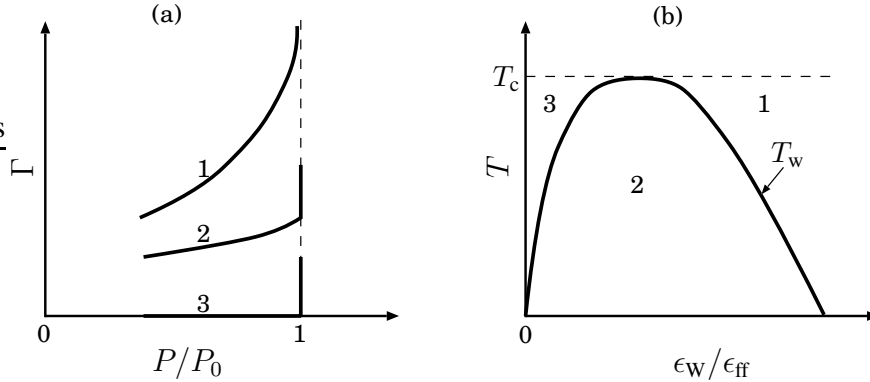


Figure 5.2: (a) Schematic vapor-pressure isotherms illustrating the three main wetting classes (taken from [23]). (b) Schematic wetting classification for a single system as a function of fluid–substrate attraction $\epsilon_w/\epsilon_{\text{ff}}$ and temperature (taken from [27]).

gradually (disregarding steplike “jumps” associated with layer formation, see below) as P approaches the bulk saturation pressure $P_0(T)$. In the grand canonical ensemble employed in this thesis a similar isothermal compression is effected by increasing the

chemical potential μ up to its gas+liquid coexistence value $\mu_0(T)$. The thickness of the film increases continuously towards infinity. In class-2 systems gas pressure reaches P_0 at a finite coverage Γ . Class-3 systems show no significant increase of Γ with P , that is the substrate weakly adsorbs molecules (i.e., $\theta = \pi$). Examples for all three classes are Kr and Xe (class 1), Ar (class 2), and H₂O (class 3) at uniform, planar graphite surfaces [23].

However, Sullivan [27] pointed out that these classes of isotherms may be observable for any system but different temperatures and substrates. Figure 5.2(b) displays his original scheme to classify the wetting behavior depending on reduced fluid–substrate attractions ϵ_w/ϵ_{ff} and temperature. According to Sullivan we observe complete wetting (class 1) for all temperatures below T_c and strongly attractive substrates. For very low ϵ_w/ϵ_{ff} , on the other hand, the surface does not adsorb molecules at all so that the system exhibits class-3 behavior. Partial wetting is observed for intermediate fluid–substrate attractions. The right line between classes 1 and 2 demarcates the wetting transition (T_w in Fig. 5.2(b)). It defines the wetting temperature T_w for fixed ϵ_w/ϵ_{ff} in a way such that for $T \geq T_w$ we observe *complete* wetting, that is formation of a macroscopically thick film. For $T < T_w$, on the other hand, we find partial wetting corresponding to classes 2 or 3.

Prewetting and Layering. However, it was not until the seminal papers by Cahn [16] and later Ebner and Saam [25, 26] that wetting phenomena were perceived as a novel class of phase transitions driven by the symmetry-breaking presence of a solid surface. These authors discovered a novel surface-induced first-order phase transition between microscopically thin and thick films, that is *prewetting*. Figures 5.3(a) and (b)

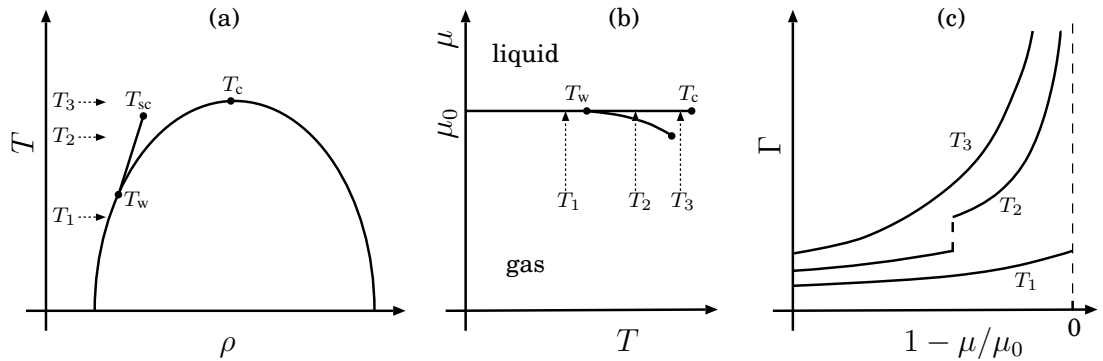


Figure 5.3: (a) and (b) schematic phase diagram of a pure fluid with a prewetting line between wetting temperature T_w and surface critical point T_{sc} . (c) Surface excess along isotherms indicated by the arrows in (a) and (b).

show the prewetting line in the phase diagram of a pure fluid. The line is a tangent to the coexistence curve starting at T_w and terminating at the surface critical (prewetting) point T_{sc} . Therefore, isotherms in Fig. 5.3(c) reveal that two isotherms T_2 and T_3 belong to class 1, whereas isotherm T_1 to class 2. Moreover, when the isotherm T_2

crosses the prewetting line in Figs. 5.3(a) and (b) the excess coverage Γ (measure of the film thickness) exhibits a discontinuous increase of finite extent indicating a first-order phase transition from microscopically thin to a microscopically thick film.

Since then it was realized that even the formation of individual layers of adsorbed molecules may constitute a discontinuous (i.e., *first-order*) phase transition. These so-called layering transitions were investigated by Pandit *et al.* [28] and Binder and Landau [30] who built on the earlier work by Dash [23] and Sullivan [27]. Pandit *et al.* [28] pointed out that there is a significant difference between prewetting and layering phase transitions. The latter consists of a discontinuous change in film thickness by just one monolayer (i.e., molecule diameter) in contrast to the prewetting transition where the film thickness increases by a *few* molecular diameters [25]. Pandit *et al.* [28] and later Bonn and Ross [127] observed prewetting for weakly and intermediately attractive long-range fluid–substrate potentials; layering transitions are to be expected for intermediate to strong short-range potentials. On account of short-range fluid–substrate interactions and the nature of our lattice fluid, our model does not allow for prewetting transitions to occur. However, in accord with the work of Bonn and Ross [127] short-range potential systems exhibit complete wetting. Also, experimental results [127] indicate that complete wetting can be characterized by mean-field models. Thus, we feel confident that our model reflects layering and complete wetting in a qualitative correct way.

Range of Fluid–Substrate Potential. Moreover, the effect of the range and the type of the fluid–substrate potential on wetting was analyzed systematically by a number of papers [29, 123, 128–133]. For example, Kroll *et al.* [128] showed that the range of the potential (short versus long) has no effect on the qualitative wetting behavior near the critical point. Ball and Evans [29] pointed out that a short-range potential may support the occurrence of layering whereas longer-range interactions lead to a continuous growth of film thickness. The relation between wetting and layering transitions was further investigated by Binder and Landau who employed Monte-Carlo simulations of Ising magnets on a simple-cubic lattice [30]. These authors also gave an account of the limitations of models with short-range interactions. In particular, they showed that layering transitions and wetting, which are of prime interest in this study, are captured in a qualitatively correct way by such models.

Additionally, the growth of fluctuations and the nature of the surface critical point was studied by Fisher and de Gennes [33], Lipowsky and Seifert [134], Sigl and Fenzl [135], Nicolaidis and Evans [136], Dietrich and Napiórkowski [31], and Bonn and Ross [127]. Dietrich and Napiórkowski [31] showed, that the (long-range) van der Waals tail of the fluid–substrate potential is not necessary for complete wetting (see below). In the excellent review of Bonn and Ross [127] the authors pointed out that for prewetting long-range fluid–substrate potentials are essential whereas both long- and short-range ones can lead to complete wetting.

Binary Mixtures. While most of the above works on wetting deal with pure fluids, binary liquid mixtures offer the opportunity to study wetting phenomena which involve

fluid phases only, that is, both coexisting bulk phases, which form the interface to be wetted, and the wetting phase itself are liquids. The intrinsic interface gives rise to the notion of *interfacial wetting* which was investigated by Sullivan [137], Tarazona *et al.* [138], Dietrich *et al.* [139, 140], Evans *et al.* [141], and Law [142]. For a review see [34].

Both in theory and experiments, the presence of solid walls complicates a precise determination of wetting characteristics because wetting phenomena depend not only on the atomic interactions between the components of the binary mixtures, but also on *two* substrate potentials acting on particles of different species. However, wetting of solid surfaces by binary *liquid* mixtures was studied by Telo da Gama and Evans [49], Dietrich and Schick [32], Fan *et al.* [43], Kierlik *et al.* [44], and Patrykiewicz *et al.* [143]. Toxvaerd [144] as well as Puri and Binder [47] investigated the surface-directed decomposition in films of binary mixtures. Some recent experimental studies were made by Plech *et al.* [38–40] and Findenegg *et al.* [62, 145]. In addition, a large portion of papers focused on mixtures *confined* by solid substrates to spaces of nanoscopic dimension(s) where wetting is subdominant to confinement-controlled phase transitions [52, 66, 78, 79, 146–149] (see also Chapter 6). Theoretically, gas adsorption and wetting of binary mixtures near gas+liquid coexistence, which is also the focal point in this thesis, were analyzed by Hadjiagapiou and Evans by means of a (continuous) mean-field density functional approach [48]. Later Schmid and Wilding used Ginzburg-Landau theory and Monte-Carlo simulations to investigate wetting of binary mixtures at gas-liquid coexistence [50]. More recently, Silbermann *et al.* employed a mean-field lattice model similar to the one on which the present study is based to investigate the wetting behavior of binary films [51].

In all three studies [48, 50, 51] intermolecular interactions are governed by short-range potentials. More specifically, Hadjiagapiou and Evans based their work on the Berthelot mixing rule for the interaction between unlike molecules of both species [48]. These authors as well as Schmid and Wilding [50] investigated wetting phenomena as a function of fluid–substrate attraction ϵ_W but for fixed interaction between unlike fluid molecules (i.e., ϵ_{AB}^*) and extended the classification scheme of Sullivan [27] partly. Silbermann *et al.* showed how the character of the wetting film (i.e., mixed *versus* demixed) changes with substrate selectivity (i.e., the energetic preference of adsorption of molecules of one species by the solid substrate) [51]. However, on account of the high dimension of the parameter space on which all models of binary mixtures are defined, most of the studies are restricted to a rather narrow range of system parameters.

In contrast, the present study aims at spanning a much wider range of model parameters. A focal point here is the competition between the tendency towards decomposition of symmetric bulk mixtures and (nonselective) gas adsorption of mixture molecules by the solid substrate. Therefore, this work extends the earlier studies in a systematic way by varying also ϵ_{AB} in addition to ϵ_W . As we shall demonstrate below the interplay between both parameters is of central importance for phase behavior and composition of wetting films. For example, as a result of this interplay we observe

wetting at *all* temperatures $T \geq 0$ for which we have coexisting phases in the bulk. Our results offer the possibility to comprehend why layering may occur for temperatures below the critical end point while complete wetting will not. However, before turning to a discussion of our results we give a brief account of phenomenological considerations and appropriate boundary conditions applying to our model to investigate and characterize wetting of a *single* solid substrate by a fluid mixture. In this context it is important to bear in mind that bulk liquid phases of the mixture remain unaffected if a single attractive solid substrate is introduced. Thus, we are concerned only with adsorption phenomena from the gaseous phase. Drying effects due to weak fluid–substrate potentials are not of interest here and will consequently be discarded.

5.1 Preamble and Model Aspects

5.1.1 Order Parameters and System Size

It is well known that wetting and layering transitions at a solid substrate depend on and are induced by the character of the substrate. Thus, one expects a variety of wetting phenomena by varying the fluid–substrate potential and the structure of the solid surface. Ball and Evans [29], de Gennes [123], Velasco and Tarazona [131], Tang and Harris [150], De Connick *et al.* [151–153], Bruin [154], Bryk *et al.* [155, 156], and Rejmer *et al.* [157, 158] analyzed the influence of surface roughness on the wetting behavior of the fluid. These authors found increased adsorption for rough walls and pronounced layer formation the smoother the walls are. More recently, Schoen *et al.* [146, 159, 159, 160] investigated the behavior of pure fluids near chemically heterogeneous and non-planar substrates. In [146] these authors showed that a non-planar wall shifts the prewetting line toward larger values of μ because a necessary prerequisite for this transition is the formation of a planar film-gas interface which is inhibited by nonplanarity of the substrate to some extent. They also observed enhanced gas adsorption for structured walls as can be seen in Fig. 4 in [146] in accordance with [131].

However, in this thesis we focus on wetting of a single *nonselective* planar, homogenous substrate by a gaseous symmetric binary bulk mixture so that

$$\epsilon_{\text{BB}}^* = 1, \quad \Delta\mu = 0. \quad (5.2)$$

Symmetric binary bulk mixtures are analyzed thoroughly in Sec. 4.2.5. We locate the substrate perpendicular to the z -axis at $z = 0$ and employ the short-range symmetric fluid–substrate potential of Eq. (2.25). Now, the attractive substrate is characterized by only a *single* parameter, that is $\epsilon_{\text{W}}^+ = \epsilon_{\text{W}}/\epsilon_{\text{ff}}$ (see Sec. 4.1.3). For purely practical reasons appropriate boundary conditions (i.e., two substrates at $z = 0$ and $z = n_z + 1$) are incorporated (see Sec. 2.2 and Eqs. (2.6) and (2.24)) such that our system is symmetric with respect to a plane located at $c \equiv n_z/2$. For small n_z the presence of a second

substrate may cause unwanted confinement effects such as capillary condensation (i.e., the shift of the gas+liquid coexistence). To make sure that wetting prevails as the dominating feature we use a large system size $n_z \geq 40$ for films which have up to five adsorbed monolayers. For larger film thicknesses we increase n_z up to 100. The range of distances from the solid substrates over which the local density ρ_k deviates from its bulk value does not exceed the value of 20ℓ except above the wetting temperature and very close to bulk coexistence. In other words, we are *effectively* dealing with wetting phenomena occurring at a *single* solid substrate when considering only one half of our model system.

Because the overall (mean) order parameters of the bulk system ρ and m cannot account for film phases we introduce *integral* order parameters which measure the amount of adsorbed particles of both species. For a fixed thermodynamic state (i.e., T and μ for symmetric mixtures) the excess coverage is expressed by

$$\Gamma = \frac{1}{c} \sum_{k=1}^c (\rho_k - \rho_{\text{bulk}}) \quad (5.3)$$

where ρ_{bulk} is the gas density of the bulk system. Thus, Γ measures the overall number of adsorbed particles. In the same spirit we introduce a density-corrected, dimensionless miscibility parameter

$$M \equiv \frac{1}{\Gamma} \int_0^\infty \rho^A(z) - \rho^B(z) dz = \frac{1}{c\Gamma} \sum_{k=1}^c m_k (\rho_k - \rho_{\text{bulk}}) \quad (5.4)$$

as a meaningful quantitative measure of the “degree” of miscibility in binary-mixture films. For example, for a pure A-film (i.e., $m_k = 1$) $M = 1$. We note that in our present symmetric model the bulk gas phase is always perfectly mixed, that is $m = 0$.

5.1.2 Scaling Considerations

From the discussion given in the preceding sections one expects the fluid–substrate attraction to become particularly important for the classification of a particular system. To see the latter let us briefly elaborate on a simple phenomenological argument.

Low Temperatures. Consider a sessile droplet of liquid on a solid substrate as sketched in Fig. 5.1(a). Its contact angle θ is determined by the Young-Dupré equation [161]

$$\cos \theta = \frac{\sigma_{\text{gs}} - \sigma_{\text{ls}}}{\sigma_{\text{gl}}} \quad (5.5)$$

where $\sigma_{..}$ is the interfacial tension between gas (g), liquid (l), and solid (s) phases. To obtain a rough estimate for the set $\{\sigma_{..}\}$ simple heuristic energetic arguments may be invoked. Consider the following *Gedankenexperiment* by which we introduce an auxiliary plane in a hypothetical, infinitely large body of liquid without interfaces. We

then remove that portion of liquid above the plane. This creates a liquid-gas interface by breaking “bonds” (i.e., cutting off interactions) between molecules across the newly formed interface. As a result the free energy of the now semi-infinite remainder of liquid will increase by an amount

$$\sigma_{gl} \simeq \frac{1}{2} \rho_{liq}^2 |\epsilon_{ff}| \quad (5.6)$$

for sufficiently low temperatures where one may safely assume entropic contributions to be negligible. In Eq. (5.6), ρ_{liq} is the density in the semi-infinite liquid slab and ϵ_{ff} is a measure of the strength of attraction between a pair of liquid molecules. Note that no distinction is made between pure fluids and (multicomponent) mixtures. To create a solid-liquid interface we proceed as before, that is we introduce a second auxiliary plane in the liquid, remove the portion of liquid *below* that plane but this time replace it by solid which, in turn, lowers the (free) energy by approximately $\rho_{liq} |\epsilon_w|$. Thus,

$$\sigma_{ls} \simeq \frac{1}{2} \rho_{liq}^2 |\epsilon_{ff}| - \rho_{liq} |\epsilon_w| \quad (5.7)$$

For sufficiently low temperatures it seems fair to assume that the density of the gas phase essentially vanishes. Hence,

$$\sigma_{gs} \simeq 0. \quad (5.8)$$

With the aid of Eqs. (5.6) – (5.8) one obtains from Eq. (5.5)

$$\cos \theta \simeq \frac{2}{\rho_{liq}} \frac{\epsilon_w}{\epsilon_{ff}} - 1 \quad (5.9)$$

Hence, from (5.9) we expect complete wetting (i.e., $\cos \theta = 1$) to occur if

$$\frac{\epsilon_w}{\epsilon_{ff}} \geq \rho_{liq}, \quad (5.10)$$

that is, complete wetting depends crucially on the relative strengths of fluid–fluid and fluid–substrate attraction. We return to this low temperature criterion later. So far we discard the entropic contributions altogether. However, Cahn [16] gave a lucid argument for the occurrence of complete wetting even near the bulk critical point (i.e., at high temperatures) where entropic contributions are vital.

Scaling Laws Near the Critical Temperature (Cahn’s Argument). Following Cahn [16] we express the growth of the contact angle near the bulk gas+liquid critical temperature T_c by

$$\cos \theta \propto (T_c - T)^{\beta - 2\nu}, \quad (5.11)$$

where β and ν are critical exponents associated with the density difference between coexisting liquids and gases and the range of intermolecular correlations, respectively. Since $\beta - 2\nu < 0$ for two- and three-dimensional systems [162] a wetting temperature

$T_w < T_c$ must exist where $\theta = 0$ such that we have complete wetting for all $T \geq T_w$. The study of Sullivan [27] also shows that for temperatures near the critical point (just below T_c in Fig. 5.2(b)) the region of class-1 systems widens towards weaker fluid–substrate potentials so that even partial wetting (class 2) is hard to observe. We note in passing that while Cahn’s argument is correct for short-range fluid–substrate potentials [125], it may be wrong for long-range potentials as pointed out by Nightingale and Indekeu [129] and corroborated later by Ebner and Saam [130]. Thus, in our case we always obtain complete wetting for intermediate to weak substrates at least close to the critical point, as long as the adsorbed films remain mixed.

Scaling Laws Near the Critical End Point Temperature. Consider now a symmetric binary mixture of type I where, for example, $\epsilon_{AB}^* = 0.7$. A typical bulk phase diagram is presented in Fig. 5.4. It reveals that for temperatures above those of the

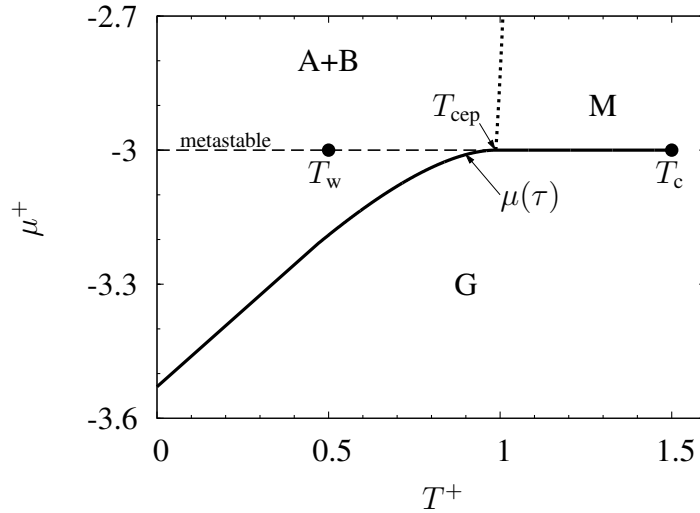


Figure 5.4: Bulk phase diagram for $\epsilon_{AB}^* = 0.7$ where the metastable gas+mixed liquid coexistence line (dashed) is also indicated. Solid lines refer to first-order phase transitions of three (G+A+B) or two (G+M) phases (abbreviation code, see Table 4.1). The λ -line is dotted. The critical end point lies at $T_{cep}^+ = 1.0$ and $\mu_{cep}^+ = -3$.

λ -line, the bulk phase diagram is indistinguishable from that of a pure fluid but for the *effective* strength ϵ_{ff} of fluid–fluid attraction (see Sec. 4.1.3). From Fig. 5.2(b) it follows that the mixture has a *hypothetical* wetting temperature T_w which, for a suitable fluid–substrate attraction, equals that of a corresponding pure fluid (in units of ϵ_{ff}) as shown in Fig. 5.4. For a moderate fluid–substrate attraction we have $0 < T_w < T_{cep}$. Thus, the wetting temperature is hypothetical because for $T < T_{cep}$ mixed bulk liquids are metastable with respect to demixed ones (see dashed horizontal line in Fig. 5.4).

Consider now the growth of wetting films along (or infinitesimally below) the G+A+B triple line $\mu(\tau)$ as $\tau \equiv T_{cep} - T \rightarrow 0^+$ in Fig. 5.4. In the vicinity of the critical

end point useful scaling laws were derived for the growth of wetting films [124, 125]. The thickness l of an adsorbed film diverges logarithmically because $T > T_w$, that is

$$l(\mu, \tau) \propto -\ln(\mu(\tau) - \mu_{\text{cep}}). \quad (5.12)$$

On the other hand, in the immediate vicinity of the critical end point one also has [9, 10, 13, 118, 119]

$$\mu(\tau) - \mu_{\text{cep}} \propto \tau^{2-\alpha} \quad (5.13)$$

where α is the relevant critical exponent of the near critical A+B coexistence. Therefore, Eq. (5.12) leads to

$$l(\tau) \propto -\ln \tau. \quad (5.14)$$

Hence, the thickness of the adsorbed film remains finite for all $T < T_{\text{cep}}$ and diverges comparably weakly as $\tau \rightarrow 0^+$. Moreover, the length of composition fluctuations ξ_{comp} between the A- and B-rich liquids diverge much faster as $T \rightarrow T_{\text{cep}}$ [162], namely²

$$\xi_{\text{comp}} \propto \tau^{-\nu}. \quad (5.15)$$

Therefore, a range of temperatures $T' < T \leq T_{\text{cep}}$ exists such that $\xi_{\text{comp}} > l$ along the triple line $\mu(\tau)$ so that the two coexisting demixed film phases are no longer distinguishable. This implies that along $\mu(\tau)$ adsorbed films always become mixed *prior* to the bulk critical end point in accord with the assertions by Ball and Evans (see Fig. 2 in [29]).

Predictions. To summarize we expect complete wetting just below T_c even for weakly adsorbing substrates (Eq. (5.11)). The wetting temperature at and above which complete wetting occurs depends strongly on ϵ_w . Therefore, for large ϵ_w the wetting temperature goes down to zero (see Eq. (5.10) and Fig. 5.2(b)). For $T > T_{\text{cep}}$ all films are mixed regardless of their thickness, that is $M = 0$ (Eqs. (5.14) and (5.15)). Below T_{cep} the thickness of *mixed* films remains finite (Eq. (5.14)). Thus, complete wetting occurs only for *demixed* films.

5.2 Pure Fluids

5.2.1 Layering Transitions and Excess Coverage

It is again instructive to begin the discussion with pure fluids realized for $\epsilon_{\text{AB}}^* = 1$. Consider first a relatively weak fluid–substrate attraction of $\epsilon_{\text{W}}^+ = 0.82$. The corresponding plot in Fig. 5.5(a) shows the gas+liquid coexistence line $\mu_0^+ = -3$ ending at the critical point where $T_c^+ = 1.5$. Moreover, films of more than four layers appear to be thermodynamically stable. The coexistence lines (n) between films of $n - 1$ and

²Note that the A- and B-rich liquid coexistence becomes critical whereas the gas+liquid coexistence remains unaffected, that is of first-order.

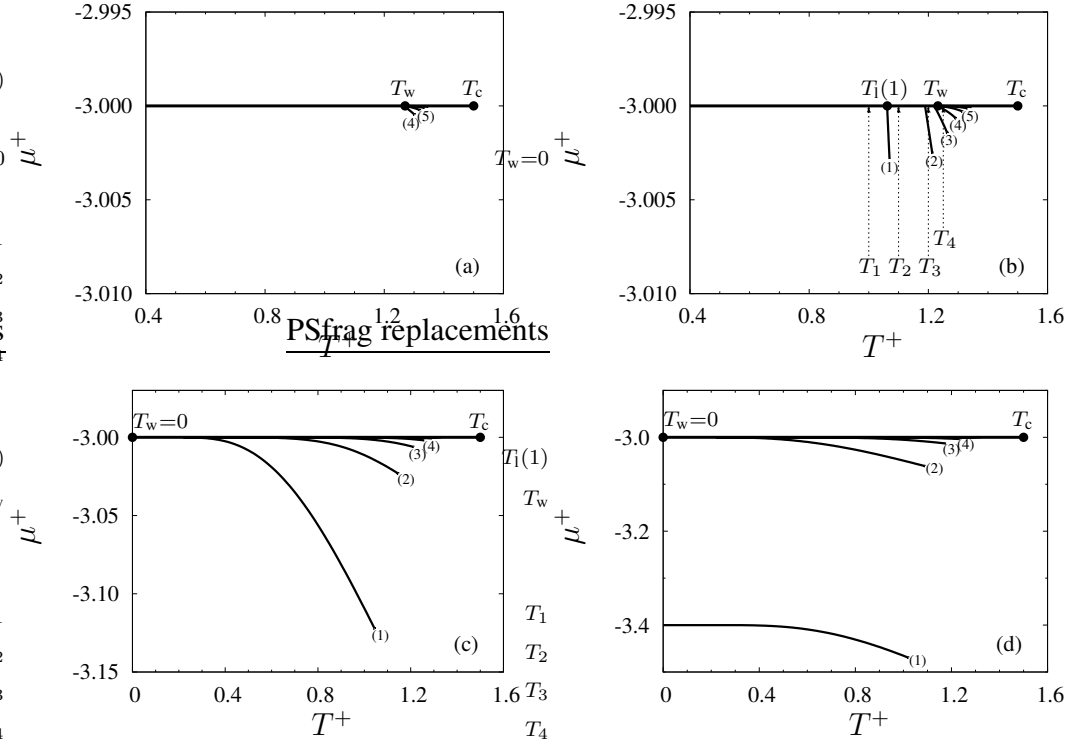


Figure 5.5: Phase diagrams for the pure fluid (i.e., $\epsilon_{AB}^* = 1$). The numbers (n) indicate first-order coexistence lines between films of $n - 1$ and n layers ($n - 1 = 0$ refers to the gas). (a) $\epsilon_W^+ = 0.82$; (b) $\epsilon_W^+ = 0.84$, excess coverage is plotted in Fig. 5.6 for vertical isotherms; (c) $\epsilon_W^+ = 1.0$, T_w approaches zero; (d) $\epsilon_W^+ = 1.4$.

n layers start at the layering temperature $T_1(n)$ and end at a layering critical temperature $T_{lc}(n)$ both of which depend on n . According to Binder and Landau the wetting temperature at which an adsorbed film becomes macroscopically thick may then be defined by [30]

$$T_w \equiv \lim_{n \rightarrow \infty} T_1(n). \quad (5.16)$$

Following the same authors [30] we define the roughening temperature by

$$T_r \equiv \lim_{n \rightarrow \infty} T_{lc}(n). \quad (5.17)$$

As one approaches T_r , fluctuations of film thickness grow enormously such that the film-gas interface becomes “rough” in the sense that individual layers parallel with the solid surface can no longer be discerned. In our model $T_r = T_c$ and hence $T_w < T_c$ so that we indeed observe layering transitions and complete wetting according to assertions by Binder and Landau (see middle plot in Fig. 2 in [30]). These authors pointed out that prewetting (i.e., coexistence between molecularly thin and thick films) can be observed only if $T_r < T_w$ which does not hold for our model. Thus, we cannot ob-

serve prewetting. Nevertheless, our model mimics correctly both partial and complete wetting scenarios as well as layering transitions.

Returning to the case $\epsilon_w^* = 0.82$ we see from Fig. 5.5(a) that the $T_1(n)$ are almost independent of n , so that the limit (5.16) is expected to exist, that is all coexistence lines start at nearly the same temperature of about $T_w^+ = 1.23$ and are fairly short. This picture changes if ϵ_w increases slightly as Fig. 5.5(b) reveals. Additional coexistence lines for mono-, bi-, and trilayer phases arise. One also notices that the shift between neighboring layering temperatures $T_1(n+1) - T_1(n)$ rapidly diminishes with increasing n so that again the limit in Eq. (5.16) should exist. This is illustrated by plots in Fig 5.6

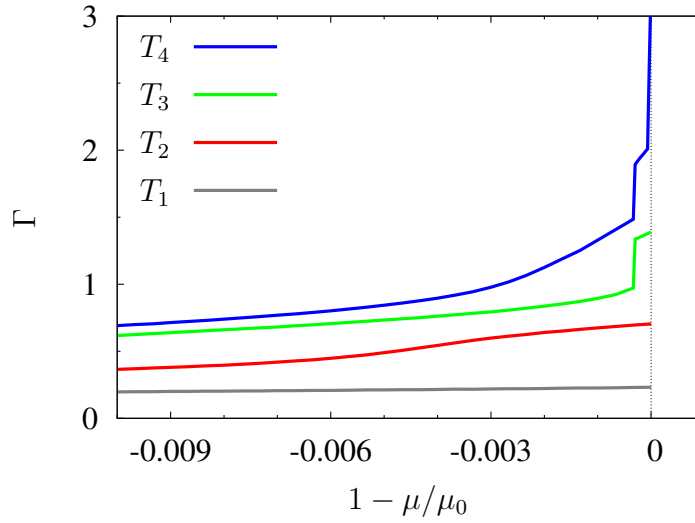


Figure 5.6: Excess coverage Γ along isotherms identified in Fig. 5.5(b) when approaching the gas+liquid coexistence at μ_0 from the gas side.

where the excess coverage Γ (see Eq. (5.3)) is presented as a function of chemical potential for four isotherms identified in Fig. 5.5(b). *Complete* wetting is observed along isotherm $T_4^+ = 1.25$ slightly exceeding the wetting temperature $T_w^+ = 1.23$.

On the other hand, the excess coverage remains finite below T_w (see isotherms T_1 - T_3 in Figs. 5.5(b) and 5.6) thus comporting to *partial* wetting. The isotherm T_1 in Fig. 5.5(b) lies below $T_1(1)$, thus we observe a sub-monolayer coverage of the substrate in accord with the corresponding Γ in Fig. 5.6 which remains below 1. Similarly, Γ along isotherm T_2 depends only weakly on μ but its final value is closer to 1, indicating that a monolayer forms on the substrate. Since the isotherm T_2 in Fig. 5.5(b) is supercritical with respect to the coexistence line (1), $\Gamma(\mu)$ is continuous. However, the isotherm T_3 crosses the layering coexistence line (2) in Fig. 5.5(b). Consequently, the corresponding Γ in Fig. 5.6 changes discontinuously but remains finite up to the bulk gas+liquid coexistence at a value which corresponds to an imperfect bilayer. Finally, isotherm T_4 is supercritical with respect to (1) and (2) but intersects all lines (n) for $n \geq 3$ (see

Fig. 5.5(b)). This is reflected by the Γ -plot in Fig. 5.6. Similar effects have also been observed in pure fluids as one can see in Fig. 4 of [163], in Fig. 13(b) of [28], and in Fig. 1(b) [29] for moderately adsorbing substrates.

If ϵ_w increases further the wetting temperature T_w goes to zero, as the plot for $\epsilon_w^+ = 1.0$ in Fig. 5.5(c) shows. All layering coexistence lines now start at $T_w = 0$, and one-phase regions of films between them widen considerably. Further increase of ϵ_w causes the coexistence line between monolayer and gas to become detached from the bulk coexistence line. For example, for $\epsilon_w^+ = 1.4$ the chemical potential of coexistence at $T = 0$ is reduced to $\mu_1^+(1) = -3.4$, whereas $\mu_1^+(n) = -3.0$ for $n \geq 2$ regardless of their magnitude ϵ_w . This effect is caused by the short-range character of the fluid–substrate potential and comports with the conjecture of Pandit *et al.* (see Fig. 18(a) in [28]) for strongly adsorbing substrates.

5.2.2 Wetting Temperature

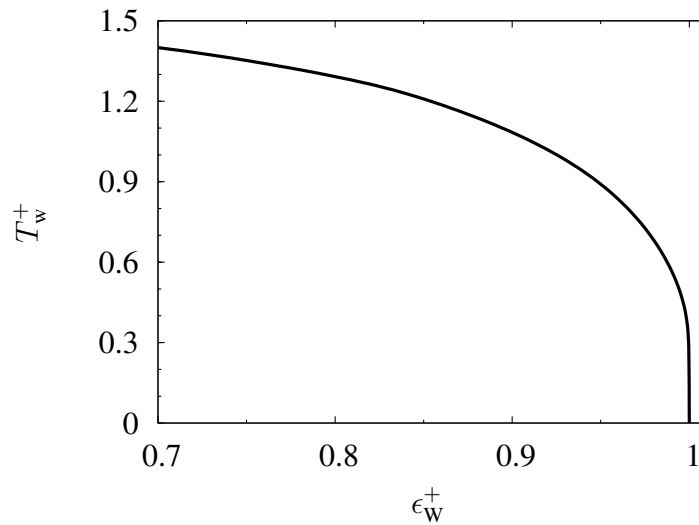


Figure 5.7: Wetting temperature as a function of the strength of the fluid–substrate attraction, ϵ_w^+ .

Finally, we briefly return to the strong dependence of the wetting temperature T_w on the strength of the fluid–substrate attraction ϵ_w . From Eq. (5.16) we can calculate T_w as a function of ϵ_w which is shown in Fig. 5.7. In accord with Fig. 5.5(c), T_w vanishes as ϵ_w^+ assumes the value of 1. Moreover, for $\epsilon_w^+ = 1.0$, $T_w = 0$ is also predicted by the phenomenological Eq. (5.10). The vanishing of T_w in the limit of sufficiently attractive substrates was reported by Sullivan (see Fig. 5.2(b)) and by Binder and Landau (see the uppermost plot in Fig. 2 of [30]).

On the other hand, Cahn's argument (see Sec. 5.1.2) already predicts $0 < T_w < T_c$ for weaker substrates. Figure 5.7 reveals that this is indeed the case. It turns out that the weaker the fluid–substrate potential the larger is the wetting temperature which tends to reach the critical temperature of $T_c^+ = 1.5$ in the limit $\epsilon_w^+ \rightarrow 0$ in accord with [30]. However, because of the numerical limitation for finding the limit of Eq. (5.16) near the critical point we are not able to reach this limiting value. It is noteworthy that the curve in Fig. 5.7 agrees qualitatively with the T_w -line in Fig. 5.2(b) of Sullivan [27].

So far our results merely verify what is already known about wetting of chemically homogenous, planar solid surfaces by *pure* fluids. However, the excellent agreement with the existing literature encourages us to extend this work to wetting by *binary* mixtures.

5.3 Wetting Behavior of Symmetric Mixtures

To study the wetting by symmetric binary mixtures as a function of both, ϵ_{AB} and ϵ_w , we divide the present section into three separate parts. Similar to the investigation of bulk systems in Chapter 4, the three generic types of binary symmetric mixtures are represented by $\epsilon_{AB}^* = 0.7, 0.5, \text{ and } 0.3$, respectively. In the following, wetting from the gas phase is observed for thermodynamic states *below* the gas+demixed or for higher temperatures *below* the gas+mixed liquid coexistence line (see Fig. 5.4). The two lines separating gas and liquid form the bulk “condensation” line represented by μ_0 where we omit the temperature-dependence for the sake of simplicity of our notation.

5.3.1 Type-I Mixtures

Phase Diagram. We begin with a mixture of type I for which $\epsilon_{AB}^* = 0.7$ as before, and plot the phase diagram in the T - μ projection for a weak substrate attraction, $\epsilon_w^+ = 0.84$ in Fig. 5.8(a). For this system, $T_w > T_{cep}$ and the layering coexistence lines for one to three layers are fairly short. Isotherms $T_1, T_2, \text{ and } T_3$ are identified for which the surface excess Γ is plotted in Fig. 5.9(a). As before in Fig. 5.6 we observe only sub-monolayer coverage along T_1 when gas+liquid coexistence is approached at μ_0 . This is because we are below $T_1(1)$. Path T_2 in Fig. 5.8(a), on the other hand, is supercritical with respect to $T_{lc}(1)$. Thus, the corresponding plot of Γ in Fig. 5.9(a) grows continuously to a value close to 1 but remains finite because $T_2 < T_w$. These two isotherms refer to partial wetting.

This situation changes along path T_3 in Fig. 5.8(a), where $T_3 > T_w$ and hence, Γ diverges when μ approaches μ_0 (see Fig. 5.9(a)). Since layering coexistence lines accommodating four or more layers coincide approximately³ with the bulk coexistence

³because of the short-range character of the fluid–substrate potential

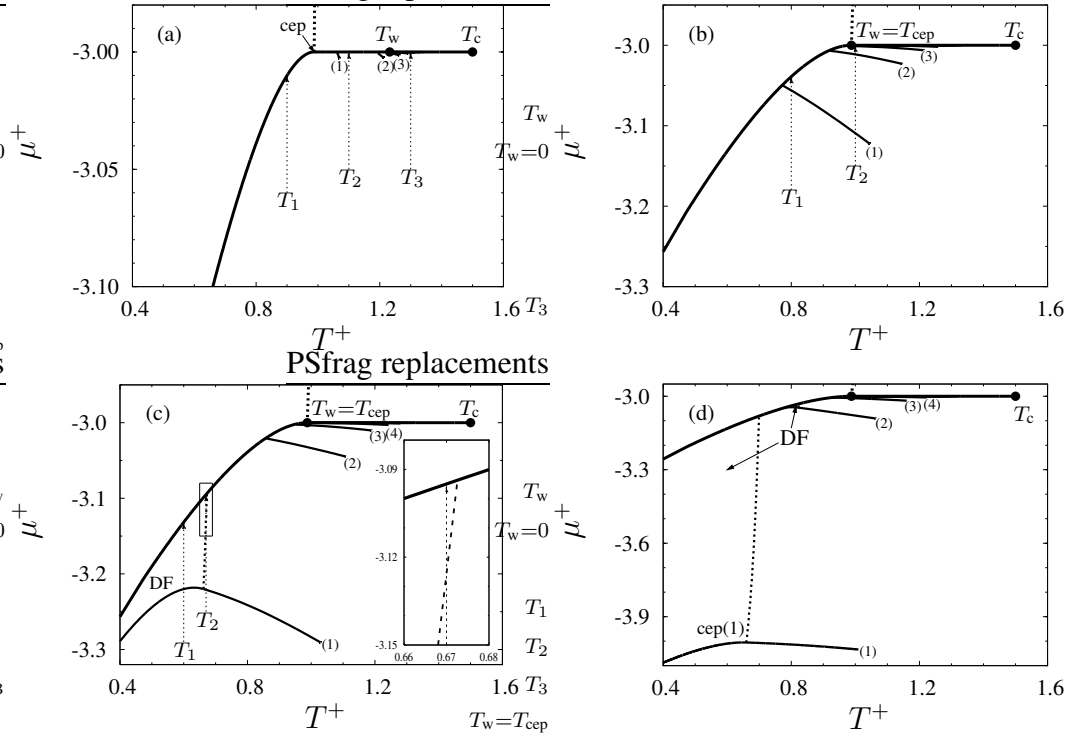


Figure 5.8: As Fig. 5.5 but for $\epsilon_{AB}^* = 0.7$. (a) $\epsilon_W^+ = 0.84$; (b) $\epsilon_W^+ = 1.0$; (c) $\epsilon_W^+ = 1.2$, where a surface λ -line (dotted) appears. Bounded rectangle is enlarged in the inset; (d) $\epsilon_W^+ = 2.0$. Note the different μ -scales in (a)–(d).

line at $\mu_0^+ = -3.0$ for $T \geq T_w$ (see Fig. 5.8(a)), this divergence is caused by a smooth formation of a macroscopically thick film, that is complete wetting.

We turn to a more attractive substrate next (i.e., $\epsilon_W^+ = 1.0$ in Fig. 5.8(b)) where $T_w = T_{cep}$ as predicted by the scaling arguments laid out in Sec. 5.1.2. The coexistence lines of films with one to four layers are now significantly longer. We consider two isotherms T_1 and T_2 below and above T_w in Fig. 5.8(b), respectively. The corresponding excess coverage Γ is plotted in Fig. 5.9(b). Since $T_1 < T_w$ we observe partial wetting for this isotherm but also a discontinuity in Γ when crossing the coexistence line (1) at $1 - \mu/\mu_0 \simeq -0.006$. As path T_2 in Fig. 5.8(b) intersects two layering coexistence lines there are two jumps in the plot of Γ in Fig. 5.9(b) before it diverges because $T_2 > T_w$. All these films are mixed (i.e., $M = 0$ right ordinate) as dashed lines in Fig. 5.9(b) show. We note that according to the scaling law of Sec. 5.1.2 we do not observe demixed films for $T > T_{cep}$.

As one increases ϵ_W further (Fig. 5.8(c) and (d)) for low μ and low T monolayer films may form either demixed (DF) or mixed films. Mixed and demixed films are separated by a surface λ -line starting at a surface critical end point cep(1). A demixed film refers to coexisting A- and B-rich films which becomes critical at the surface λ -

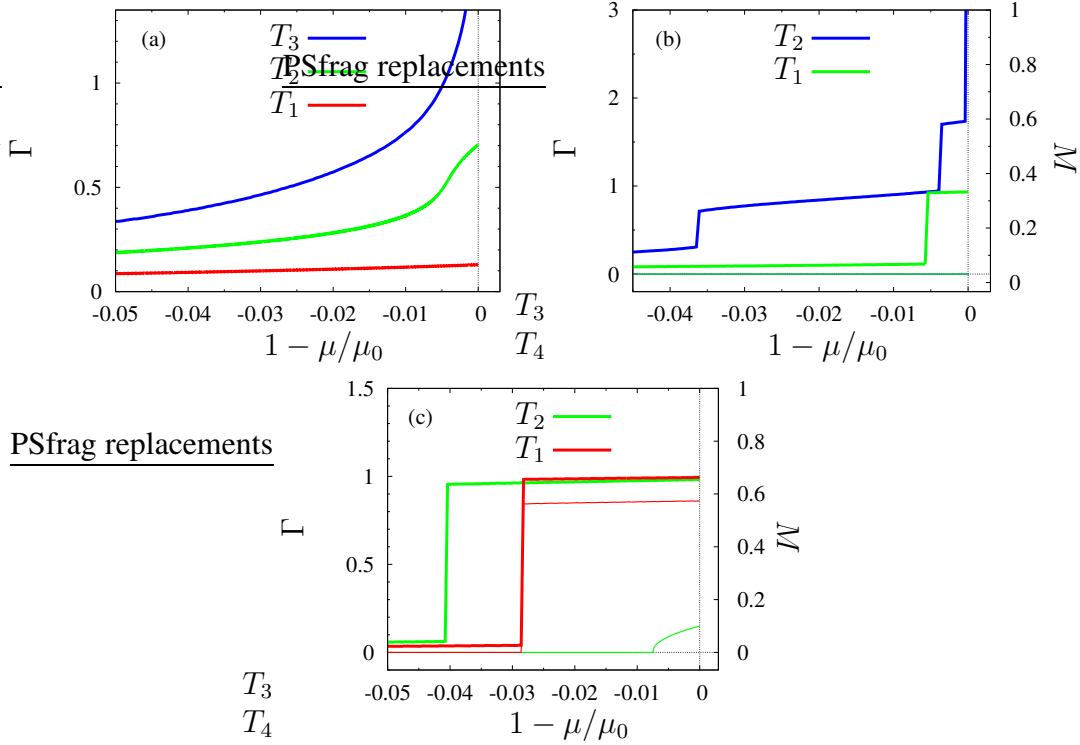


Figure 5.9: Excess coverage Γ (thick lines, left ordinate) and miscibility M (thin lines, right ordinate) along the isotherms identified in Figs. 5.8(a)–(c) as a function of $1 - \mu/\mu_0$, where μ_0 is the chemical potential at bulk condensation.

line. Therefore, when plotting the miscibility M of a demixed film we only show the A-rich film and omit the B-rich one, because for both the magnitude of Γ is the same as well as the *absolute* values of M . Along the isothermal path T_1 indicated in Fig. 5.8(c) the parallel plot of Γ and M in Fig. 5.9(c) shows a layering transition between gas and demixed ($M \rightarrow 0.54$) monolayer phases at $1 - \mu/\mu_0 \simeq -0.029$. Moreover, along the isotherm $T_2 > T_1$ we first observe a first-order layering transition from gas to mixed monolayer at $1 - \mu/\mu_0 \simeq -0.041$ which is reflected by the discontinuity in Γ whereas M remains zero (see Fig. 5.9(c)). As one continues along T_2 towards bulk gas+liquid coexistence one eventually crosses the surface λ -line (see inset of Fig. 5.8(c)). Now, the order parameter Γ remains nearly constant whereas M changes continuously to positive values as Fig. 5.9(c) reveals. Thus, this phase transition is of second-order according to our expectation when crossing the λ -line. This is further illustrated by the vertical tangent at M at $1 - \mu/\mu_0 = -0.008$ in Fig. 5.9(c)⁴.

However, Γ remains finite for the two isotherms, that is we are below the wetting temperature at $T_w = T_{cep}$. If ϵ_w reaches sufficiently large values this scenario does not change much except thicker layers start to demix, too. For example, for $\epsilon_w^+ = 2.0$ in

⁴Note, that we omit the B-rich film phase.

Fig. 5.8(d) both demixed and mixed bilayer films appear.

Complete Wetting. Before turning to type-II mixtures we return to our earlier observation that T_w cannot be lower T_{cep} regardless of the values of ϵ_w (at least for moderate values). For this purpose a plot of a typical type-I mixture for $\epsilon_w^+ = 1.18$ is

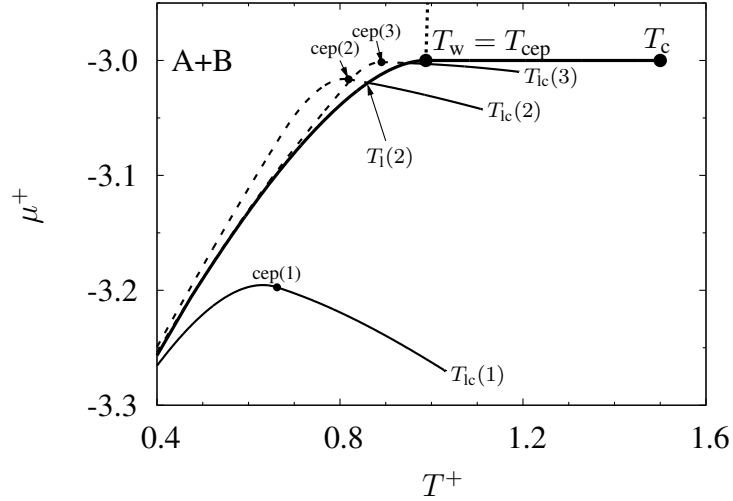


Figure 5.10: As Fig. 5.5 but for $\epsilon_w^+ = 1.18$. Also shown are metastable layering coexistence lines (dashed). Surface λ -lines starting at surface critical end point $cep(n)$ are omitted for the sake of clarity.

shown in Fig. 5.10 where now the metastable portions of film-phase coexistence lines are also apparent as dashed lines. For low temperatures all films are demixed. As T increases along the layer coexistence lines (1), (2), and (3) each one of them exhibits a surface critical end point $cep(n)$, where a corresponding surface λ -line starts (which in Fig. 5.10 are omitted for the sake of clarity). However, for $T > T_{cep}(n)$, a film of n layers turns out to be mixed because entropic contributions dominate energetic ones. This is apparently the easier the lower n is. Thus, $\lim_{n \rightarrow \infty} T_{cep}(n) = T_{cep}$ exists (see Fig. 5.10) but with $T_{cep}(n) \leq T_{cep}$. Consequently, we do not observe *demixed* films for temperatures above the bulk critical end point T_{cep} contrary to the qualitative discussion of Schmid and Wilding (see Fig. 16 in [50]) but in accord with the scaling argument of Eqs. (5.14) and (5.15). However, this figure also reveals that the surface critical end points $cep(n)$ for $n \geq 2$ are metastable and only mixed films are thermodynamically stable. Thus, one has layering temperatures $T_l(n)$, but only for finite n as long as $T < T_{cep}$. Consequently, there is no complete wetting (of mixed films) below the bulk critical end point, in accord with the scaling arguments in Sec. 5.1.2.

However, complete wetting by *demixed* films may be found for sufficiently strong substrates. Then the metastable (dashed) demixed layering coexistences (see Fig. 5.10) are more bending to the right so that they lie within the bulk gas region and thus

become stable.

5.3.2 Type-II Mixtures

Phase Diagram. If we lower ϵ_{AB} the type of the bulk mixture changes from I to II (see Chapter 4). The critical end point vanishes and instead, the quadruple point appears at which the mixed and the two demixed liquid phases coexists with gas. For a fluid–substrate attraction of $\epsilon_W^+ = 1.3$ the phase diagram is displayed in Fig. 5.11(a). In the present case the wetting temperature coincides with the quadruple point as T_w

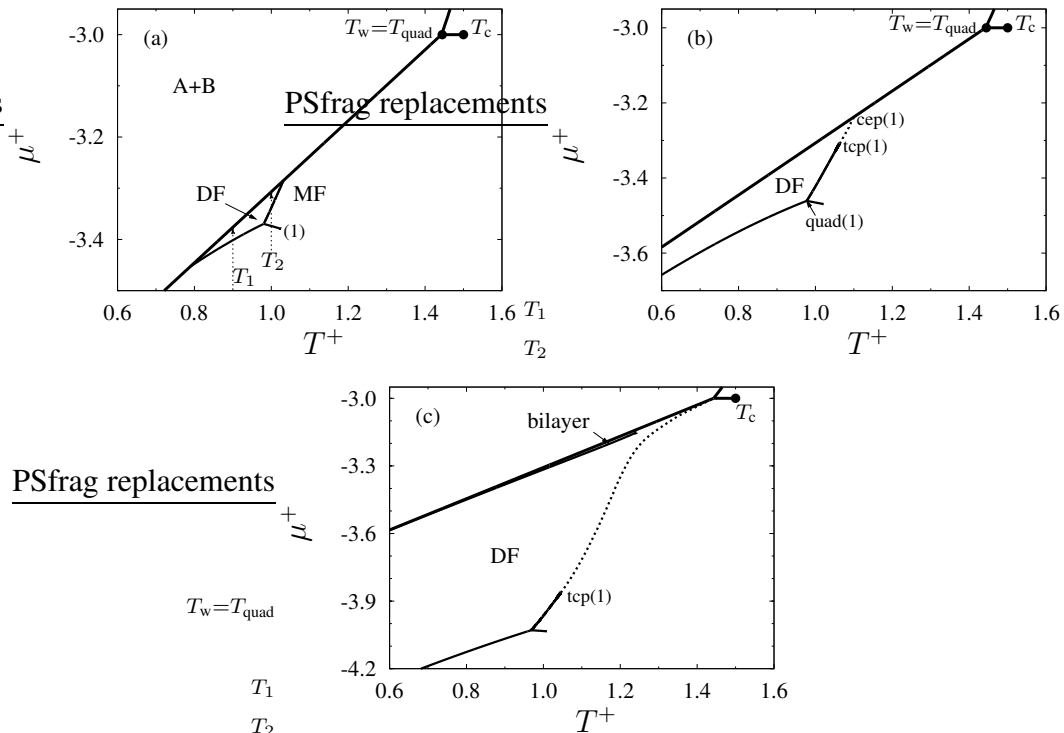


Figure 5.11: As Fig. 5.5 but for $\epsilon_{AB}^* = 0.5$. (a) $\epsilon_W^+ = 1.3$; (b) $\epsilon_W^+ = 1.4$; (c) $\epsilon_W^+ = 2.0$.

did with T_{cep} in the previously discussed case of a type-I mixture (see Fig. 5.10). Plots in Fig. 5.11(a) also show the triangular-shaped one-phase region of the demixed monolayer (DF). The latter is enclosed by various first-order coexistence lines which can be identified if we consider two isotherms T_1 and T_2 . Along T_1 we cross the gas+demixed monolayer triple⁵ line before eventually reaching the bulk condensation line where demixed monolayer and demixed liquid coexist. This is visible in the parallel plot of Γ and M in Fig. 5.12 (isotherm T_1) where both, Γ and M , exhibit a discontinuity at $1 - \mu/\mu_0 \simeq -0.008$, indicating that a demixed layer forms. Along

⁵Note, that the demixed monolayer represents a coexistence of A- and B-rich monolayers.

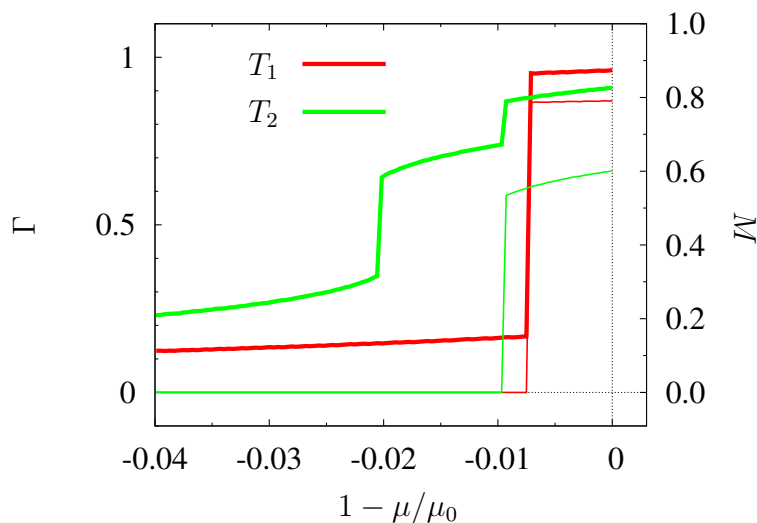


Figure 5.12: As Fig. 5.9 but for two isotherms specified in Fig. 5.11(a).

isotherm T_2 (see Fig. 5.11(a)) two coexistence lines are crossed. At the first intersection at $1 - \mu/\mu_0 \simeq -0.021$ (see Fig. 5.12), Γ changes discontinuously to about $\Gamma \simeq 0.64$ but M remains zero. Thus, a mixed monolayer film (MF) appears. As μ increases further, Γ keeps rising until a second discontinuity at $1 - \mu/\mu_0 \simeq -0.01$ is observed, at which $\Gamma \simeq 0.87$. Hence, the initial monolayer film becomes slightly denser. Moreover, at the second discontinuity M rises to a value of about 0.53, and therefore the initially mixed monolayer appears to be demixed. Schmid and Wilding [50] also reported a discontinuous change in film thickness accompanied by a change in composition (see Fig. 14 in their work). However, here the observed jump in film thickness involves only mono- and bilayer films (see also Fig. 5.8(d)) on account of the short-range attraction employed in this study. Since Γ remains finite along T_1 and T_2 all the way to $1 - \mu/\mu_0 \rightarrow 0^-$, we again deal with cases of partial wetting. In addition, the demixed and mixed films coexist with the gas phase at the surface quadruple point at $T_{\text{quad}}(1) = 0.98$ slightly below T_2 in Fig. 5.11(a).

As ϵ_W^+ increases to 1.4 the one-phase region of the demixed monolayer (DF) widens considerably, as Fig. 5.11(b) shows. In this case transitions from demixed to mixed films are either of first- or second-order, because a surface tricritical point $\text{tcp}(1)$ appears at which a surface λ -line (dotted line) starts. This line terminates at a surface critical end point $\text{cep}(1)$ when approaching the bulk condensation line. The widening of the region for larger ϵ_W , where the demixed film is stable, was reported by Schmid and Wilding (see Fig. 5 in [50]). They also showed that this effect is more pronounced the smaller the value of ϵ_{AB} is (see Fig. 7 in [50]) in accord with our results (see Figs. 5.8(d) and 5.11(c)). In addition, the monotonic temperature-dependence of the surface λ -line agrees with the findings of these authors (see Fig. 8 in [50]).

Further increase of ϵ_W causes the gas+monolayer coexistence lines to become even

more detached from the bulk phase diagram, as the graph for $\epsilon_W^+ = 2.0$ in Fig. 5.11(c) shows. Since the surface λ -line becomes longer compared with its counterpart in Fig. 5.11(b), the region of demixed film phases (DF) is enlarged so that a novel (demixed) bilayer film arises in Fig. 5.11(c). Unlike bilayer films for $\epsilon_{AB}^* = 0.7$ in Figs. 5.8 and 5.10, coexistences involving *mixed* bilayer are not observed. Thus, the surface critical point $T_{lc}(2)$ is buried inside the demixed region.

Comparing Figs. 5.11(b) and (c) it should also be noted that the surface tricritical temperature (tcp(1)) decreases slightly from 1.051 to 1.049 if ϵ_W^+ increases from 1.4 to 2.0. Hence, the order of layering transitions at $T^+ = 1.05$ changes from first- to second-order. Schmid and Wilding [50] observed a weakening of the first-order mixed+demixed film transition for larger ϵ_W which may indicate that the corresponding (tri)critical point also decreases.

5.3.3 Type-III Mixtures

Phase Diagram. A typical type-III mixture is obtained for $\epsilon_{AB}^* = 0.3$. Its wetting behavior for a fluid–substrate attraction $\epsilon_W^+ = 1.6$ is illustrated by Fig. 5.13(a). The

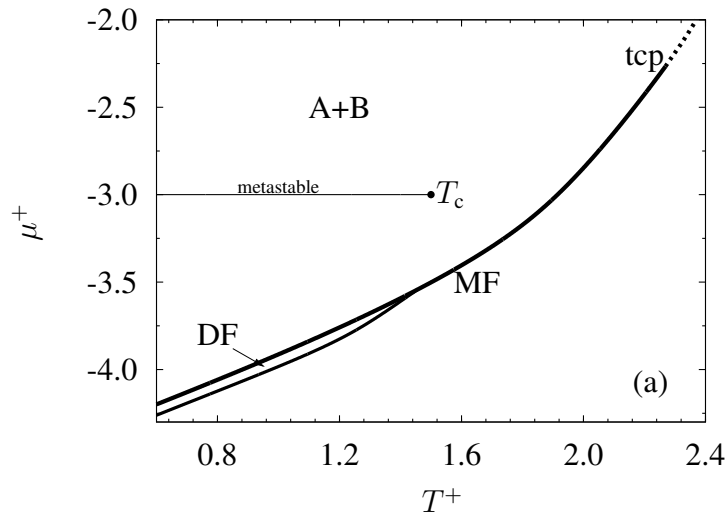


Figure 5.13: Ctnnd.

now metastable gas+mixed liquid bulk coexistence line is buried inside the region of the demixed bulk liquid (A+B) and is thus only metastable (see also Sec. 4.2.5). Also, the bulk tricritical point (tcp) is visible where gas and both demixed liquids become critical simultaneously. In addition, even though the substrate is strongly attractive all film phases turn out to be metastable, thus being entirely inaccessible from an equilibrium perspective. One exception are the adsorbed demixed (DF) and mixed

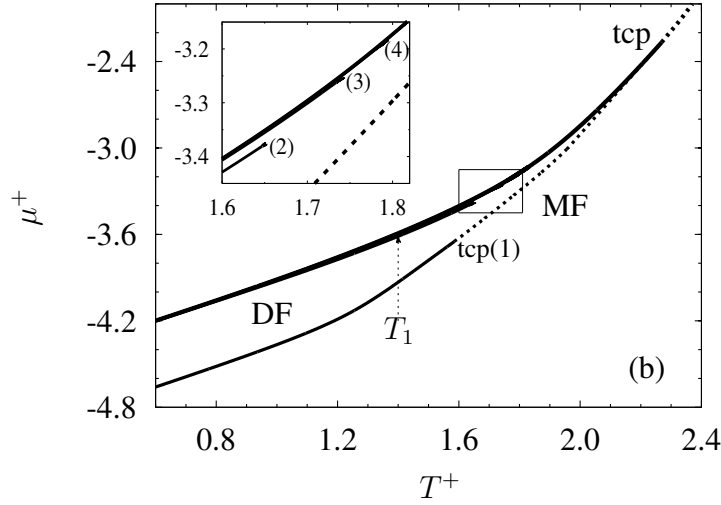


Figure 5.13: As Fig. 5.5 but for $\epsilon_{AB}^* = 0.3$. (a) $\epsilon_W^+ = 1.6$; (b) $\epsilon_W^+ = 2.0$.

(MF) monolayer films. The latter is formed continuously from the gas phase, but the demixed film is enclosed by first-order transition lines as Fig. 5.13(a) shows.

If we now increase the fluid–substrate attraction to $\epsilon_W^+ = 2.0$ (see Fig. 5.13(b)), the one-phase region of the demixed film widens. Similar to mixtures of type II in Figs. 5.11(b) and (c), the coexistence line pertaining to gas+demixed film ends at a surface tricritical point tcp(1) at which the surface λ -line starts. Thus, the transition from demixed to mixed monolayer is either first- or second-order. In addition, Fig. 5.13(b) also reveals that a number of thicker films appears. This is discussed in more detail in the following paragraph.

Complete Wetting. The inset in Fig. 5.13(b) shows that a number of additional layer-coexistence lines arise (i.e., (2), (3), and (4) are specified). Consider now the isotherm T_1 in Fig. 5.13(b). We plot the excess coverage Γ and miscibility M along that isotherm in Fig. 5.14. The parallel discontinuous increase of Γ and M at $1 - \mu/\mu_0 \simeq -0.095$ indicates that at this point the isotherm crosses the coexistence line between gas and demixed monolayer in Fig. 5.13(b). As we move closer towards bulk condensation (A+B-region) along T_1 , additional layering transitions are visible in the plot of Γ which finally diverges at bulk coexistence. Because M increases discontinuously as well in Fig. 5.14, the newly formed thicker films are even more demixed. Hence, in that case the solid substrate is completely wet by demixed films for low temperatures $T \geq 0$.

Returning to the phenomenological argument in Sec. 5.1.2, that is $T_w = 0$ if $\epsilon_W/\epsilon_{ff} \geq 1$, we have in this case $\epsilon_W^+ = 2.0$ and $\epsilon_{ff} = \epsilon_{AA}$, because we are dealing with *demixed* films. From this we obtain $\epsilon_W/\epsilon_{ff} = 1.3$, which is indeed greater than 1. Thus, complete wetting here at zero temperature agrees with the phenomenological

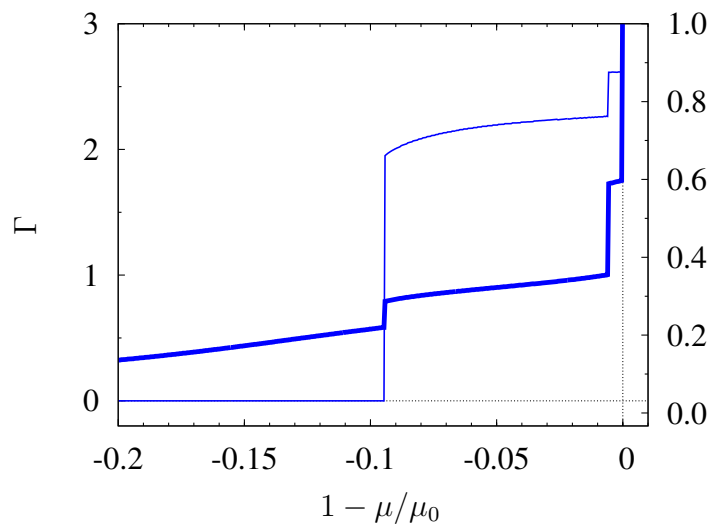


Figure 5.14: As Fig. 5.9 but for the isotherm T_1 specified in Fig. 5.13(b).

argument.

However, the layering coexistences become critical within the demixed region DF in Fig. 5.13(b) and are therefore not detectable in the sense of individual equilibrium phases for higher temperatures. For even higher temperatures but below T_{tcp} the film becomes mixed (MF) upon crossing the surface λ -line.

Confined Symmetric Mixtures

The phase behavior of pure fluids and their mixtures in confined geometries is currently receiving a lot of experimental and theoretical attentions. The comprehensive review of Gelb *et al.* [52] gives a summary of phase equilibria of *pure* fluids in porous materials of gas+liquid, layering, and freezing/melting in simple and also more complex pore geometries. The study of pure fluids is extended within the framework of different approaches: the impact of structured, corrugated, and heterogeneous pore walls on the phase behavior was first investigated by Röcken *et al.* [164, 165] and Schoen *et al.* [81, 146, 159, 166–170]. These authors also discussed the role of surface-induced bridge phases. The structure of thin layers and their freezing was studied by Vishnyakov [171] and Sałamacha [172], whereas Pitard *et al.* [173], Kierlik *et al.* [73, 74] and Klapp *et al.* [75] analyzed hysteresis effects and the role of metastable phases.

More recently, *binary* mixtures in pores received more attention both experimentally and theoretically. Recalling the complex behavior of mixtures in bulk and at solid substrates discussed in Chapters 4 and 5, we expect a large number of scenarios for phase transitions and phase separations including the appearance of film phases and adsorption/desorption phenomena. Because of the large number of model parameters, most of the theoretical works are concerned with symmetric mixtures or special

cases of parameter sets. Nevertheless, these works extend our perception of the behavior of pure adsorbates in simple pore geometries. Density functional theory was employed by Telo da Gama and Evans [49], Marconi and van Swol [174], Sliwinska-Bartkowiak *et al.* [67, 68], and Sokołowski *et al.* [78, 79, 175, 176]. Also, phase equilibria were analyzed via Monte-Carlo [65, 66, 76, 77, 177] and molecular dynamics simulations [65, 178]. Other approaches were a liquid-state formalism describing a randomly disordered matrix [179], a lattice mean-field model [147], a mean spherical approximation [180] and an optimized random phase approximation [76, 77]. As all these theoretical works focus mainly on the phase and wetting behavior of confined mixtures, we include them into the present discussion.

Experimentally, the phase separation in porous materials was observed for a variety of systems such as lutidine+water in vycor [181], iso-butyric acid+water in dilute silica gel [64], $^3\text{He}+^4\text{He}$ mixture in porous gold [122], $n\text{-C}_6\text{H}_{14}+n\text{-C}_8\text{F}_{18}$ in vycor [182, 183], n -hexane+perfluoro- n -hexane vapor between two mica surfaces [184], 2-butoxyethanol+water [62] and iso-butyric acid+heavy water [145] both confined to mesoporous silica glass. Results obtained within the latter two studies will be further discussed in Part III of this thesis where we apply our approach to actual laboratory experiments.

Structure and domain growth in binary mixtures were discussed theoretically [45–47, 69, 70, 185–188] and experimentally [72, 189–193]. Diffusional properties and kinetics were also studied by experiments [61, 145, 194–196] and by theoretical models [71, 197–199]. Finally, the investigations were extended by introducing temperature-dependent interactions [200] or a third mixture-component [201]. In addition, effective forces acting between the two plates forming a slit pore were discussed by Patey *et al.* [66, 202]. Kanamori *et al.* [203] examined solidification and the structure of confined, quenched silica gels.

The following study on symmetric binary mixtures confined between two nonselective solid substrates (slit-pore geometry) consists of two parts. First, we analyze the phase behavior of confined mixtures of the three principal mixture types (i.e., type I, II, and III) introduced in Sec. 4.2.5. Here we investigate the role of the pore width n_z and of the strength of the fluid–substrate attraction ϵ_w on the phase diagrams. Second, we study the dependence of critical and critical-end points on the degree of confinement. In addition, we demonstrate that the decomposition of binary mixtures as well as appearance and character of surface-induced film phases can be controlled by n_z and ϵ_w .

6.1 Phase Behavior of Confined Mixtures

Since the parameter space is large, we focus in this chapter exclusively on symmetric binary mixtures, that is

$$\epsilon_{\text{BB}}^* = 1, \quad \Delta\mu = 0, \quad (6.1)$$

which are described in Sec. 4.2.5. Such mixtures are confined to a slit-pore geometry of pore width n_z . Both components of the fluid mixture interact with the *nonselective* solid substrates via the short-range attraction of Eq. (2.25) with $\epsilon_{WA} = \epsilon_{WB} \equiv \epsilon_W$.

In the following section we study the phase behavior of the three possible types of symmetric binary mixtures. In order to visualize the stable phases based on T - μ and ρ - T projections of the phase diagrams where ρ is the total (mean) density of the pore fluid, that is

$$\rho \equiv \frac{1}{n_z} \sum_{z=1}^{n_z} \rho_z. \quad (6.2)$$

Since the nonselective solid substrates preserve the $m_z \leftrightarrow -m_z$ symmetry of the system, a demixed phase still corresponds to A+B coexistence. In this sense the two projections contain the full information about the phase behavior. We note that the total density is an appropriate order parameter to determine the phase behavior of confined binary mixtures in contrary to the previous discussion of wetting in Chapter 5, where we had to use (integral) order parameters Γ and M .

6.1.1 Type-I Mixtures

We begin with the symmetric binary mixture of type I which can be realized by choos-

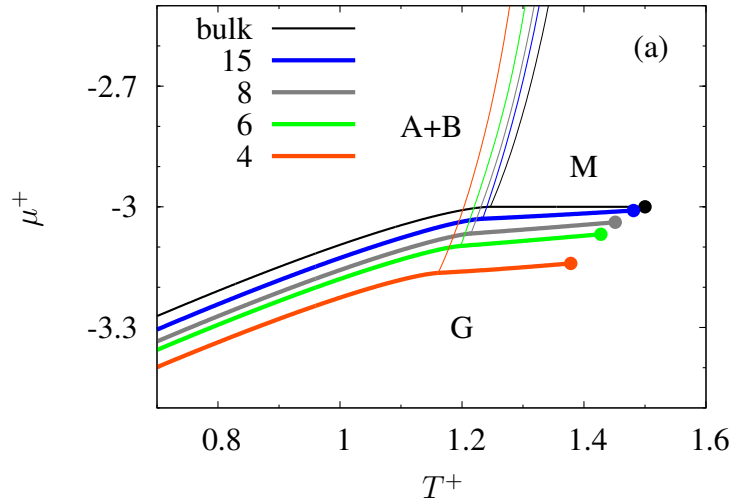


Figure 6.1: Ctnl.

ing $\epsilon_{AB}^* = 0.6$. Figure 6.1 shows the phase diagram in the two projections for various pore widths n_z and fixed value of $\epsilon_W^+ = 0.87$. First, the type of the mixture is preserved for our choice of parameters, but we see that the gas+liquid coexistence line (thick lines in Fig. 6.1(a)) moves to lower chemical potentials with decreasing n_z . This

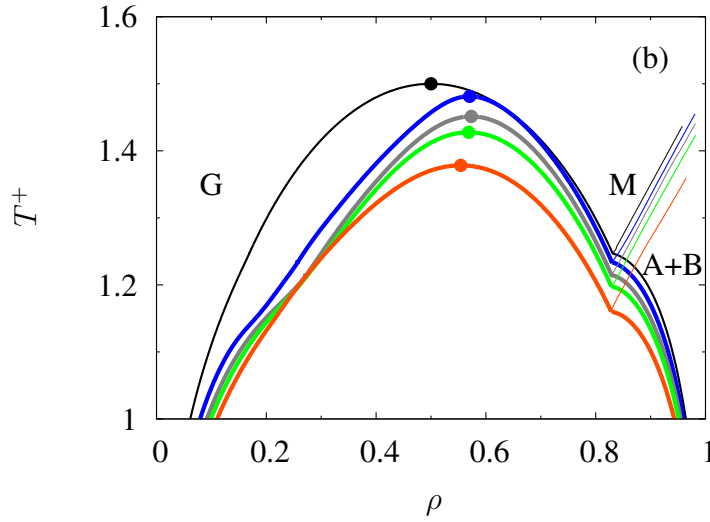


Figure 6.1: Phase diagrams for $\epsilon_{AB}^* = 0.6$ and $\epsilon_W^+ = 0.87$ in (a) $T-\mu$; (b) $\rho-T$ projection for various pore widths n_z as indicated in the key in (a). Thick (thin) lines represent first-order (second-order) phase transitions. Dots mark gas+mixed liquid critical points.

effect is known as capillary condensation and refers to a situation in which the (attractive) solid substrates promote condensation of a *confined* gas at chemical potentials at which a corresponding *bulk* system would still be a thermodynamically stable gas. For mixtures of type I we have of course to distinguish between mixed and demixed liquid phases separated by the (critical) λ -line (thin lines). This line shifts toward lower temperatures the more confined the liquid is, that is the smaller n_z becomes (see Fig. 6.1). This effect is strong only for very narrow pores. We note that the λ -line consists of liquid+liquid (A+B) critical points, so that the corresponding critical temperature decreases with higher degree of confinement. Most of the previous works on confined mixtures focused on liquid+liquid coexistence and also found a depression of their critical points [65–68, 177]. Because of our nonselective walls, we do not see a shift of the critical concentration (i.e., total miscibility m) toward the preferentially adsorbed component. Thus, the critical miscibility¹ in our model stays at $m_c = 0$.

Also, we observe the expected shift of the gas+mixed liquid critical point (dots in Fig. 6.1) to lower temperatures. This depression is the more pronounced the narrower the pore is. The effect agrees with previous results on pure fluids [1, 52] and binary mixtures [77, 79, 147, 174]. However, as can be seen in Fig. 6.1(b) the gas+mixed liquid critical density is first shifted to higher values ($n_z = 15$) and decreases subsequently with decreasing n_z if n_z is sufficiently small (i.e., $n_z = 6, 4$). Such non-monotonic behavior, not observed for pure fluids, was reported by other authors [175],

¹which is visible in neither phase diagram projections.

too and is only found for weakly attractive substrates. With decreasing critical temperature the entropy contribution decreases while the potential-energy terms dominate. Thus, since $\epsilon_{\text{W}}^+ < 1$ we observe drying effects in the liquid phase leading to a decrease of the density inside the pore. This is the more pronounced the smaller the pore is.

Another confinement effect, that has no counterpart in pure fluids, can be seen in Fig. 6.1(a). It concerns a downward shift in T and μ of the critical end point (contact point of thin and thick lines) with decreasing n_z . The total density at that point remains nearly constant as Fig. 6.1(b) shows. A detailed analysis of the interplay of confinement and locations of critical and critical-end points is deferred to Sec. 6.2.1

Let us now concentrate on the appearance of surface-induced film phases. In order to generate such films (see Chapter 5) we increase the strength of the substrate attraction to $\epsilon_{\text{W}}^+ = 1.87$. Figure 6.2 shows the phase diagram for such a system for $n_z = 15$.

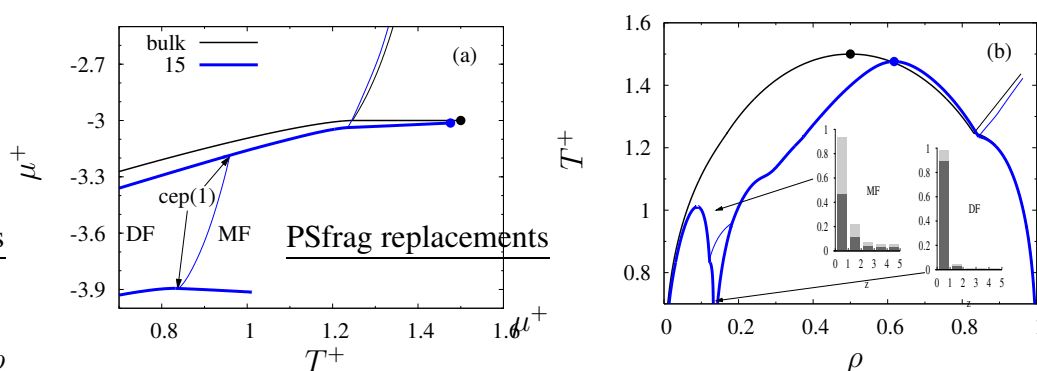


Figure 6.2: As Fig. 6.1 but for $\epsilon_{\text{W}}^+ = 1.87$. Exemplary density profiles for demixed (DF) and mixed (MF) films for $n_z = 15$ are shown in the insets where the shading of the bars refers to the local amounts of component A and B, respectively (only the part close to *one* wall is displayed).

We observe demixed (DF) and mixed (MF) film phases which are located between the gas and the liquid phases (see Fig. 6.2(a)). For low temperatures the demixed film (A-rich and B-rich films in coexistence) is stable but becomes critical at its critical (surface) λ -line and passes into the (single) mixed film for higher temperatures in accord with other work [79]. This λ -line meets the gas+film coexistence curve *below* and that of the film+demixed liquid coexistence *above* at the two surface critical end points (cep(1)). The gas+mixed film coexistence ends at a surface critical point at $T_{\text{lc}}^+ = 1.01$ and $\mu_{\text{lc}}^+ = -3.9$.

The same phase behavior is reflected by Fig. 6.2(b) where the phase diagram is shown in the ρ - T projection. Two representative density profiles (histograms) illustrate the local structure of demixed and mixed film phases. As one can see, such a film consists of two monolayers adsorbed at either walls². The monolayers of the two films

²The opposite wall is omitted in the histograms.

have nearly equal densities characteristic of a liquid but differ in composition (see inset of Fig. 6.2(b)). A detailed study of the influence of the confinement on the character of the film phases is deferred to Sec. 6.2.3.

6.1.2 Type-II Mixtures

We now turn to confined mixtures of type II which we realize by setting $\epsilon_{AB}^* = 0.5$ (see Sec. 4.2.5). The phase behavior of a confined type-II mixture is illustrated by Fig. 6.3 for various pore widths but fixed $\epsilon_W^+ = 1.73$. For wide pores (i.e., $n_z = 12$)

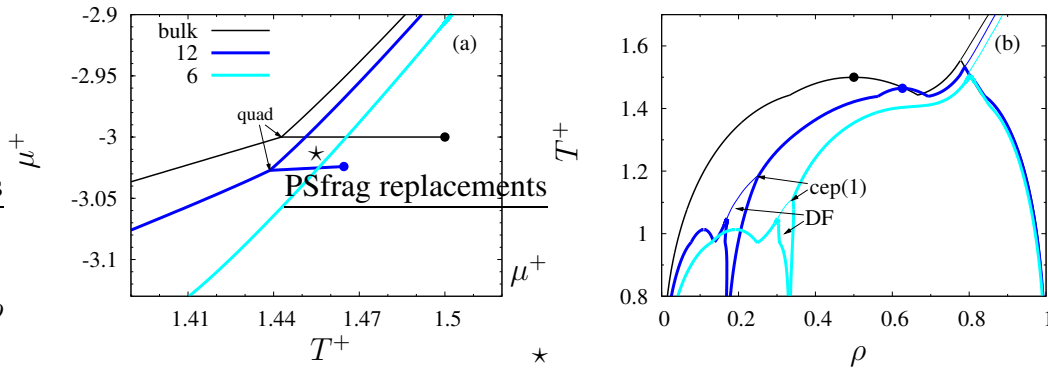


Figure 6.3: As Fig. 6.1 but for $\epsilon_{AB}^* = 0.5$ and $\epsilon_W^+ = 1.73$.

we observe a remarkable shift of the gas+mixed liquid critical density from $\rho_c = 0.5$ (bulk) to $\rho_c = 0.63$ and the usual depression of the corresponding critical temperature as can be seen in Fig. 6.3(b). Additionally, we see a shift of the tricritical points toward higher densities and lower temperatures in agreement with [79]. Moreover, similar to type-I mixtures the liquid+liquid λ -line shifts to lower temperatures so that all liquid+liquid coexistence curves are also shifted to smaller temperatures in accord with the aforementioned works [65–68, 177].

For smaller pores with $n_z = 6$ Fig. 6.3(b) reveals that the gas+mixed liquid coexistence vanishes. Now the gas+demixed liquid coexistence curve ends at a tricritical point without any further phase transition. Therefore, the mixture changes its type from II to III depending on the degree of confinement. We return to this fact later in Sec. 6.2.2. This confinement-induced absence of the gas+mixed liquid critical point was also found by Binder *et al.* [148], Schöll-Paschinger *et al.* [77], and Sokołowski *et al.* [79, 176].

For lower temperatures and lower densities we again find film phases as for type-I mixtures (see Fig. 6.3(b)). But here, the demixed films (DF) coexist with the mixed ones along a line of first-order phase transitions. Such a first-order mixed+demixed film coexistence was observed by Binder *et al.* [148] for confined symmetric binary polymer blends. This coexistence line ends at a surface tricritical point and turns into

the surface λ -line which connects to the film+demixed liquid coexistence curve at a surface critical end point (cep(1) in Fig. 6.3(b)). Moreover, similar to type-I mixtures the gas+mixed film coexistence terminates at the surface critical point at about $T_{sc}^+ \simeq 1.01$ for the two confined mixtures. A qualitatively similar film-phase behavior for confined mixtures was reported by Sokołowski *et al.* [79, 176].

A cut-out of the corresponding T - μ projection of that phase diagram is shown in Fig. 6.2(a) where the film phases are outside the range plotted. However, one observes that the gas+mixed liquid coexistence is apparent in bulk and for $n_z = 12$ but vanishes for $n_z = 6$ which causes the quadruple point (quad) to disappear, at which A-rich, B-rich, mixed liquids and gas coexist. Moreover, capillary condensation, that is the downward shift of the gas+demixed liquid, is quite pronounced.

6.1.3 Type-III Mixtures

For mixtures of type III represented by $\epsilon_{AB}^* = 0.4$, the stable gas+mixed liquid coexistence is absent, even in the bulk (see Sec. 4.2.5). Figure 6.4 displays the ρ - T

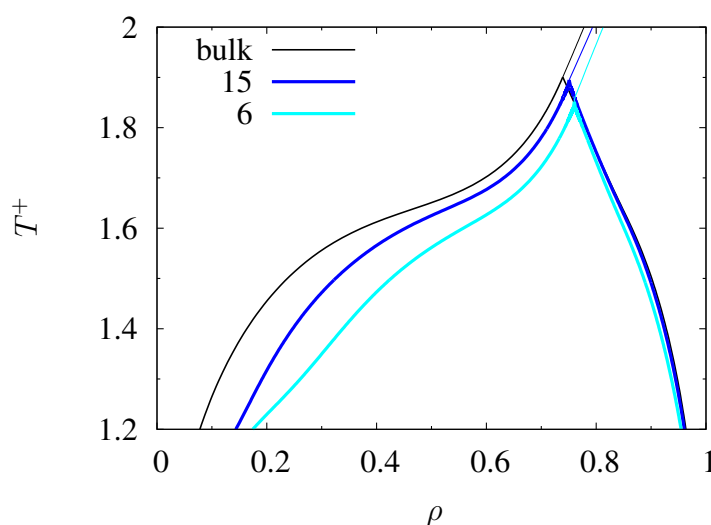


Figure 6.4: As Fig. 6.1(b) but for $\epsilon_{AB}^* = 0.4$ and $\epsilon_W^+ = 1.43$.

projection of the phase diagram for various pore widths but fixed substrate attraction strength $\epsilon_W^+ = 1.43$. The shape of the coexistence curves is almost identical regardless of n_z , except for a small shift of the tricritical point toward lower temperatures and larger densities similar to the behavior of tricritical points of type-II mixtures (see Fig. 6.3(b)). This can be understood because the correlation length associated with density fluctuations cannot increase beyond the distance between the pore walls leading to a depression of the tricritical temperature. Our mean-field model cannot account for density fluctuations but since the film profiles of the gas phase decaying from either walls

overlap, the gas and the liquid become indistinguishable at lower temperatures the smaller the pore is. Also, the enhanced adsorption at the walls leads to an increase of the total density of the coexisting gas phase (see Fig. 6.4) for this choice of $\epsilon_W^+ = 1.43$. Thus, the density at the tricritical point is shifted to higher values. As found for mixtures of other types before, the liquid+liquid λ -line is shifted to lower temperatures (for constant ρ) leading to a depression of the corresponding liquid+liquid coexistence curves.

For this rather weak substrate attraction we do not find any stable film phases. However, this changes upon increasing ϵ_W^+ . Figure 6.5 shows the phase diagram for

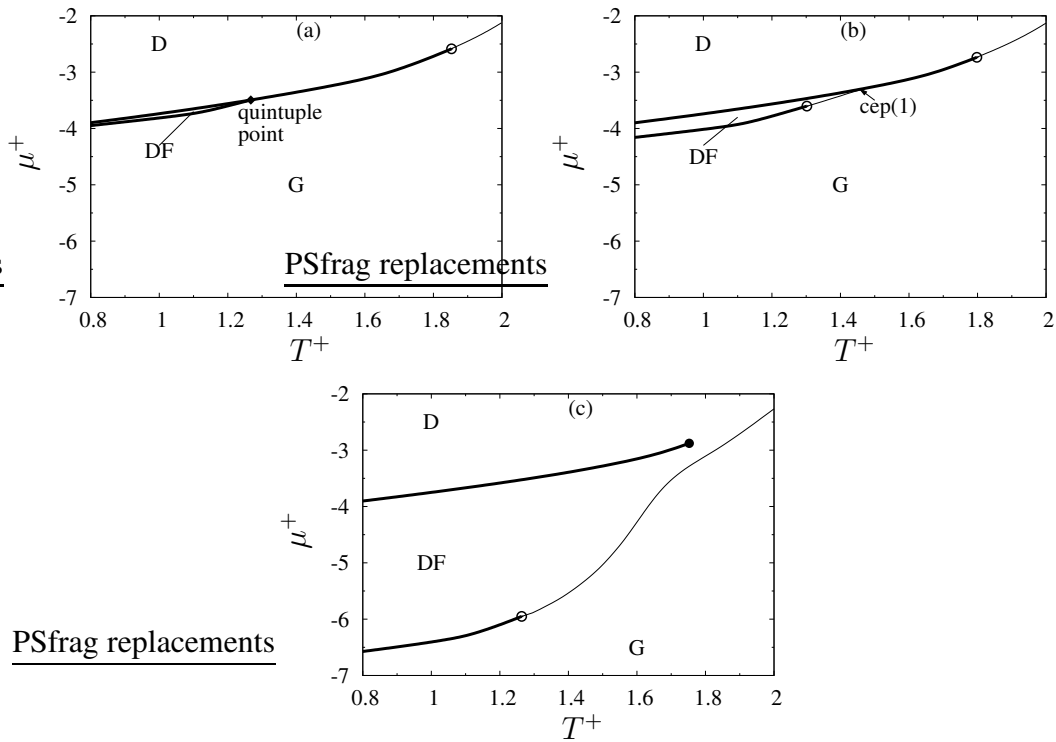


Figure 6.5: As Fig. 6.1(a) but for $\epsilon_{AB}^* = 0.4$, $n_z = 10$, and various values of ϵ_W^+ (a) 1.64; (b) 1.86; (c) 4.3. Open dots (o) represent tricritical points.

the same mixture for fixed pore width $n_z = 10$ but various values of ϵ_W^+ in the T - μ projection. For $\epsilon_W^+ = 1.64$ (Fig. 6.5(a)) the demixed film (DF) emerges between gas (G) and demixed liquid (D) coexistence for low temperatures. The G+DF and DF+D coexistence lines join at a surface quintuple point (A- and B-rich liquids, A- and B-rich films, gas) at $T_{\text{qui}}^+ = 1.27$ and $\mu_{\text{qui}}^+ = -3.5$. Therefore, the demixed film is completely surrounded by lines of first-order transitions. Above the quintuple temperature gas coexists with demixed liquid via first-order transitions until the ordinary tricritical point (o) is reached.

If ϵ_W^+ increases further to a value of 1.86 (Fig. 6.5(b)) the quintuple point disap-

pears. Instead a surface tricritical point arises at $T_{\text{tcp}}^+(1) = 1.30$ and $\mu_{\text{tcp}}^+(1) = -3.6$ involving gas, A-rich and B-rich films. At this tricritical point a surface λ -line starts which intersects the G+D coexistence line at the surface critical end point (cep(1)) at $T_{\text{cep}}^+(1) = 1.48$ and $\mu_{\text{cep}}^+(1) = -3.3$. For $T > T_{\text{cep}}^+(1)$ gas and demixed liquid coexist along the thick line until they become indistinguishable at the tricritical point where the ordinary (A+B) λ -line begins.

For even larger $\epsilon_{\text{W}}^+ = 4.3$ the plot in Fig. 6.5(c) indicates that the cep(1) disappears. The G+DF coexistence line is shifted to lower chemical potentials ending at a surface tricritical point where the surface λ -line starts. In contrast to the previous case this line does no longer intersect the line of first-order DF+D transitions. Therefore, above that λ -line the fluid is always demixed. This leads to film+liquid coexistence (both demixed) ending at a true critical point³ at $T_{\text{c}}^+ = 1.75$ and $\mu_{\text{c}}^+ = -2.9$. This effect is remarkable because the total density of the demixed film phase adsorbed on the substrates is relatively low so that ordinarily one would anticipate a stable mixed film phase.

This scenario was also reported by Martinez *et al.* [79] but because of the different (long-range) fluid–substrate potential they found the separation of the λ -line even for larger pores. Also, $^3\text{He}+^4\text{He}$ mixtures, which are of type III in the bulk (see Sec. 4.2.5), confined by porous gold or aerogel [121, 122] exhibit a similar behavior. The transition λ -line between normal (corresponding to the mixed one here) and superfluid (demixed here) liquid phases is detached from the $^3\text{He}+^4\text{He}$ coexistence curve (gas+liquid here) and the coexistence region lies entirely within the superfluid part of the phase diagram. As can be seen in Fig. 1 of [122] the top of the $^3\text{He}+^4\text{He}$ coexistence curve is also a regular critical point.

6.2 Impact of Confinement

6.2.1 Critical Points and Critical End Points

Suppose now we have a typical mixture of type I with $\epsilon_{\text{AB}}^* = 0.6$. As already seen in Sec. 6.1.1 the confined mixture exhibits a gas+mixed liquid critical point which depends on the pore width n_z and on the fluid–substrate interaction strength ϵ_{W} .

From Fig. 6.6 it is obvious that increasing ϵ_{W} causes a substantial depression of T_{c} for fixed and sufficiently small values of n_z . The depression of T_{c} can be understood in terms of enhanced gas adsorption at the walls with increasing ϵ_{W} . Thus, for a given T the total densities of coexisting gas and liquid are less different the larger ϵ_{W} becomes. Consequently, the temperature T_{c} of the critical point, at which the two become identical, decreases with increasing ϵ_{W} similar to the tricritical temperatures discussed in

³Strictly speaking, this coexistence curve consists of quadruple points which ends at a *double* critical point, where A-rich film+liquid and B-rich film+liquid coexistences become critical simultaneously. The A+B coexistence remains first-order until it meets the λ -line.

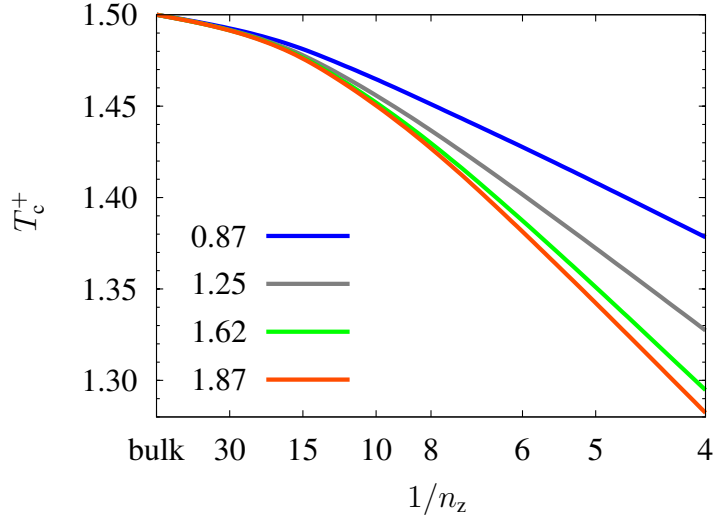


Figure 6.6: Critical gas+mixed liquid temperature T_c^+ as a function of the reciprocal pore width for various fluid–substrate interaction strengths, ϵ_W^+ , as indicated in the figure ($\epsilon_{AB}^* = 0.6$).

Sec. 6.1.3. Here the depression of T_c is more pronounced with decreasing pore width (see Fig. 6.6). This is because the finite pore space in the z -direction limits the growth of adsorbed films. Thus, if the range of film thicknesses becomes comparable with the pore width, gas and liquid are no longer distinguishable.

Let us now study the behavior of the critical end point. Its temperature is plotted as a function of n_z for various ϵ_W in Fig. 6.7. Similar to the critical temperature, T_{cep} decreases with increasing pore width in accord with the works of Bucior *et al.* [78] and Martinez *et al.* [79], who found a stronger depression of T_{cep} . For larger $\epsilon_W^+ \geq 1.25$, T_{cep} increases with the strength of the fluid–substrate attraction, contrary to the change of T_c with ϵ_W . Both effects seem plausible if one realizes that the total density increases for larger ϵ_W on account of more pronounced adsorption. Since the increase of the gas density is larger than that of the liquid density, T_c decreases as mentioned above. On the other hand, a (small) increase in liquid density may cause decomposition of the liquid because the present choice of $\epsilon_{AB}^* = 0.6 < 1$ promotes demixing energetically. Thus, the critical end point temperature increases for larger ϵ_W . However, if the liquid density decreases due to weak substrate attraction (drying effect), e.g. for $\epsilon_W^+ = 0.87$, the opposite would be true. Now, because of the entropy, the system favors mixing of the two components rather than decomposition. This can be seen in Fig. 6.7 where the curve of $\epsilon_W^+ = 0.87$ is intermediate to those pertaining to $\epsilon_W^+ = 1.25$ and 1.62.

However, compared with the confinement-induced shift of T_c the impact of varying ϵ_W is quite small as far as T_{cep} is concerned. Moreover, it is gratifying that the depression of both, T_c and T_{cep} , diminishes rather quickly as $n_z \rightarrow \infty$ so that a smooth extrapolation of our results to the bulk limit is achieved. In addition, the phase dia-

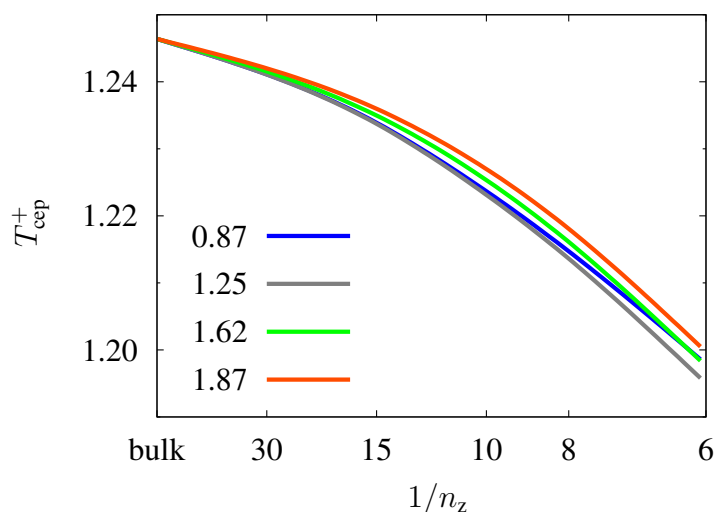


Figure 6.7: As Fig. 6.6 but for critical-end-point temperature T_{cep}^+ .

grams are topologically unaffected upon varying n_z and ϵ_w .

6.2.2 State and Decomposition

The discussion in Sec. 6.1.2 already revealed that it is possible to switch between various types of phase diagrams with profound consequences for liquid+liquid and gas+liquid phase equilibria. This may have practical implications for the condensation of gas mixtures or for the decomposition of mixtures of immiscible liquids.

Consider as an example a system where $\epsilon_{AB}^* = 0.5$ (see Fig. 6.3 for plots of phase diagrams for various pore widths n_z) and suppose one fixes the thermodynamic state such that the mixture is a gas in the bulk (\star in Fig. 6.3(a)). On account of the confinement induced shift of the phase diagram the system turns out to be a mixed liquid in a slit pore with $n_z = 12$. In this rather wide pore, however, the phase diagram is topologically equivalent to the one for the bulk. This changes for a narrower pore of $n_z = 6$ as Fig. 6.3(a) shows. Consequently, between $n_z = 12$ and $n_z = 6$ the confined liquid mixture changes its physical nature from mixed to demixed. This process is further illustrated by the plots in Fig. 6.8 where the total density ρ of thermodynamically stable confined phases is plotted as a function of n_z (i.e., the pore width). Three different branches are discernible. For small $n_z < 8$, ρ is relatively high indicating that the pore is filled with liquid. A corresponding plot of the local densities of a representative phase for $n_z = 5$ shows that this liquid consists of an A- (or B-) rich, high-density fluid (since the two cannot be distinguished in a symmetric mixture). Hence, for $n_z < 8$ we observe decomposition of liquid mixtures. For intermediate pore widths, that is for $8 \leq n_z \leq 16$, ρ is somewhat smaller than for the tightest pores ($n_z < 8$). An inspection

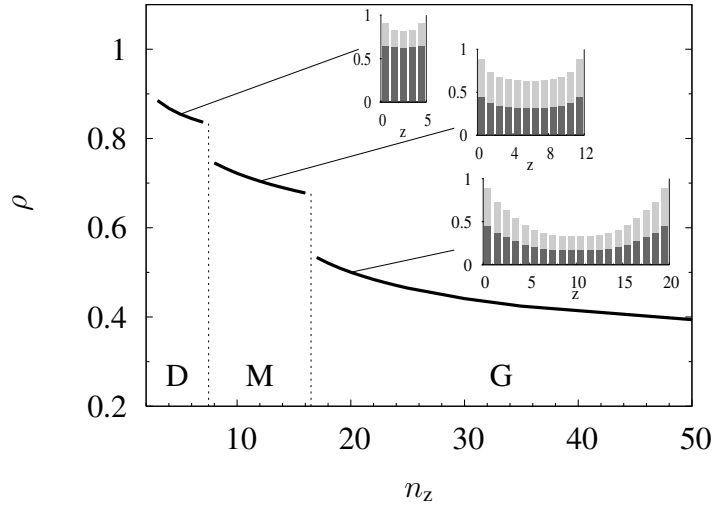


Figure 6.8: Mean pore density ρ as a function of pore width n_z for the thermodynamic state marked by a \star in Fig. 6.3(a) (i.e., $T^+ = 1.453$, $\mu^+ = -3.01$, $\epsilon_{AB}^* = 0.5$, $\epsilon_W^+ = 1.73$). Stability limits between pairs of phases are indicated by vertical lines. Exemplary density profiles for each stable phase (i.e., D, M, and G) are shown.

of a prototypical plot of the local densities for $n_z = 12$ reveals that the confined phase now consists of an equimolar mixture. Hence, for intermediate pore sizes the confined phase is a mixed liquid. Finally, for $n_z > 16$, ρ is even smaller than along the two previously discussed branches. The local density of a representative state for $n_z = 20$ now clearly shows that a comparatively low-density fluid exists at the center of the pore. As either substrate is approached the density increases indicating that this mixture wets the substrates. However, as expected for such a “gas” state the fluid consists of an equimolar mixture similar to states along the intermediate branch $8 < z < 16$. The change of ρ between a pair of branches is discontinuous at characteristic pore widths where first-order transitions occur between these phases.

Thus, by choosing an appropriate pore width one can either promote condensation of a gas to a mixed liquid phase, or initiate liquid+liquid phase separation in the pore. Sokołowski *et al.* [79, 175] and Schöll-Paschinger *et al.* [77] also showed that the type of the mixture may be tuned by the degree of confinement in qualitative agreement with our result of Sec. 6.1.2. These authors reported topological changes of phase diagrams between types I \rightarrow II and II \rightarrow III as the pore width decreases.

6.2.3 Film Phases

Similar considerations apply to the nature of film phases as the degree of confinement varies. Such film phases which are adsorbed monolayers at the two walls have a *lo-*

cal density similar to that of a liquid phase. Typical examples for density profiles of demixed and mixed films are shown as insets in Fig. 6.2(b).

The discussion in Secs. 6.1.1 and 6.1.2 showed that the transition between these film phases may be of first- or second-order. In this section we investigate the influence of n_z and ϵ_w on such films. Consider the case of $\epsilon_{AB}^* = 0.6$. From Figs. 6.1 and 6.2 we see that an increase of ϵ_w^+ from 0.87 to 1.87 leads to the appearance of stable film phases which are demixed for low and mixed for higher temperatures.

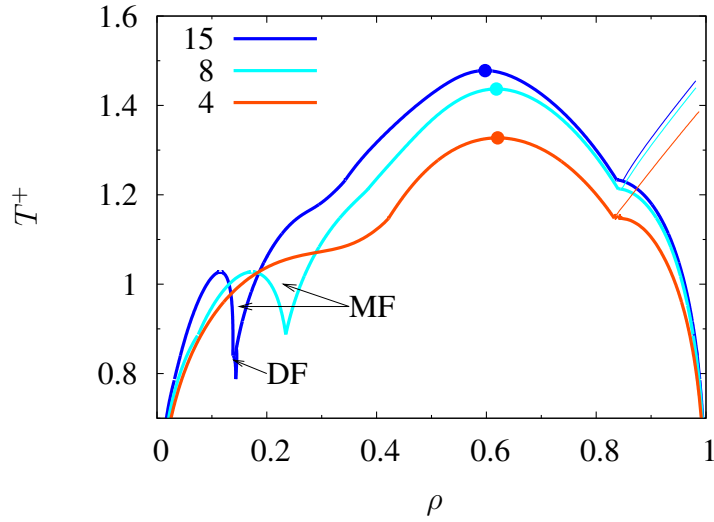


Figure 6.9: As Fig. 6.2(b) but for $\epsilon_w^+ = 1.25$.

Examining the somewhat intermediate case of $\epsilon_w^+ = 1.25$, for which phase diagrams for $n_z = 15, 8$, and 4 are displayed in Fig. 6.9, we observe a demixed film (DF) for wide pores ($n_z = 15$) and low temperatures. The demixed film becomes mixed at $T^+ = 0.85$ via a second-order phase transition. When decreasing the pore width to $n_z = 8$, the demixed film is no longer thermodynamically stable and only the mixed film arises. For even smaller $n_z = 4$ we do not find any film at all. These effects are caused by capillary condensation, which is more pronounced for narrow pores, thus preventing film phases from forming. In other words, for narrow pores wetting is subdominant to capillary condensation according to one's physical intuition. Thus, by choosing appropriate values of n_z and ϵ_w one cannot only trigger adsorption of films at the walls but can also change their composition.

Part III

Comparison with Experimental Data

We now apply our model to experimental data for binary mixtures imbibed in mesoporous solid matrices. Experimentally, a porous medium affects a fluid mixture not only by mere confinement to volumes of nanoscopic dimensions [66](see Chapter 6) but also by the selectivity of the solid substrates, that is the substrates' energetic preference for molecules of one mixture component over the other [35, 52, 68]. In addition to substrate *selectivity* most mixtures exhibit an *asymmetry* in interactions between the pairs of like molecules (A–A and B–B). As we have seen in Part I and II of this thesis both features can be incorporated by our model. Hence, we apply it here to an experimental system with the goal of supporting the interpretation of the experimental data by providing additional information that is experimentally inaccessible.

In this regard, one realizes that most experiments examine mixtures separating into two *liquid* phases (A+B) of different composition below a critical solution point T_c (see Chapter 4 for liquid+liquid coexistence). Therefore, the gas phase does not play an important role and is consequently disregarded to simplify the subsequent theoretical treatment [52]. In that sense, similar to the equivalence between gas+liquid and liquid+liquid coexistences in Ising-models [80], there are two kinds of *long-range* phenomena near liquid+liquid (A+B) coexistence:

- (i) composition fluctuations near the A+B critical point
- (ii) multilayer adsorption of the preferred component (say, B) as one approaches the A+B phase coexistence curve from the A-rich side.

For several binary mixtures these long-range adsorption phenomena were indeed observed, either at a free liquid surface (i.e., interfacial wetting, see, for example, [142]) or at some inert solid substrate [127]. They also occur in systems governed by short-range interactions (see Chapter 5).

In narrow pores, on the other hand (see Chapter 6), when the pore width is less than the thickness of an adsorbed layer, concentration profiles near the pore walls overlap at the center of the pore, thereby causing enhanced adsorption. As described above this effect is more pronounced near the A+B critical point [43, 46, 49] and in that one-phase region of thermodynamic state space where molecules (B) of the minor component of the mixture (A-rich phase) are preferentially adsorbed by the substrate.

This situation changes if the confined mixture undergoes a phase separation into A- and B-rich liquids. Note, that the phase transition strongly depends on the degree of confinement (see Chapter 6). This separation cannot occur on a macroscopic length scale. Instead, microphase separation of the system may lead to (metastable) local structures of the two phases in the pore, depending on the relative amounts and strengths of interaction of the two components with the surface [45, 46, 52, 65, 69–72, 145, 181, 184–193, 204]. The structure of microphase-separated mixtures in porous materials is of interest in a variety of different fields, ranging from liquid chromatography or microfiltration and related membrane processes to techniques by which liquids may be extracted from porous materials (for a review see [205]). In the two-phase region flat pore walls are wet, either partially or completely, by that phase in

which the major component (B) is preferentially adsorbed by the substrates [47, 69]. Additionally, in rather irregular porous networks the preferred B-rich phase is located in regions of smaller pore widths [184] whereas the A-rich phase occupies predominantly wider pores or pore junctions [70, 184].

In the present work, the results of two experimental systems are compared with the predictions of our model. First, we study the confinement effect on the adsorption from an amphiphile+water mixture imbibed by controlled-pore glass (CPG-10) materials of different mean pore sizes (10 – 50 nm). Here, the confined mixture remains in the *one-phase* region at the amphiphile-rich side of the phase diagram and is in equilibrium with an external bulk mixture which gives rise to pronounced depletion of the less preferred amphiphile the smaller the pore is. However, for wide pores the adsorption profile decays towards the bulk concentration thus permitting us to calculate the range of composition fluctuations within the pores. The model results agree, at least qualitatively, with differential-refractometer measurements by Rother and Findenegg [62, 206].

Second, we consider the binary system iso-butyric acid+heavy water (iBA+D₂O) inside a porous matrix of CPG-10-75. Model parameters are adjusted such that the calculated liquid+liquid coexistence curve in the bulk matches that of its experimental counterpart. We analyze the complete phase behavior as well as the local structure of the *confined* iBA+D₂O mixture as far as we can carry out our mean-field analysis. Our results are consistent with results of small-angle-neutron-scattering study of Schemmel and Findenegg [63, 145, 207] hence assisting their interpretation.

Confinement Effect on the Adsorption from $C_4E_1+H_2O$ Mixtures

Aqueous systems of solutions of surfactants or amphiphile molecules are of particular interest in view of the relative ease with which one may tune their properties by, say changing the relative lengths of their hydrophilic and hydrophobic (sub)chains. Short-chain members of the family of oligo-ethylenglycol-monoalkyl-ethers, $C_nH_{2n+1}(OC_2H_4)_mOH$ (abbreviated as C_nE_m), are convenient model amphiphiles for such studies. The amphiphilicity of C_nE_m molecules and therefore the location of the liquid+liquid coexistence curve can be tuned by varying the length of the hydrophobic and hydrophilic blocks (i.e., n and m). Liquid solutions of amphiphiles typically exhibit an *upper* miscibility gap in their phase diagram.

In previous experimental studies, interfacial wetting of such systems near liquid+liquid coexistence was analyzed by ellipsometry [208, 209]. Depending on the hydrophilicity and chain length of the C_nE_m molecules, pronounced multilayer adsorption was observed, either on the water-rich or on the amphiphile-rich side of the phase diagram. Critical adsorption from the ethoxybutanol (C_4E_1)+ H_2O system onto atomically flat hydrophilic silicon dioxide substrate was studied by neutron reflectometry

[210]. Preferential adsorption in a porous glass matrix near criticality of the $C_4E_1+H_2O$ system was measured over a wide range of compositions by Gröll and Woermann [211, 212]. Although the authors investigated *confined* $C_4E_1+H_2O$ mixtures, effects arising from confinement were not discussed in view of the large pore size of the macroporous silica matrix used in that study (mean pore size of about 100 nm). However, pronounced H_2O -adsorption at the hydrophilic glass surface was observed in amphiphile-rich liquid phases [211, 212].

The present work addresses the question of how multilayer adsorption within the one-phase region but near liquid+liquid coexistence is affected by confinement. Since composition profiles from two opposing substrates may overlap for sufficiently small substrate distances, the adsorbed amount of the preferred component deviates from that adsorbed at a *single* free surface. Chapter 5 already showed that the excess coverage increases as one approaches bulk coexistence. Accordingly, confinement effects in an one-phase region may be irrelevant well away from coexistence, but become dominant close to two-phase coexistence. The underlying experiments by Rother and Findenegg [62, 206] used a technique closely related to that developed by Gröll and Woermann [211] to study the adsorption of the binary system $C_4E_1+H_2O$ in porous glass (CPG-10) of different average pore sizes varying between 10 and 50 nm. This is well below the mean pore size of the material used by Gröll and Woermann. A detailed account of the experimental setup of Rother and Findenegg is given elsewhere [206].

7.1 Determination of Model Parameters

7.1.1 Interaction Parameters

We consider a binary amphiphile (A) + water (B) liquid mixture. The mixture is contained in some volume divided into cells of equal size on a simple cubic lattice with lattice constant ℓ . We apply our model introduced in Chapter 2 with the modification that cells may now be occupied by more than one molecule thereby taking into account the bidispersity of the mixture (i.e., different sizes of unlike molecules). Since an amphiphile molecule is much larger than a water molecule, a cell occupied by water contains more water molecules than another one occupied by amphiphile. Consequently, the attraction between two water cells (i.e., ϵ_{BB}) is much stronger compared with the weaker attraction between a pair of amphiphile cells and an amphiphile and a water cell. Thus, we assume $\epsilon_{AA} = \epsilon_{AB} = 0$ for simplicity.

In the same manner the selective solid substrate is modeled by the long-range potential of Eq. (2.27) but with $\epsilon_{WA} = 0$ such that the substrate selectively adsorbs water. The average size¹ of the molecules of an 1:1 mixture of C_4E_1 and H_2O is 1.2 nm which is chosen to be the lattice constant ℓ . We set μ to a sufficiently large value such that

¹We assume spherical molecules and mass densities of 0.901 g/cm³ and 1.0 g/cm³ for amphiphile and water, respectively.

the mixture remains in the liquid state regardless of T in accord with the experimental conditions. In other words, we deliberately ignore the presence of a gas phase. Our model system, *formally* equivalent to a one-component gas+liquid system, depends on four parameters, namely temperature $T^* \equiv k_B T / |\epsilon_{BB}|$, incremental chemical potential $\Delta\mu^* \equiv \Delta\mu / |\epsilon_{BB}|$, pore width n_z , and strength of water–substrate attraction $\epsilon_W^* \equiv \epsilon_{WB} / |\epsilon_{BB}|$.

7.1.2 Confinement Parameters

However, in the experimental system the pore geometry of the CPG-10 material is irregular (see Fig. 7.1) rather than slit-like and therefore has a larger surface-to-volume ratio A_p/V_p . To take this geometrical difference into account we introduce the concept

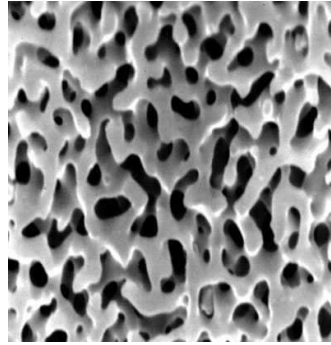


Figure 7.1: Scanning electron micrograph of the CPG-10 material.

of the *hydraulic* radius [62]

$$r_h \equiv 2 \frac{V_p}{A_p}. \quad (7.1)$$

Thus, $r_h = 1/3 d_p$ for spherical pores of diameter d_p , $r_h = 1/2 d_p$ for long cylindrical pores, and $r_h = d_p$ for slits. In order to overcome the problem of modeling different curvatures and shapes between the model slit and the CPG network, we assume that pore matrices with equal r_h have *identically* the same geometrical impact on the confined fluid. For example, a slit pore of width d_p is assumed to be “geometrically equivalent” to a cylindrical pore with diameter $2 d_p$ because for both $r_h = d_p$.

On the other hand, from the ratio r_h/d_p one can “guess” the form of the pores. This ratio is given in Table 7.1 for CPG-10 materials used in the experiment by Rother and Findenegg [62] as well as mean pore sizes d_p and hydraulic radii r_h . We see that r_h/d_p assumes values near $2/3$ at least for small pores. Together with Fig. 7.1 it is then obvious that the CPG-10 pores are irregular but approximately cylindrically in shapes [52, 213]. Silica-based matrices were further studied experimentally by a number of authors [203, 214] and characterized commercially [215] (for a review see [62]).

Material	d_p / nm	r_h / nm	r_h/d_p	l / nm
CPG-10-75	10.3 ± 0.7	6.8	0.66	6.3
CPG-10-240	35 ± 2	23	0.66	7.5
CPG-10-500	50	43	0.86	14.2

Table 7.1: Mean pore size d_p , hydraulic radius r_h , and estimated film thickness l at $w_A = 0.5$ for three CPG materials used in the experiment by Rother *et al.* (see [62] for more details).

In the model we consider slit pores, that is $r_h = n_z \ell$, for the same range of pore sizes used in the experiment. Thus, with $\ell = 1.2 \text{ nm}$ (see above) we vary the pore width from $n_z = 3$ up to $n_z = 100$ which corresponds to hydraulic radii ranging from $r_h = 3.6 \text{ nm}$ to $r_h = 120 \text{ nm}$ (Table 7.1). Note, that for $r_h = 6.8 \text{ nm}$ the model slit pore has a width of 6.8 nm , whereas the geometrically corresponding CPG-10-75 material (see Table 7.1) has a nominal pore size of 10.3 nm . However, the application of the slit-pore geometry to CPG matrices assumes that molecules in different pores do not interact and that the curvatures of the irregular network are accounted for by the concept of the hydraulic radius. Additionally, we calculate the composition profiles for two different water–substrate attraction strengths, $\epsilon_W^* = 2.0$ and $\epsilon_W^* = 4.5$. Note that for $\epsilon_W^* < 1$ one may observe drying phenomena and $\epsilon_W^* > 5$ leads to unrealistically strong preferential adsorption effects which are not of interest here.

7.1.3 Thermodynamic States

It is well known that an *upper* miscibility gap in the phase diagram is a characteristic feature of water+nonionic amphiphile systems [62]. To account for this feature would require strongly *temperature-dependent* interaction parameters [200]. We avoid these complications by restricting our attention to a situation near phase separation for just two temperatures close to each other. In that case we assume that the interaction parameters remain approximately constant.

In the experiment these temperatures are chosen such that the amphiphile-rich phase at bulk coexistence assumes two mass fractions of $w_A^{\text{bulk}} = 0.4$ and $w_A^{\text{bulk}} = 0.5$. We note that the critical mass fraction is $w_{A,c}^{\text{bulk}} = 0.3$ [62]. The corresponding temperatures are $T_{0.4} = 51 \text{ }^\circ\text{C}$ and $T_{0.5} = 58 \text{ }^\circ\text{C}$ for $w_A^{\text{bulk}} = 0.4$ and $w_A^{\text{bulk}} = 0.5$, respectively. We reemphasize that the experimental coexistence curve is concave with a lower critical point so that $T_{0.4} < T_{0.5}$.

Our model bulk system phase-separates at $\Delta\mu^* = -3.0$ (similar to the pure gas+liquid system) but with an upper critical point at $T_c^* = 1.5$. We fix the bulk mass fractions of the amphiphile-rich phase at phase coexistence to the experimental values by choosing $T_{0.4}^* = 1.489$ and $T_{0.5}^* = 1.499$ for $w_A^{\text{bulk}} = 0.4$ and $w_A^{\text{bulk}} = 0.5$, respectively,

where we convert volume fractions² $\rho^A = 1 - \rho^B$ into corresponding mass fractions through

$$w_A = \frac{1}{1 + \kappa(1/\rho^A - 1)}. \quad (7.2)$$

In Eq. (7.2), $\kappa = 0.90$ is the ratio of mass densities of amphiphile (0.901 g/cm³) and water (1.0 g/cm³) at $T = 50$ °C. We note that $T_{0.4}^* < T_{0.5}^*$ on account of the lower miscibility gap.

Experimentally the liquid C₄E₁+H₂O mixture inside the porous matrix is in equilibrium with two bulk mixtures of mass fractions $w_A^{\text{bulk}} = 0.4$ and $w_A^{\text{bulk}} = 0.5$, respectively. Thus, the thermodynamic state remains fixed. Consequently, we also fix the thermodynamic state in the model at $\Delta\mu^* = -3.0$ and $T_{0.4}^* = 1.489$ and $T_{0.5}^* = 1.499$ accordingly and calculate concentration profiles for several pore widths and water–substrate attractions which is subject of the next section.

7.2 Adsorption and Pore Width

Figures 7.2(a) and (b) show the mean mass fraction of amphiphile w_A as a function of the reciprocal hydraulic radius r_h and two water–substrate attractions. The model

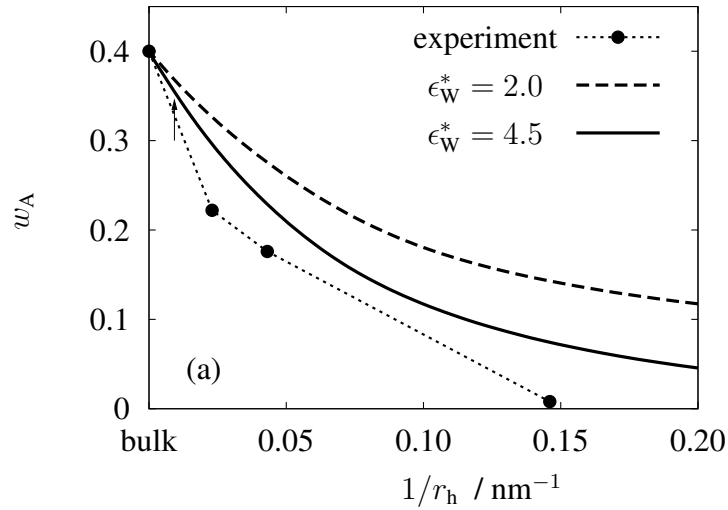


Figure 7.2: Ctnl.

bulk values match those of the experiment as described above. In agreement with the experimental results it is found that the composition of the pore liquid becomes the more depleted of the amphiphile the smaller the pore widths are. As expected, a lower value of ϵ_w^* reduces this depletion effect. Figure 7.2 also illustrates that in the

²for $\mu \rightarrow \infty$, $\rho^A + \rho^B \rightarrow 1$.

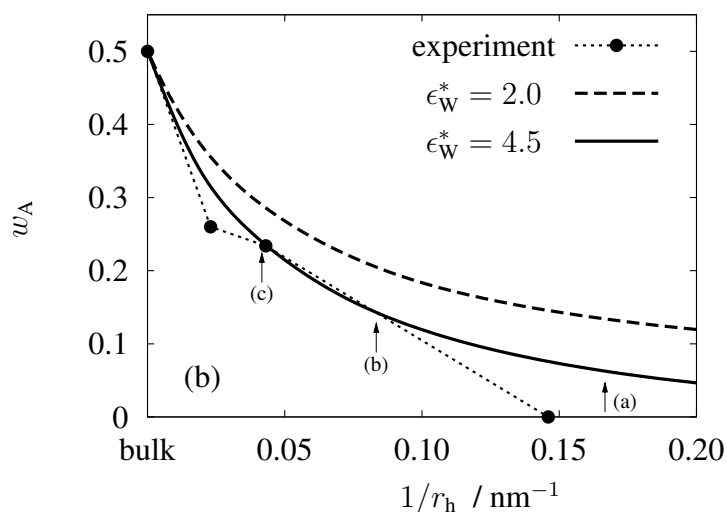


Figure 7.2: Mean mass fraction w_A of the amphiphile in pores as a function of the reciprocal hydraulic radius r_h , where bulk refers to an infinite pore size. Experimental data are compared with two sets of theoretical results for different substrate attractions ϵ_W^* at amphiphile bulk mass fraction (a) $w_A^{\text{bulk}} = 0.4$ and (b) $w_A^{\text{bulk}} = 0.5$.

experiment the amphiphile is completely removed from the porous matrix if $1/r_h = 0.15$ (i.e., CPG-10-75 see Table 7.1). The calculations exhibit a similar trend but only as an asymptotic behavior for larger values of $1/r_h$. This disagreement may be due to the experimental error bars but may also be caused by an increasing inadequacy of the mean-field approximation in cases of very small pore widths. Moreover, the model data for $w_A^{\text{bulk}} = 0.4$ (Fig. 7.2(a)) and $w_A^{\text{bulk}} = 0.5$ (Fig. 7.2(b)) do not fit the data equally well which may reflect a change in strength of intermolecular attractions with increasing temperature. A more detailed picture is, however, still attained if we consider concentration profiles for exemplary pore sizes in the next section.

7.3 Concentration Profiles

The depletion of the amphiphile is further illustrated in Fig. 7.3 which shows the mass fraction profiles for the system $w_A^{\text{bulk}} = 0.5$, $\epsilon_W^* = 4.5$, and different pore sizes indicated by arrows in Fig. 7.2(b). Because of the strong preference of the substrate for water, layers in the vicinity of the two substrates consist of almost pure water. Toward the center of the pore the composition tends toward the bulk mass fraction $w_A^{\text{bulk}} = 0.5$ as the pore width increases. However, the long-range fluid–substrate potential and the long-range composition fluctuations ξ_c near critical coexistence³ lead to a mass

³Note, that $T_{0.5}^* = 1.499$ is very close to $T_c^* = 1.5$.

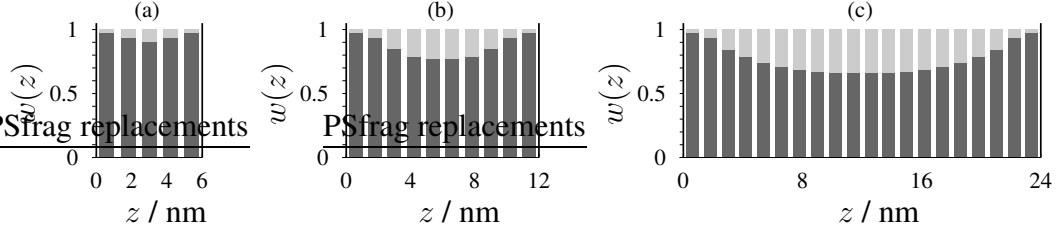


Figure 7.3: Mass fraction profiles $w(z)$ normal to the substrate surface for pore widths (a) 6 nm; (b) 12 nm; (c) 24 nm; as indicated by arrows in Fig. 7.2(b) for $\epsilon_W^* = 4.5$ and $w_A^{\text{bulk}} = 0.5$. Light and dark regions refer to amphiphile ($w_A(z)$) and water ($1 - w_A(z)$) amounts, respectively.

fraction of water near the center of the pore that still deviates significantly from its bulk value of 0.5 even for the largest pore (pore width 24 nm, Fig. 7.3(c)). This pore displayed in Fig. 7.3(c) (24 nm) corresponds to the CPG-10-240 material for which the thickness l of the adsorbed water film⁴ is given by $l = 7.5$ nm (see Table 7.1) which is one fifth of the pore width $d_p = 35$ nm. The corresponding decay length for the model slit may be calculated from $24/5$ nm \approx 4.8 nm which is in the range of the decay in Fig. 7.3(c).

Further insight into the long-range nature of the correlations is gained by plotting the mass fraction profile of amphiphile in a large pore of 108 nm (i.e., $n_z = 90$) relative to its bulk value of $w_A^{\text{bulk}} = 0.4$ indicated by the arrow in Fig. 7.2(a). As shown in Fig. 7.4 the layers close to the substrate again consist of pure water (i.e., $w_A(z) \approx 0$) but in this case the profile decays until it reaches its bulk value ($w_A(z) \rightarrow 0.4$). Because of the mean-field approximation we do not observe oscillations in the profile for small distances from the substrate [126]. The line in Fig. 7.4 represents a fit of a scaling function for critical adsorption proposed by Peliti and Leibler [216] (see also [34]), namely

$$w_A^{\text{bulk}} - w_A(z) = A \left(\sinh \frac{bz}{\xi_c} \right)^{-b} \quad (7.3)$$

where we use a mean-field value of the ratio of critical exponents of $b = \beta/\nu = 1.0$ according to Stanley [162]. The scaling function in Eq. (7.3) decays algebraically ($\propto z^{-b}$) over fluctuation-dominated regions, that is for $z < \xi_c$, and exhibits the usual exponential behavior ($\propto e^{-z/\xi_c}$) in the “tail”-region ($z \gg \xi_c$). However, the short-range behavior is not accounted for by this function, which diverges for small z . The fit of the profile with Eq. (7.3) yields a correlation length of $\xi_c = 16$ nm, which is, in fact, in the range of the estimated film thickness $l = 14.2$ nm of CPG-10-500 pores (see Table 7.1).

⁴estimated from the adsorption excess data for a slap model of water films; see [62].

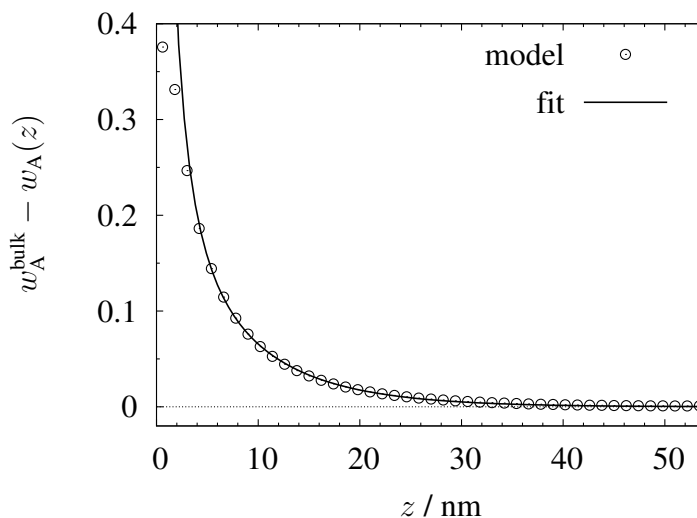


Figure 7.4: Local excess mass fraction profile at $w_A^{\text{bulk}} = 0.4$ for a large pore as specified by the arrow in Fig. 7.2(a). Only the part near *one* wall is shown. The solid line represents the fit by Eq. (7.3), with $\xi_c = 16$ nm and $A = 0.1$.

7.4 Summary of Confined $C_4E_1+H_2O$ Mixtures

On the basis of the above results we conclude that our model predicts a qualitatively correct dependence of the mean mass fraction w_A of the $C_4E_1+H_2O$ mixture on the pore width r_h . However, the model obtains an asymptotic decay of w_A for large pores while an almost linear dependence on $1/r_h$ is found in the experiment (see Fig. 7.2). Moreover, the strong depletion of amphiphile from the porous matrix can be attributed to a high value of the water–substrate attraction strength ϵ_w^* . It is desirable to confirm this result by studying sorption from a liquid system onto a less selective surface. The concentration profile for a wide pore (Fig. 7.4), on the other hand, gives rise to a correlation length of $\xi_c = 16$ nm which is indeed long-range, so that the adsorption process for pore widths of less than 32 nm should not be confused with that occurring at a free surface. Instead, overlapping profiles imply that the composition at the center of the pore deviates significantly from the bulk (see Fig. 7.3). Nevertheless, because of the temperature-dependent interaction parameters necessary to account for the upper miscibility gap in the phase diagram, we concentrate on a rather narrow temperature range where we may safely assume this dependence to be minute.

In order to tap the full potential of our model, we turn to the system iso-butyric acid + heavy water inside a porous matrix in the next chapter. Despite of our admittedly crude assumptions (i.e., $\epsilon_{AA} = \epsilon_{AB} = 0$, $\mu \rightarrow \infty$), we are able to *tune* our model parameters in order to map the theoretical coexistence curve onto its experimental counterpart because this system exhibits a *lower* miscibility gap.

CHAPTER 8

Interpretation of SANS-Data and Structure of Confined iBA+D₂O Mixtures

We now turn our attention to a binary mixture of iso-butyric acid (iBA) and heavy water (D₂O) confined to a mesoporous controlled pore glass (CPG-10, see Fig. 7.1). The *bulk* system exhibits a lower miscibility gap qualitatively similar to our model mixture. Experimentally, the iBA+D₂O bulk mixture was thoroughly investigated by Woermann *et al.* [217, 218]. It exhibits a liquid+liquid phase separation below $T_c = 318.19$ K into iBA- and D₂O-rich liquid phases. The authors also studied the critical behavior and determined the critical exponents for such mixtures. Based upon their data [218] and additional measurements by Schemmel *et al.* [145] we adjust parameters such that the liquid+liquid coexistence curve calculated for our model matches as much as possible its experimental counterpart. In addition, by choosing appropriate values for both pore width and fluid–substrate attraction strength we study the effect of confinement on the phase behavior. Theoretical predictions are then compared with results of a small-angle-neutron-scattering study of iBA+D₂O mixtures confined to pores of CPG-10-75.

8.1 Experimental Details

Small-angle neutron scattering (SANS) is used to analyze the temperature-dependent mesoscale structure of the iBA (A) + D₂O (B) mixtures confined to CPG-10-75 pores with a mean pore size of about 10 nm (see Table 7.1). For two fixed mass fractions of iBA, $w_A = 0.25$ and $w_A = 0.54$, the mixture is filled into the pore material well above the critical temperature and with no excess liquid left outside of the pores, that is the liquid is inside the pores and no exchange process occurs. This ensures that the *mean* mass fraction across the porous matrix remains constant at the two values regardless of temperature. The SANS experiments are carried out over a temperature range from 10 °C to 70 °C. The system is equilibrated for at least 45 minutes. Details of the sample preparation and the experiment are given in [63, 145, 207].

Scattering data are analyzed by a scaling function similar to that proposed by Formisano and Teixeira [182, 183] consisting of four additive contributions:

- (i) Scattering by contrast differences between silica matrix and preferentially adsorbed film (k_G) [189]
- (ii) Scattering by contrast differences between core liquid and adsorbed layer (k_F) [189]
- (iii) Ornstein-Zernike scattering of the pore liquid characterized by diffuse composition fluctuations for high temperatures [219]
- (iv) Debye scattering by domains or structures with sharp interfaces for low temperatures [220].

Additional contributions from both Porod scattering [221] and the incoherent background are disregarded because they are negligible here [63]. Moreover, analysis of the SANS data [63] revealed that the Ornstein-Zernike term can be neglected, too at lower temperatures, while at higher temperatures the Debye term can be ignored. However, at intermediate temperatures near phase separation in the pore both terms are incorporated.

Contributions (i) and (ii) define contrast factors k_G and k_F describing the *difference* in scattering-length density between silica matrix and adsorbed layer and between adsorbed layer and core liquid, respectively (see Fig. 8.1). We adopt the following prescription to compare the measured contrast factors with those predicted by our model. The densities, ρ_{lay}^A and ρ_{lay}^B , of the first layer at the pore wall and the mean densities, ρ_{core}^A and ρ_{core}^B , associated with the remainder of the pore space are given by

$$\begin{aligned}
 \rho_{\text{lay}}^A &\equiv \frac{1}{2}(\rho_1^A + \rho_{n_z}^A) & \rho_{\text{core}}^A &\equiv \frac{1}{n_z - 2} \sum_{k=2}^{n_z-1} \rho_k^A \\
 \rho_{\text{lay}}^B &\equiv \frac{1}{2}(\rho_1^B + \rho_{n_z}^B) & \rho_{\text{core}}^B &\equiv \frac{1}{n_z - 2} \sum_{k=2}^{n_z-1} \rho_k^B,
 \end{aligned} \tag{8.1}$$

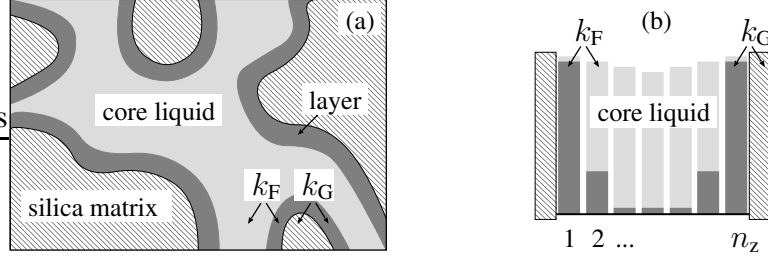


Figure 8.1: (a) Sketch of the irregular silica network of the CPG-10 material (see SEM picture in Fig. 7.1) and (b) density profile of the model slit pore, an adsorbed layer at the pore wall and the liquid in the core. The contrast factors arise from differences in the scattering length density between core liquid and layer (k_F) and between matrix and layer (k_G), respectively.

where n_z is the width of the model slit pore. Taking values of scattering-length densities Nb [222] in units of 10^{10} cm^{-2} , $Nb_A = 0.537$, $Nb_B = 6.37$, and $Nb_{\text{SiO}_2} = 3.64$, for iBA, D_2O , and SiO_2 (silica matrix), respectively, we define the contrast parameters in units of 10^{10} cm^{-2} for a given model phase by

$$\begin{aligned} k_G &\equiv |Nb_{\text{lay}} - Nb_{\text{SiO}_2}| = |0.537 \rho_{\text{lay}}^A + 6.37 \rho_{\text{lay}}^B - 3.64| \\ k_F &\equiv |Nb_{\text{core}} - Nb_{\text{lay}}| = |0.537 (\rho_{\text{core}}^A - \rho_{\text{lay}}^A) + 6.37 (\rho_{\text{core}}^B - \rho_{\text{lay}}^B)|. \end{aligned} \quad (8.2)$$

Before we turn to our results we describe in the next section how the model parameters are adjusted to model a confined mixture similar to the experimental one. We proceed in a similar manner as in the Sec. 7.1.

8.2 Determination of Model Parameters

8.2.1 Interaction Parameters

Similar to the approach described already in Chapter 7 we divide space into cubic cells of equal sizes with lattice constant ℓ . Each cell may be occupied by either iBA (A) or D_2O (B), or it may be altogether empty¹. Because iBA molecules are about five times larger than water molecules, cells occupied by water contain more molecules than those occupied by iBA. Therefore, we expect that the interaction parameters to decrease in the order $|\epsilon_{\text{BB}}| > |\epsilon_{\text{AB}}| \gg |\epsilon_{\text{AA}}|$. In the present analysis we deliberately set $\epsilon_{\text{AA}} \equiv 0$ to reduce the number of model parameters.

¹So that in principle the gas phase may appear in our model.

8.2.2 Confinement Parameters

In the experimental system water molecules are much more strongly adsorbed by the silica matrix than iBA molecules. This selectivity of the substrate is modeled according to the long-range potential of Eq. (2.27) but with $\epsilon_{\text{WA}} \equiv 0$. Thus, the iBA–substrate interaction is only repulsive.

Embracing again the concept of a hydraulic radius r_{h} to account for different pore geometries in the model and in the experiment (see Sec. 7.1.2) we set the lattice constant equal to the mean distance between molecules in an 1:1 iBA+D₂O mixture, that is $\ell = 1$ nm. From Table 7.1 we find $r_{\text{h}} = 6.8$ nm for CPG-10-75 pores, and therefore the width of the model slit pore is given by $n_z = r_{\text{h}}/\ell = 7$.

8.2.3 Thermodynamic States

Equilibrium states of the model mixture (i.e., order parameters ρ^{A} and ρ^{B}) then depend on $T^* \equiv k_{\text{B}}T/|\epsilon_{\text{BB}}|$, $\mu^* \equiv \mu/|\epsilon_{\text{BB}}|$, $\Delta\mu^* \equiv \Delta\mu/|\epsilon_{\text{BB}}|$, $\epsilon_{\text{AB}}^* = \epsilon_{\text{AB}}/\epsilon_{\text{BB}}$, and $\epsilon_{\text{W}}^* \equiv \epsilon_{\text{WB}}/|\epsilon_{\text{BB}}|$. Note that the volume densities ρ^{A} and ρ^{B} are given in units of ℓ^3 .

From Sec. 2.4.2 and Eq. (2.23) we see, on the one hand, that the mean chemical potential μ , which is a monotonic function of the pressure, couples directly to the mean density $\rho = \rho^{\text{A}} + \rho^{\text{B}}$ where

$$\rho^{\text{A}} \equiv \frac{1}{n_z} \sum_{k=1}^{n_z} \rho_k^{\text{A}}, \quad \rho^{\text{B}} \equiv \frac{1}{n_z} \sum_{k=1}^{n_z} \rho_k^{\text{B}}. \quad (8.3)$$

The incremental chemical potential $\Delta\mu$, on the other hand, couples to the composition of the mixture $\rho^{\text{A}} - \rho^{\text{B}} = \rho m$. Thus, μ and $\Delta\mu$ determine gas+liquid and liquid+liquid coexistence, respectively (see also Chapter 4). Since the experimental system is always in the liquid state, μ should be large enough (> -2.0) to guarantee that the liquid state is thermodynamically stable throughout. Moreover, varying $\Delta\mu$ allows us to fix the composition of the mixture at different T which mimics the experimental situation. We return to this issue in Sec. 8.4 where we focus on temperature quenches at constant mean concentration.

To make contact with parallel experiments we need to convert densities ρ^{A} and ρ^{B} to mass fractions by

$$w_{\text{A}} = 1 - w_{\text{B}} = \frac{1 - \alpha}{1 + \kappa + \alpha(\kappa - 1)} \quad (8.4)$$

with $\alpha = (\rho^{\text{A}} - \rho^{\text{B}})/(\rho^{\text{A}} + \rho^{\text{B}})$ and $\kappa = 0.85$ as the experimental ratio of the mass densities of iBA and D₂O.

In order to link the dimensionless model temperature T^* to that of the experimental study we use the criterion that the critical temperature of the experiment $T_{\text{c}}^{\text{exp}} = 318.19$ K [218] matches T_{c}^* characteristic of the model.

Note that our model does not permit us to capture solidification of the lattice fluid. Once the liquid state has been attained no further first-order phase transition to a solid

state arises regardless of T , μ and $\Delta\mu$. In the experimental system, however, solidification of the mixture will, of course, eventually occur if T becomes sufficiently small. To correct for this unphysical behavior of the model we introduce an offset temperature T_0 which serves to relate the temperature scale characteristic of the model to the physical one governing the experimental system. Thus, T^* is transformed into Système Internationale (SI) units by

$$T \text{ [K]} = \frac{T^*}{T_c^*} (T_c^{\text{exp}} - T_0) + T_0. \quad (8.5)$$

8.2.4 Phase Diagram of Bulk Systems

Model parameters T_0 , μ^* , and ϵ_{AB}^* are then adjusted to represent the experimental bulk phase diagram. These parameters are held constant for all calculations. Figure 8.2

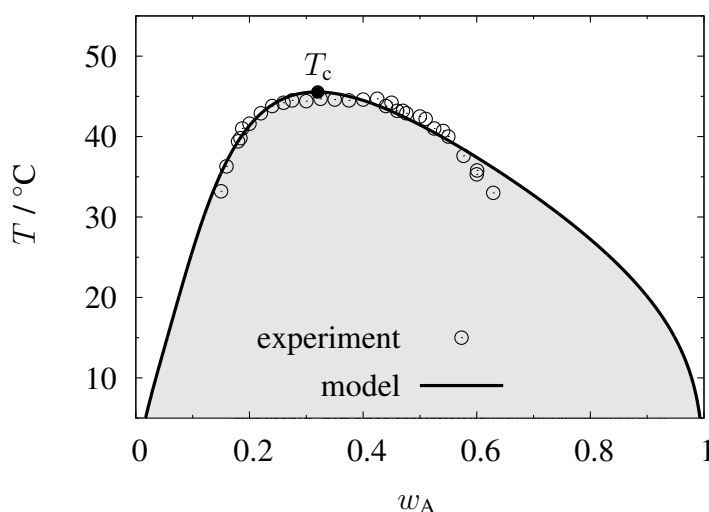


Figure 8.2: Bulk phase diagram of the system iBA+D₂O. The solid line represents the model coexistence curve whereas the open circles (○) indicate experimental values taken from [145, 218]. The two-phase region is shaded.

shows the experimental and calculated coexistence curves for $T_0 = 261 \text{ K}$ ($-12 \text{ }^\circ\text{C}$), $\mu^* = -1.05$, and $\epsilon_{AB}^* = 0.3$. The shaded area shows the two-phase region, where the mixture separates into iBA- and D₂O-rich liquid phases. The impact of μ and ϵ_{AB} on the bulk phase diagram decouples. In other words, changes in μ lead to a horizontal shift of the entire coexistence curve along the w_A -axis, whereas variations of ϵ_{AB}^* modify its curvature. We note from Fig. 8.2 that the model critical temperature, T_c , is about 0.5 K higher than the experimental value taking into account that

$$\Delta w_A \propto (T_c - T)^\beta \quad (8.6)$$

is governed by different values for the critical exponent. For the model $\beta = 0.5$ as expected at mean-field level [162], whereas $\beta = 0.330$ [218] for the experimental system.

8.3 Phase Diagram of Confined Systems

Consider now the iBA+D₂O mixture confined to the mesoporous matrix. As reasoned by the concept of the hydraulic radius before, in our calculations CPG-10-75 is represented by an 3.4 nm slit pore. Taking the parameter set adjusted to mimic the bulk phase diagram, that is $T_0 = 261$ K, $\mu^* = -1.05$, and $\epsilon_{AB}^* = 0.3$, we are left with only one remaining model parameter ϵ_W^* , measuring the strength of water–substrate attraction. As argued in Chapter 7, ϵ_W^* should be somewhere in the range of 1 and 5 to avoid unrealistically weak or strong adsorption. Here, we choose $\epsilon_W^* = 3.0$ for

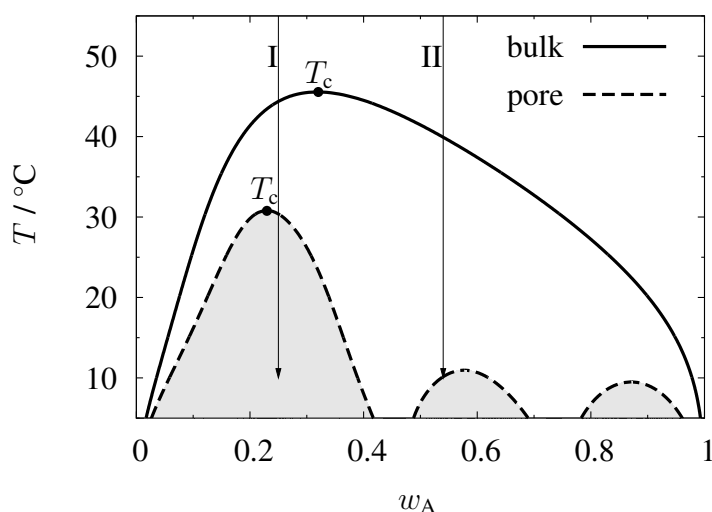


Figure 8.3: Phase diagram of the model mixture for the bulk system (—) and confined in the slit pore (---) with $\epsilon_W^* = 3.0$. Two-phase region of the confined mixture is shaded. Dots (●) represent critical points. Paths I and II display temperature quenches at two fixed compositions $w_A = 0.25$ and $w_A = 0.54$, respectively.

which the model coexistence curves are shown in Fig. 8.3. The shaded areas refer to the respective two-phase regions of the confined system. The remarkable topological change of the phase diagram relative to that of the bulk system is caused by both confinement and selectivity of the porous matrix (i.e., energetic preference to adsorb water). As expected, the critical temperature of the pore fluid is shifted downward. The critical composition moves toward the water-rich side because of the selective character of the substrates. In addition to the liquid+liquid coexistence curve the confined fluid exhibits two more less-pronounced two-phase regions at larger w_A and lower T .

Here, the coexisting phases are water-rich films of one or two layers (e.g. see Figs. 8.1(b) or 8.5(d1), respectively) which are distinguishable only at lower temperatures. The existence of such layer phases is a signature of homogenous solid surfaces. Such phases are unlikely to exist in systems with rough or chemically heterogeneous surfaces [29, 123, 131, 155].

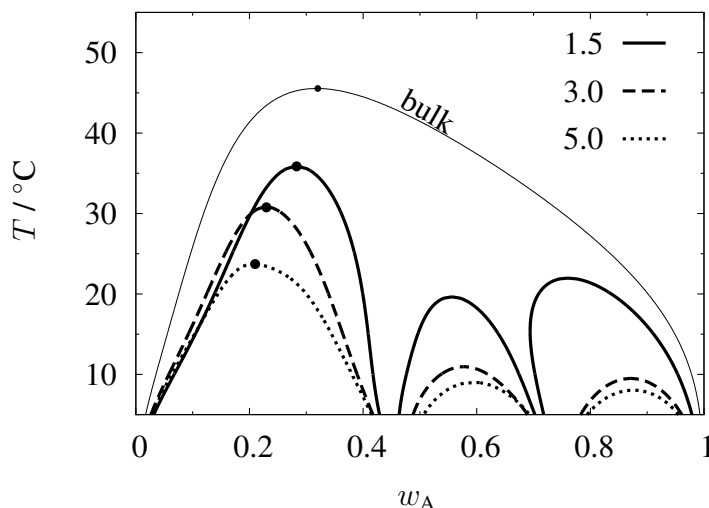


Figure 8.4: Phase diagram of the mixture for the model slit pore for different water–substrate attractions ϵ_{W}^* as given in the graph. Dots (•) indicate critical points.

As pointed out above, we are still left with some ambiguity as far as the precise value of ϵ_{W}^* is concerned. Therefore, we investigate the impact of ϵ_{W}^* on the phase diagram. Results plotted in Fig. 8.4 reveal that the larger the selectivity of the substrates, the lower are critical temperature and critical iBA-concentration. Moreover, film-phase transitions are increasingly inhibited, that is their two-phase region becomes narrower with increasing ϵ_{W}^* and coexistence lines shift downward in temperature (see Fig. 8.4). This is because for strongly adsorbing walls almost all water molecules stick to the solid surfaces.

8.4 Structure and Contrast Factors

We now investigate mixtures as a function of temperature at constant composition. Specifically, we consider paths I and II indicated in Fig. 8.3 corresponding to $w_{\text{A}} = 0.25$ and $w_{\text{A}} = 0.54$, respectively, for which SANS measurements were carried out by Schemmel and Findenegg [63].

In order to achieve the stable phase of constant mass fraction w_{A} , we have to distinguish between two scenarios. If the state is in the one-phase region (outside the shaded

regions in Fig. 8.3), on the one hand, the incremental chemical potential $\Delta\mu$ couples to and varies monotonically with w_A as described in Sec. 8.2. Therefore, $\Delta\mu$ has to be varied until the constant value of w_A is reached for each temperature.

On the other hand, for states pertaining to the liquid+liquid coexistence region, the mixture separates into two stable phases (labeled (1) and (2)) at fixed T with mean composition $w_A^{(1)} < w_A < w_A^{(2)}$. The phase coexistence determines $\Delta\mu$. The condition of constant mass fraction across all pores must then satisfy the expression

$$x w_A^{(1)} + (1 - x) w_A^{(2)} = w_A \quad (8.7)$$

where x is the mole fraction of phase (1). That is, the portion of the mesoporous matrix which is occupied by phase (1) is x , whereas the remainder pore space (i.e., $1 - x$) is occupied by phase (2). From Eq. (8.7) we can calculate the relative amounts of phase (1) and (2) across the porous matrix. Since the contrast parameters of the two coexistent phases are assumed to be additive, the *mean* contrast parameters may be cast as

$$\begin{aligned} k_G &= x k_G^{(1)} + (1 - x) k_G^{(2)} \\ k_F &= x k_F^{(1)} + (1 - x) k_F^{(2)}. \end{aligned} \quad (8.8)$$

8.4.1 D₂O-rich Phases

We begin with an investigation of the confined iBA+D₂O mixture along path I in Fig. 8.3 ($w_A = 0.25$). For this path SANS data [63] reveal that the scattering intensity is *independent* of temperature over the experimental range (10 °C - 70 °C). This implies

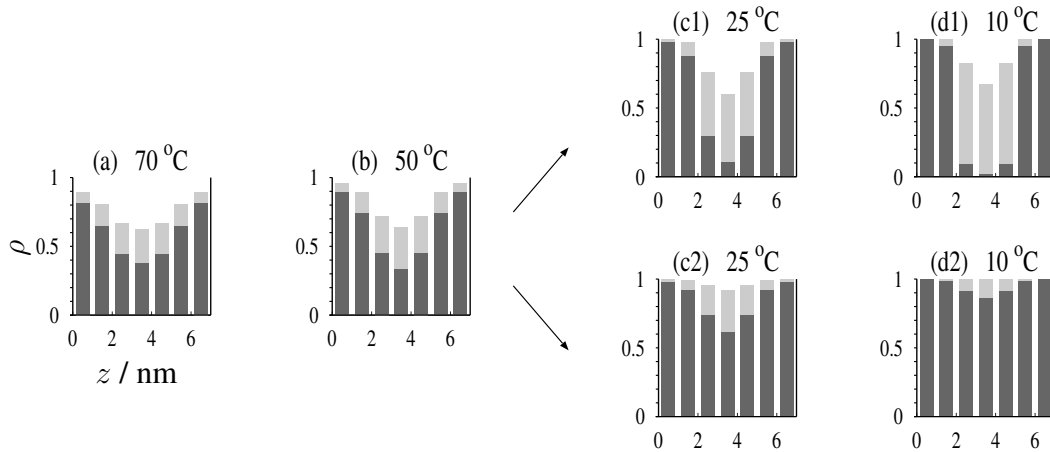


Figure 8.5: Volume density profiles at constant $w_A = 0.25$ at temperatures given in the graphs. The single phase (a) and (b) separates into two phases below $T \simeq 30$ °C (c1,c2) and (d1,d2). Dark fields represent D₂O, bright fields iBA fractions.

that the two contrast factors k_G and k_F remain constant, which seems surprising in view of the fact that the mixture phase-separates in this temperature range. According to path I in Fig. 8.3 the confined mixture separates into two phases for $T \lesssim 30$ °C (shaded area). Figures 8.5(a) and (b) illustrate the associated variation of the local

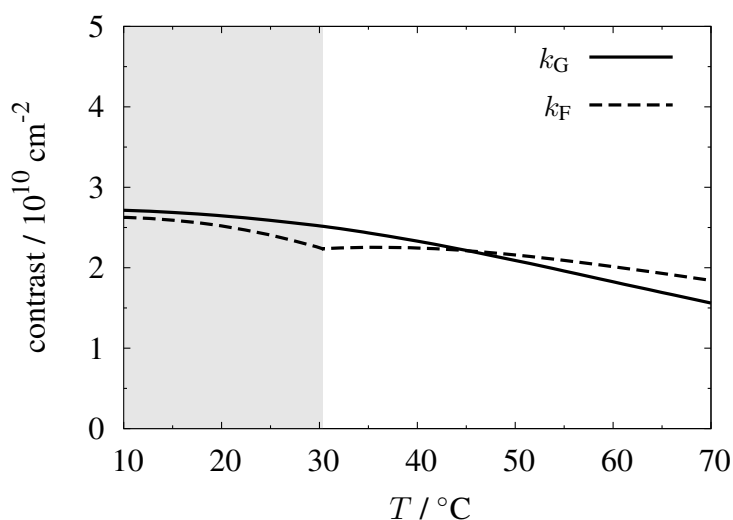


Figure 8.6: Model contrasts k_G and k_F calculated from Eqs. (8.2), (8.7), and (8.8) as a function of temperature at constant $w_A = 0.25$. The two-phase region is shaded.

densities in the one-phase region at $T = 70$ °C and $T = 50$ °C; graphs (c) and (d), on the other hand, display coexisting phases at $T = 25$ °C and $T = 10$ °C, respectively. From Eqs. (8.2), (8.7), and (8.8) we compute the contrast factors k_G and k_F . Plots in Fig. 8.6 show that neither k_G nor k_F exhibits a pronounced temperature-dependence which supports the results of the experiment (i.e., constant k_G and k_F).

The weak temperature-dependence can be rationalized as follows. Since water is the major component ($w_B = 1 - w_A = 0.75$) and is strongly adsorbed by the substrate, the first layer consists of almost pure water at all temperatures (see Fig. 8.5) leading to nearly temperature-independent values of ρ_{lay}^A and ρ_{lay}^B . Therefore, k_G and k_F (see Fig. 8.1) are expected to depend only weakly on T . Consequently, we conclude that k_G and k_F are not suitable for analyzing and characterizing the structure of phases where the preferentially adsorbed component (here, water) is also the one dominating the composition of the mixture.

8.4.2 iBA-rich Phases

We now focus on the confined mixture along path II shown in Fig. 8.3. In the experimental range (10 °C - 70 °C) the mixture remains in the one-phase region regardless of T where now iBA is the dominating component ($w_A = 0.54$). Figure 8.7 illustrates

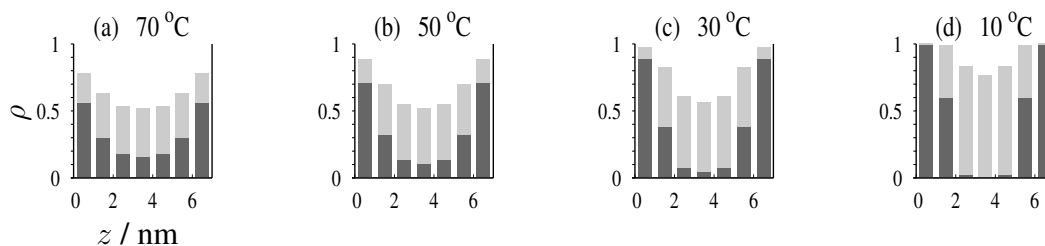


Figure 8.7: As Fig. 8.5, but for $w_A = 0.54$ (see path II in Fig. 8.3).

density profiles for four representative temperatures. At low temperatures, that is for $T = 10\text{ °C}$ to $T = 30\text{ °C}$, almost all water molecules accumulate in the first and second layer, whereas the core liquid is almost depleted of water (Figs. 8.7(d) and (c)). Therefore, over this temperature range the two contrast factors attain high values as Fig. 8.8 demonstrates.

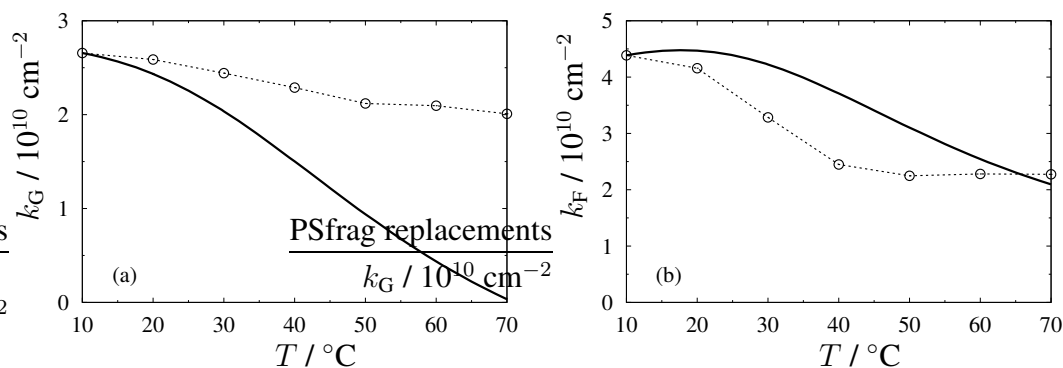


Figure 8.8: Contrast parameters (a) k_G and (b) k_F as a function of temperature obtained from the model calculation with Eq. (8.2) (—) and from the SANS data (\circ) at constant $w_A = 0.54$. The experimental data are scaled arbitrary as described in the text.

This changes significantly at higher temperatures. Profiles in Figs. 8.7(a) and (b) (i.e., $T = 70\text{ °C}$ to 50 °C) exhibit more gradual concentration changes from the pore walls into the core region, whereas the interface between layer and core liquid becomes more diffuse. This points to water enrichment of the core liquid and causes k_G and k_F to decrease with increasing temperature (see Fig. 8.8). Since experimentally the contrast factors are undetermined up to a temperature-independent scaling factor [63], we adjust them so that the values at $T = 10\text{ °C}$ coincide with the corresponding values predicted by the model (see Fig. 8.8). Therefore, although we cannot compare the absolute values of k_G and k_F , we see from Fig. 8.8 that the dependence of k_G and k_F on temperature for the model agrees qualitatively with that of the experiment.

The results of the model calculation are further supported by the corresponding SANS measurements. At low temperatures $T \lesssim 30\text{ °C}$ the SANS data suggest that

domains or structures are formed exhibiting sharp interfaces in between. These structures corresponding to the Debye scattering (see Sec. 8.1) have sizes of about 3–4 nm which are about half of the pore size (6.8 nm). For these temperatures the model also predicts a sharp interface between water-rich layer and iBA-enriched pore liquid as can be seen in Figs. 8.7(c) and (d). Thus, a surface-induced structure may be considered as a microscopic phase segregation² into a sandwich-type structure [47, 69, 70]. The iBA-enriched middle layer (core liquid) occupies about half of the pore. Thus, our calculation reproduces the experimental findings. For higher temperatures where the Ornstein-Zernike scattering dominates the experimental system (see Sec. 8.1), this segregation becomes more diffuse. Inspecting of Figs. 8.7(a) and (b) reveals that the density profiles also exhibit a broad and smooth crossing from the layer to the core liquid.

8.5 Summary of Confined iBA+D₂O Mixtures

Confined asymmetric mixtures of iBA+D₂O in which the water is strongly preferred by the CPG-10-75 matrix generally exhibit a rich phase behavior in the bulk as well as in mesoporous solid matrices. The critical point of the bulk system (Fig. 8.2) is on the water-rich side of the phase diagram reflecting the fact that the water–water attraction exceeds that between iBA molecules. Figure 8.3 shows that confinement leads to a substantial depression of the critical temperature and to a shift of the critical composition towards the preferred component D₂O in accord with earlier studies [64–66, 68, 77] (see also Chapter 6). In addition, preference of the minor component triggers surface-induced film-phase transitions [32, 47] apparent in Fig. 8.3. However, by virtue of its nature the lattice model overestimates these transitions. Fortunately, they are irrelevant in the present context.

Considering temperature quenches at constant mean mass fraction $w_A = 0.25$ (see path I in Fig. 8.3), we observe from Fig. 8.5 that the system phase-separates below $T \lesssim 30$ °C. Even though our mean-field model with constant pore width is unable to *localize* the two coexistent phases inside the porous network, in the experiment the two are distributed across the CPG-10 matrix. We surmise that the iBA-rich phase represented by Figs. 8.5(c1) and (d1) is in rather wide pores or in the pore junctions, whereas the D₂O-rich phase of Figs. 8.5(c2) and (d2) occupies the smaller pore spaces as suggested by Monette *et al.* [70] and Kohonen *et al.* [184]. Another scenario applies to pore matrices with long homogenous walls where according to earlier investigations [47, 69, 70] the phase separation leads to capsule-like structures (tube-shaped iBA-rich phase and water-rich bubbles in between). The SANS measurements [63] for $w_A = 0.25$ showed that the contrast factors k_G and k_F are constant in the temperature range 10 – 70 °C. The model calculations of Fig. 8.6 support these findings which are

²Note, that the system is inside the one-phase region.

shown here to be a direct consequence of the confinement-induced liquid-liquid phase separation.

We also investigate an amphiphile-rich confined fluid along the path labeled II in Fig. 8.3. In this case and contrary to the water-rich phases a significant temperature-dependence of the SANS contrast parameters is observed both experimentally and theoretically. Although the mixture remains in the one-phase region regardless of T , we observe a microscopic phase segregation for $T \lesssim 30$ °C upon which an iBA-rich core region forms. It occupies about half of the pore volume (Figs. 8.7(c) and (d)). The SANS analysis also gives rise to structures of sizes 3 – 4 nm which are about half of the hydraulic radius of 6.8 nm (Table 7.1) in accord with the theoretical results. Comparing Figs. 8.8(a) and (b) we find good agreement between model and experimental contrast factors. Since water is the minor component ($w_A = 0.54$), a first-order phase transition would lead to discontinuities in k_G and k_F . This is not apparent in the experimental curves in Fig. 8.8 and therefore, the mixture remains in the one-phase region in complete agreement with the model prediction.

CHAPTER 9

Conclusion

Summary and Closing Remarks

In the present thesis we investigate phase behavior and structure of binary mixtures of components A and B in bulk, in contact with a single solid substrate, and confined between two parallel substrates (slit-pore geometry). The substrates are homogenous and planar but can be selective for one of the two components and are placed perpendicular to the z -axis. The thesis is divided into three parts. Part I is given to a description of the model and the method used throughout our investigations, whereas the second Part presents main results of our theoretical studies. In Part III we compare theoretical predictions with experimental findings for confined binary mixtures.

Part I

Chapter 2 is dedicated to the introduction of a model to determine the phase behavior of classical binary mixtures. Such mixtures consist of molecules of species A and B. The basic concept of the model is the combination of a lattice-fluid model and a mean-field approximation in the grand canonical ensemble. We employ the lattice model [80]

to greatly reduce the dimensionality of the configuration space. It accounts solely for nearest-neighbor interactions between the fluid molecules that are modeled according to square-well potentials. The depths of the attractive wells are ϵ_{AA} and ϵ_{BB} for pairs of like molecules, respectively, and ϵ_{AB} determines the attraction strength between unlike molecules. The mean-field approximation, which we apply only to intermolecular correlations in the x - y plane, is reasonable in view of the translational invariance of system properties in that plane. This is a direct consequence of the symmetry of the external field representing the confining substrates, that is the fluid–substrate potential depends only on the z -coordinate of a molecule. We derive a *closed* expression for the grand potential density which is subsequently minimized numerically with respect to the local densities of both components to obtain thermodynamically stable phases for a given set of model parameters and thermodynamic variables.

This gives rise to one of the greatest advantages of the model, namely it permits to compute entire phase diagrams with comparably little computational effort even for a rather highly dimensional model parameter space. This aspect is particularly important in the context of this work where we have to “scan” the wide parameter space for interesting features and characteristics of the phase behavior of binary mixtures. The derivation of the grand potential and relevant thermodynamic quantities is detailed in Chapter 2. Numerical aspects are further discussed in Chapter 3.

Part II

Bulk. In Chapter 4 we present results of our study of binary bulk mixtures. To reduce the dimensionality of the parameter space, we restrict this study to binary mixtures for which $\epsilon_{AA} = \epsilon_{BB}$. Thus, mixture properties come about only by varying the attraction strength of unlike molecules, $\epsilon_{AB}^* = \epsilon_{AB}/\epsilon_{AA}$, in a way to either promote mixing ($\epsilon_{AB}^* \geq 1$) or demixing ($\epsilon_{AB}^* \leq 1$). We determine essentially three different generic types of phase diagrams. According to Gibbs’ phase rule (see Sec. 2.4.3), these phase diagrams are distinctly different from those for one-component systems, because for binary mixtures two-phase coexistence is represented by surfaces in μ - $\Delta\mu$ - T space in which critical and triple points form entire lines.

For type-I mixtures, that is for $1 > \epsilon_{AB}^* > 0.58$, the phase diagram is dominated by gas+liquid coexistence (grey surface in Fig. 4.3(a)) whereas demixing transitions (blue face) are found only at low temperatures and for large densities. All three phases, namely gas, A- and B-rich liquids, also coexist along a triple line ending at the critical end point (cep) in accord with earlier studies by Dietrich and Schick (Fig. 3 in [32]) and van Konynenburg and Scott [2]. Results for the corresponding *symmetric* mixture are obtained when setting $\Delta\mu = 0$ for which the well-known bulk phase diagrams are plotted in Fig. 4.9. Qualitatively the same phase behavior of symmetric type-I mixtures was observed by Wilding *et al.* (Fig. 2(a) in [12]) and Kahl *et al.* [14].

For intermediate values of $0.58 \geq \epsilon_{AB}^* > 0.4$ the mixture is of type II where now a mixed liquid+demixed liquid transition arises (see Fig. 4.5). The mixed liquid may

also coexist with a gas phase. As can be seen in Fig. 4.5, all four phases coexist at a single quadruple point which is an unique feature of this type of mixture. For higher temperatures the quadruple point bifurcates into three independent triple lines each terminating at a tricritical point. Such a behavior has not been reported in the literature before. Figure 4.10 displays the corresponding phase diagram of the symmetric mixture of type II which is again obtained by a $\Delta\mu = 0$ -cut through the general phase diagram of Fig. 4.5. The resulting phase diagram again agrees with the one of Wilding *et al.* (Fig. 2(c) in [12]) who observe this type for $0.72 > \epsilon_{AB}^* \geq 0.605$. Note, that the phase diagram of the symmetric mixture exhibits only one tricritical point, as the other two are located at $\Delta\mu \neq 0$.

Type-III mixtures are distinct in that they exhibit a strong tendency to demix. As Fig. 4.7 shows, the triple line of coexisting gas, A- and B-rich liquid phases ends at a single tricritical point. The mixed liquid phase is suppressed because of the rather small values of $0.4 \geq \epsilon_{AB}^* \geq 0$. This is further illustrated by plots for the symmetric type-III mixture in Fig. 4.11 where the gas+mixed liquid critical point is now metastable. Again, our results for the symmetric mixture support the earlier findings of Wilding *et al.* (Fig. 2(d) in [12]) for a different model system.

The qualitative agreement between our study of symmetric mixtures and those of Wilding *et al.* [12] and Kahl *et al.* [14] based upon off-lattice models allows to conclude that the phase diagrams of types I-III are indeed generic, that is model-independent. Chapter 4 also discuss the three obtained types in view of the classification scheme of van Konynenburg and Scott [2] who employed the van der Waals equation for binary mixtures. It is noteworthy that qualitatively equivalent phase diagrams are obtained for dipolar fluids [101, 102, 104] and classical Heisenberg systems [103, 105–107]. This is plausible since the lattice-fluid is equivalent to the Ising spin model [80]. However, we point out that full phase diagrams of types I-III involving the entire thermodynamic state space, that is μ , $\Delta\mu$, and T , have not been published elsewhere but are presented here for the first time.

Another question concerns the *order* of the demixing transition when the mixed liquid is isothermally compressed until it spontaneously decomposes [15]. We find first-order demixing for intermediate temperatures for mixtures of type II and III as indicated by the arrow in Figs. 4.6(c) and 4.8(b,c), respectively. For higher temperatures, this transition becomes second-order. For mixtures of type I, on the other hand, demixed liquids are only stable for low temperatures and the transition from mixed to demixed liquids is always second-order (Fig. 4.4(c)).

Wetting of Symmetric Mixtures. In Chapter 5 we study wetting of nonselective planar homogenous substrates by symmetric binary mixtures. The strength of the *short-range* attraction is governed by a single parameter ϵ_W . The lattice-fluid model is adequate to capture some of the major characteristics of systems, that is layering transitions [29, 30]. However, the discrete nature of the model favors layer-like structures more strongly than in more realistic continuous models [28]. In accord with earlier results of Ebner [24, 163] and Ball and Evans [29] for pure fluids, we find nei-

ther roughening nor prewetting transitions because of the mean-field approximation on which our approach is based [28].

Nevertheless, the model exhibits a wetting temperature T_w such that we observe complete wetting for $T \geq T_w$, that is an infinite number of layer transitions eventually causing a macroscopically thick film to form close to bulk coexistence. Below T_w , the fluid wets the substrate only partially. Moreover, we can discriminate between mixed and demixed films. Our main results can be summarized as follows:

- (i) The wetting temperature goes to zero for sufficiently attractive substrates (i.e., $\epsilon_w/\epsilon_{ff} > 1$) in accord with simple phenomenological considerations (Figs. 5.5, 5.7 and 5.13(b)).
- (ii) We always observe complete wetting according to Cahn's argument [16] at least for temperatures just below the bulk gas+liquid (tri)critical point (Figs. 5.5, 5.8, and 5.11).
- (iii) For mixtures of types I-III all *mixed* films decompose at sufficiently low temperatures, which are the lower the thinner the film is. The transition from mixed to demixed films may be of either first- or second-order. The latter arises at surface λ -lines. However, the layering transitions from $n - 1$ to n layers remain first-order and become critical at $T_{lc}(n)$ (e.g. Fig. 5.10) in accord with earlier studies [29, 30].
- (iv) Complete wetting of the substrate by *mixed* films occurs only for mixtures of type I for $T > T_{cep}$ (Fig. 5.10) and for mixtures of type II for $T > T_{quad}$ (Fig. 5.11), respectively. Below these temperatures demixed films wet the substrate completely. For mixtures of type III complete wetting involves always demixed films (Fig. 5.13).

Results of item (iii) are in accord with studies of Martinez *et al.* [79, 175] who analyzed the behavior of confined binary mixtures within the scope of a continuous model. It is noteworthy, that the adsorbed film phases exhibit a complex phase behavior similar to the bulk systems including surface quadruple points, critical end and tricritical points as well as triple lines. Moreover, surface critical points $T_{lc}(n)$ of the layering transitions converge to the bulk (tri)critical point T_c for $n \rightarrow \infty$ (Figs. 5.10 or 5.13). Therefore, the roughening transition [28, 30] coincides with T_c thereby precluding prewetting on the one hand and is an unrealistic feature of our mean-field model on the other hand.

Since complete wetting of *mixed* films (item (iv)) is not possible for mixtures of neither type III, type II (if $T < T_{cep}$) nor type I (if $T < T_{quad}$), the surface λ -line separating mixed and demixed films must meet the bulk tricritical point, quadruple point, or critical end point, respectively, in order to observe complete wetting of *demixed* films (see Figs. 5.11(c) and 5.13(b)).

Confined Symmetric Mixtures. In the context of confinement, we study the phase behavior of symmetric binary mixtures between two planar, homogenous, nonselective solid substrates in Chapter 6. The degree of confinement is characterized by the pore width n_z and the strength of the *short-range* fluid–substrate attraction, ϵ_w . For *all* types of mixtures, we observe four general features with *increasing* degree of confinement (i.e., larger ϵ_w and smaller n_z):

- (i) The gas+liquid (mixed or demixed) critical point shifts toward lower temperatures (Fig. 6.6) and higher densities (Figs. 6.1, 6.3, and 6.4).
- (ii) Capillary condensation of the gas phase, that is the gas+liquid (mixed or demixed) coexistence curve moves to lower chemical potentials (Figs. 6.1 and 6.3).
- (iii) Liquid+liquid critical points (λ -line) also shift toward lower temperatures and larger densities (Figs. 6.1(b), 6.3(b), and 6.4).
- (iv) The type of mixtures may change from I to II, from II to III (Fig. 6.3), or from III to a novel type which has no counterpart in the bulk (Fig. 6.5).

The first two items are also known for pure fluids (e.g. [52]) although in the present context the gas may condense and form a demixed liquid. Since the substrates favor the liquid state (i.e., $\epsilon_w > 0$), the gas+liquid coexistence curve moves to larger densities.

The depression of the liquid+liquid critical temperature (item (iii)) agrees with previous studies of Gubbins *et al.* [65, 67, 68] and Greberg and Patey [66]. Though the substrates are nonselective but attractive, the coexisting A- and B-rich liquids are denser for larger degrees of confinement.

The perhaps most significant result of item (iv) concerns confinement-induced changes in the type of mixtures, as can be seen in Fig. 6.3, where the type-II mixture ($n_z = 12$) is converted into type I for smaller pores ($n_z = 6$). The change in *topology* of the phase diagram may cause a change in *morphology* of a confined mixture while holding thermodynamic state variables fixed. For example, for a given thermodynamic state for which the bulk system is in the gas phase, Fig. 6.8 indicates that this gas phase may condense to a mixed liquid at $n_z = 16$ which eventually decomposes in narrow pores ($n_z < 8$). This may have important repercussions for experimental systems. For example, confinement-induced demixing may be relevant for the separation of mixed gases or liquids.

Another interesting feature involves type-III mixtures which may completely change their phase behavior if substrate attraction is sufficiently strong (Fig. 6.5). For instance, as Fig. 6.5 reveals the gas+demixed liquid tricritical point becomes a true critical point with increasing substrate attraction strength where now the dilute phase is also demixed because the surface λ -line detaches from the coexistence line. Such an effect was also reported not only for binary mixtures [79] but also for $^3\text{He}+^4\text{He}$ mixtures confined to aerogel [121, 122].

Part III

Confined C₄E₁+H₂O Mixtures. In Chapter 7, we model liquid C₄E₁+H₂O mixtures confined to controlled-pore glass matrices (CPG-10) of different pore widths (see Table 7.1). These systems are studied experimentally by Rother and Findenegg [62]. The mean size of the molecules together with the concept of a hydraulic radius r_h , which accounts for the difference in pore geometry, are used to convert the pore widths of the CPG-10 materials to that of the model slit pore. The bulk system exhibits an upper miscibility gap implying strongly temperature-dependent interactions. Therefore, we focus on a small temperature range where this dependence is expected to be rather weak. Since water–water (ϵ_{BB}) and water–substrate (ϵ_{WB}) interaction strengths dominate, we assume all other amphiphile-related interactions to be repulsive. Thus, the ratio $\epsilon_W^* = \epsilon_{WB}/\epsilon_{BB}$ is the only model parameter remaining. In both, experiment and model, two thermodynamic states are chosen such that the amphiphile-rich phase at bulk liquid+liquid coexistence assumes mass fractions $w_A = 0.4$ and $w_A = 0.5$, respectively.

Similar to the confined system in the experiment, we find that the less favored amphiphile is strongly depleted from pore space as can be seen in Fig. 7.2. This can be attributed to relatively large values of ϵ_W^* . Depletion of amphiphile is the more pronounced the smaller the pore is and the more selective the substrates are. However, the experiment suggests a complete removal of the amphiphile for the smallest pore (CPG-10-75) which disagrees with the slow asymptotic decay of w_A for smaller pore widths in the model (Fig. 7.2).

A more detailed understanding of the strong adsorption of water by the substrates is gained by inspecting the concentration profile for a wide model pore displayed in Fig. 7.4. A fit of a scaling function proposed by Peliti and Leibler [34, 216] for the decay of the water adsorption gives a long-range correlation length of $\xi_c = 16$ nm which is in the range of the experimentally estimated film thickness for the largest pore (CPG-10-500) of 14.2 nm [62]. However, the two values deviate from each other. This prompts us to conclude that the estimate from experimental data is not sufficient.

Confined iBA+D₂O Mixtures. Experimentally, the binary iso-butyric acid (iBA) + heavy water (D₂O) mixture inside a porous matrix of CPG-10-75 ($r_h = 6.8$ nm, see Table 7.1) was analyzed by SANS measurements of Schemmel and Findenegg [63] within a temperature range of 10 – 70 °C. The liquid iBA+D₂O system exhibits a lower miscibility gap and is therefore amenable to theoretical investigations based upon our present model. Model parameters are adjusted so that the theoretical liquid+liquid coexistence curve in the bulk matches its experimental counterpart to a maximum extent (Fig. 8.2). By choosing appropriate values of the attraction strength between D₂O and the substrates, we study the influence of confinement on phase behavior and local structure of the mixture.

A key feature is a substantial confinement-induced depression of the critical temperature (see Fig. 8.3) in accord with earlier studies [52, 66, 77]. This is caused by

the pore width which serves to cut off concentration fluctuations. Confinement also leads to a shift of the critical mass fraction (Fig. 8.3) to the water-rich side, since the water is energetically favored by the substrate [64, 68]. The two effects become more pronounced for stronger matrix selectivity as Fig. 8.4 displays. Additional film phases involving water-rich mono- and double-layers are found on the iBA-rich side at low temperatures (see Figs. 8.3 and 8.4). However, these phases may be overemphasized by our model (see above) but are irrelevant in the present context anyway.

Finally, the structure of a water-rich and an iBA-rich phase with constant *mean* mass fractions $w_A = 0.25$ and $w_A = 0.54$, respectively, are analyzed for temperatures in the range 10 – 70 °C (see paths I and II in Fig. 8.3). For $w_A = 0.25$ (path I), density profiles plotted in Fig. 8.5 reveal a phase separation for $T \lesssim 30$ °C (see also Fig. 8.3). Assuming a simple relation between calculated local densities and contrast factors k_G and k_F (Fig. 8.1), we find a weak temperature-dependence of k_G and k_F (Fig. 8.6). The SANS measurements [63] for $w_A = 0.25$ also show that k_G and k_F remain constant in the range 10 – 70 °C in accord with our calculations.

For $w_A = 0.54$, the mixture remains in the one-phase region regardless of the temperature (path II in Fig. 8.3). However, Fig. 8.7 shows density profiles implying a strong temperature-dependence of the local structure. We observe a sandwich-like microscopic phase segregation for $T \lesssim 30$ °C where almost the entire amount of water is adsorbed by the substrates (Figs. 8.7(c) and (d)). The iBA-enriched core liquid has a thickness of about half the pore width in accord with the experiments (Debye scattering) [63]. For temperatures above 30 °C, on the other hand, the sharp segregation becomes more diffuse corresponding to water-enrichment in the core region (Figs. 8.7(a) and (b)). Comparing the contrast factors of model and experiment in Fig. 8.8, we find good qualitative agreement. Since the experimental curves of k_G and k_F in Fig. 8.8 are smooth, we conclude that the system does not exhibit a first-order phase separation according to the prediction of our calculations. However, as the water is the minor component, the graph of k_G shows a pronounced adsorption of water even for high temperatures, thus supporting our notion that water is strongly favored by the CPG-10 matrix.

Prospects

In this thesis we introduce a model of binary mixtures which turns out to be a very powerful tool for studying the phase behavior of mixtures in bulk, near solid substrates, and in confinement. However, since our model is based on the discretization of the configurational space (lattice-fluid) it would be desirable to compare our results with other off-lattice or continuous models that are frequently employed in density functional theory [223], integral equations [111, 224], or Monte-Carlo simulations [146]. Because of the good agreement of our results with those obtained by the continuous models of Wilding *et al.* [12, 13, 50], Kahl *et al.* [14, 77], and Martinez *et al.* [79, 147, 175] we expect the lattice-fluid model to be qualitatively quite reasonable. On the other hand,

the mean-field approximation, which basically neglects fluctuations in the x - y plane, also leads to deviations from exact models. Especially, one expects entropic contributions to be somewhat underestimated due to the missing fluctuations in composition and density. Sommerfeld [225], who compared results of mean-field and Monte-Carlo methods, indeed observed quantitative deviations between the two but only near criticality. However, the author pointed out, that major features of the phase diagram are quantitatively captured by the mean-field approach.

In this thesis we analyze the bulk phase behavior of symmetric binary mixtures under the constraint $\epsilon_{AA} = \epsilon_{BB}$. Although the results give a comprehensive picture of the complex phase behavior of such systems, the question arises how this behavior will change in the more general case where $\epsilon_{AA} \neq \epsilon_{BB}$. Since the model employed in this work can readily account for this symmetry break a study focusing on such bulk mixtures is presently under way, but goes beyond the scope of this thesis.

Another important question, which the present thesis also does not address, is the wetting of selective solid substrates by asymmetric mixtures. It would be interesting to analyze how the character of the adsorbed film phases responds to selective adsorbents. This field was partly examined in the work of Silbermann *et al.* [51]. Additionally, one could imagine to introduce long-range fluid–substrate potentials which account for somewhat more realistic interactions. Here we apply these kinds of potentials to model confined binary mixtures in experiments (see Part III of this thesis).

Because of the good agreement between our model predictions and experimental data (see Part III) it seems worthwhile to apply the present model to other experimental systems in order to tap its full potential and stimulate and support their interpretation.

Bibliography

- [1] M. Thommes and G. H. Findenegg. *Pore condensation and critical-point shift of a fluid in controlled-pore glass*. *Langmuir* **10**(11): 4270–4277 (1994).
- [2] P. H. van Konynenburg and R. L. Scott. *Critical lines and phase equilibria in binary van der Waals mixtures*. *Philos. Trans. R. Soc. London, Ser. A* **298**: 495–540 (1980).
- [3] J. D. van der Waals. *Molekulartheorie eines Körpers, der aus zwei verschiedenen Stoffen besteht*. *Z. Phys. Chem.* **5**: 133–173 (1890).
- [4] D. Furman and R. B. Griffiths. *Global phase diagram for a van der Waals model of a binary mixture*. *Phys. Rev. A* **17**(3): 1139–1148 (1978).
- [5] U. K. Deiters and I. L. Pegg. *Systematic investigation of the phase behavior in binary mixtures. I. Calculations based on the Redlich-Kwong equation*. *J. Chem. Phys.* **90**(11): 6632–6641 (1989).
- [6] T. Kraska and U. K. Deiters. *Systematic investigations of the phase behavior in binary fluid mixtures. II. Calculations based on the Carnahan-Starling-Redlich-Kwong equation of state*. *J. Chem. Phys.* **96**(1): 539–547 (1992).
- [7] M. Keskin, M. Gencaslan, and P. H. E. Meijer. *Evaluation and comparison of critical lines for various models of gas-liquid binary systems*. *J. Stat. Phys.*

- 66(3/4): 885–896 (1992).
- [8] P. H. E. Meijer. *The van der Waals equation of state around the van der Laar point*. J. Chem. Phys. **90**(1): 448–456 (1989).
- [9] N. B. Wilding. *Coexistence curve singularities at critical end points*. Phys. Rev. Lett. **78**: 1488–1491 (1997).
- [10] N. B. Wilding. *Critical end point behavior in a binary fluid mixture*. Phys. Rev. E **55**(6): 6624–6631 (1997).
- [11] N. B. Wilding and P. Nielaba. *Tricritical universality in a two-dimensional spin fluid*. Phys. Rev. E **53**(1): 926–934 (1996).
- [12] N. B. Wilding, F. Schmid, and P. Nielaba. *Liquid-vapor behavior of a symmetrical binary fluid mixture*. Phys. Rev. E **58**(2): 2201–2212 (1998).
- [13] N. B. Wilding. *Continuous demixing at liquid-vapor coexistence in a symmetrical binary fluid mixture*. Phys. Rev. E **67**: 052 503 (2003).
- [14] G. Kahl, E. Schöll-Paschinger, and A. Lang. *Phase transitions and critical behaviour of binary liquid mixtures*. Chemical Monthly **132**(11): 1413–1432 (2001).
- [15] O. Antonevych, F. Forstmann, and E. Diaz-Herrera. *Phase diagram of symmetric binary fluid mixtures: First-order or second-order demixing*. Phys. Rev. E **65**: 061 504 (2002).
- [16] J. W. Cahn. *Critical point wetting*. J. Chem. Phys. **66**(8): 3667–3672 (1977).
- [17] M. S. Lavine. *Drug delivery: A coat of many layers*. Science **293**: 1403 (2001).
- [18] P. Ball. *Window, clean thyself!*. Nature **377**: 290 (1995).
- [19] D. Jones. *Blaze of colour*. Nature **371**: 382 (1994).
- [20] D. Quéré. *Surface wetting: Model droplets*. Nature Materials **3**: 79 – 80 (2004).
- [21] T. Young. *An essay on the cohesion of fluids*. Phil. Trans. R. Soc. **95**: 65–87 (1805).
- [22] A. Dupré. *Theorie Mechanique de la Chaleur* (Gauthier–Villars, Paris, 1869).
- [23] J. G. Dash. *Clustering and percolation transitions in helium and other thin films*. Phys. Rev. B **15**(6): 3136 (1977).
- [24] C. Ebner. *Evidence for the roughening and wetting transitions in the lattice-gas model of adsorption from Monte Carlo simulations*. Phys. Rev. A **23**(4): 1925 (1981).
- [25] C. Ebner and W. F. Saam. *New phase-transition phenomena in thin argon films*. Phys. Rev. Lett. **38**(25): 1486–1489 (1977).
- [26] W. F. Saam and C. Ebner. *Classical fluid structure near solid substrates: A comparison of different theories*. Phys. Rev. A **17**(5): 1768–1773 (1978).
- [27] D. E. Sullivan. *Van der Waals model of adsorption*. Phys. Rev. B **20**(10): 3991–4000 (1979).
- [28] R. Pandit, M. Schick, and M. Wortis. *Systematics of multilayer adsorption phenomena on attractive substrates*. Phys. Rev. B **26**(9): 5112 (1982).
- [29] P. C. Ball and R. Evans. *Structure and adsorption at gas-solid interfaces: Lay-*
-

- ering transitions from a continuum theory.* J. Chem. Phys. **89**(7): 4412–4423 (1988).
- [30] K. Binder and D. P. Landau. *Wetting and layering in the nearest-neighbor simple-cubic Ising lattice: A Monte Carlo investigation.* Phys. Rev. B **37**(4): 1745–1765 (1988).
- [31] S. Dietrich and M. Napiórkowski. *Analytic results for wetting transitions in the presence of van der Waals tails.* Phys. Rev. A **43**(4): 1861–1885 (1991).
- [32] S. Dietrich and M. Schick. *Order of wetting transitions.* Phys. Rev. E **33**(7): 4952–4968 (1986).
- [33] M. E. Fisher and P. G. de Gennes. *Wall phenomena in a critical binary mixture.* C. R. Seances Acad. Sci., Ser. B **287**(8): 207–209 (1978).
- [34] D. Beysens. *Study of wetting and adsorption phenomena at fluid and fluid mixture interfaces.* In *Liquids at Interfaces (Les Houches Session XLVIII)*, (edited by J. Charvolin, J. F. Joanny, and J. Zinn-Justin), 499–548 (North Holland, Amsterdam, 1990).
- [35] D. Beysens and D. Estéve. *Adsorption phenomena at the surface of silica spheres in a binary liquid mixture.* Phys. Rev. Lett. **54**(19): 2123–2126 (1985).
- [36] R. Bennes, M. Privat, E. Tronel-Peyroz, and M. Amara. *Surface transition on silica and adsorbed layer thickness divergence near the coexistence curve of the silica-water-2,5-lutidine system.* Langmuir **7**(6): 1088–1090 (1991).
- [37] H. Sellami, A. Hamraoui, M. Privat, and R. Olier. *Experimental evidence of pure layering at the solid/liquid binary mixture interface. silica/water-2,5-dimethylpyridine system.* Langmuir **14**(9): 2402–2409 (1998).
- [38] A. Plech, U. Klemradt, M. Aspelmeyer, M. Huber, and J. Peisl. *Solid-liquid interface of a 2-propanol-perfluoromethylcyclohexane mixture: From adsorption to wetting.* Phys. Rev. E **65**: 061 604 (2002).
- [39] A. Plech, U. Klemradt, M. Huber, and J. Peisl. *Wetting transition of a binary liquid mixture at a solid boundary.* Europhys. Lett. **49**(5): 583 (2000).
- [40] A. Plech, U. Klemradt, and J. Peisl. *Wetting transition and pretransitional thin films in binary liquids: alcohol/perfluoromethylcyclohexane mixtures studied by x-ray reflectivity.* J. Phys.: Cond. Matt. **13**: 5563–5576 (2001).
- [41] J. Bowers, A. Zarbakhsh, H. K. Christenson, I. A. McLure, and R. Cubitt. *Adsorption from alkane+perfluoroalkane mixtures at fluorophobic and fluorophilic surfaces. I. Nature of the noncritical adsorption profiles.* J. Chem. Phys. **119**(22): 11 917–11 925 (2003).
- [42] J. Bowers, A. Zarbakhsh, A. Querol, H. K. Christenson, I. A. McLure, and R. Cubitt. *Adsorption from alkane+perfluoroalkane mixtures at fluorophobic and fluorophilic surfaces. II. Crossover from critical adsorption to complete wetting.* J. Chem. Phys. **121**(18): 9058–9065 (2004).
- [43] Y. Fan, J. E. Finn, and P. Monson. *Monte Carlo simulation study of adsorption from a liquid mixture at states near liquid-liquid coexistence.* J. Chem. Phys. **99**(10): 8238 (1993).
-

- [44] E. Kierlik, M. L. Rosinberg, Y. Fan, and P. A. Monson. *Prewetting at a liquid mixture-solid interface: A comparison of Monte Carlo simulations with mean field density functional theory*. J. Chem. Phys. **101**(12): 10 947–10 952 (1994).
- [45] K. Binder. *Spinodal decomposition in confined geometry*. J. Non-Equil. Thermody. **23**(1): 1–44 (1998).
- [46] K. Binder, S. Puri, and H. L. Frisch. *Surface-directed spinodal decomposition versus wetting phenomena: Computer simulations*. Faraday Discuss. **112**: 103–117 (1999).
- [47] S. Puri and K. Binder. *Surface-directed phase separation with off-critical composition: Analytical and numerical results*. Phys. Rev. E **66**: 061 602 (2002).
- [48] I. Hadjiagapiou and R. Evans. *Adsorption from a binary fluid mixture - the composite wetting film at the solid vapor interface*. Mol. Phys. **54**(2): 383–406 (1985).
- [49] M. M. Telo da Gama and R. Evans. *Adsorption and wetting transitions at a model of the interface between a solid and a binary fluid mixture*. Mol. Phys. **48**(4): 687 (1983).
- [50] F. Schmid and N. B. Wilding. *Wetting of a symmetrical binary fluid mixture on a wall*. Phys. Rev. E **63**(031201): 031 202–1–12 (2001).
- [51] J. R. Silbermann, D. Woywod, and M. Schoen. *Wetting of a selective solid surface by an asymmetric binary mixture*. Phys. Rev. E **69**(3): 031 606 (2004).
- [52] L. D. Gelb, K. E. Gubbins, R. Radhakrishnan, and M. Sliwinska-Bartkowiak. *Phase separation in confined systems*. Rep. Prog. Phys. **62**: 1573–1659 (1999).
- [53] R. E. Grim. *Clay mineralogy*. McGraw-Hill international Series in the earth and planetary sciences (McGraw-Hill, New York, 1968), 2nd edition.
- [54] J. N. Israelachvili. *Intermolecular and surface forces* (Academic Press, London etc., 1997), 2nd edition.
- [55] M. S. Dresselhaus. *Nanotubes: A step in synthesis*. Nature Materials **3**: 665 – 666 (2004).
- [56] S. Iijima and T. Ichihashi. *Single-shell carbon nanotubes of 1-nm diameter*. Nature **363**: 603–605 (1993).
- [57] R. M. de Vos and H. Verweij. *High-selectivity, high-flux silica membranes for gas separation*. Science **279**: 1710–1711 (1998).
- [58] A. T. Bell. *The impact of nanoscience on heterogeneous catalysis*. Science **299**: 1688–1691 (2003).
- [59] M. Djennad, D. Benachour, H. Berger, and R. Schomäcker. *Poly(vinyl alcohol) ultrafiltration membranes: Synthesis, characterization, the use for enzyme immobilization*. Eng. Life Sci. **3**(11): 446 – 452 (2003).
- [60] M. E. Davis. *Ordered porous materials for emerging applications*. Nature **417**: 813 – 821 (2002).
- [61] T. Hellweg, S. Schemmel, G. Rother, A. Brûlet, H. Eckerlebe, and G. H. Findenegg. *De-mixing dynamics of a binary liquid system in a controlled-pore glass*.
-

- Eur. Phys. J. E **12**: s01 (2003).
- [62] G. Rother, D. Woywod, M. Schoen, and G. H. Findenegg. *Confinement effect on the adsorption from a binary liquid system near liquid/liquid phase separation*. J. Chem. Phys. **120**(24): 11 864–11 873 (2004).
- [63] S. Schemmel, G. Rother, E. Eckerlebe, and G. H. Findenegg. *Local structure of a phase-separating binary mixture in a mesoporous glass studied by SANS*. J. Chem. Phys. (submitted).
- [64] Z. Zhuang, A. G. Casielles, and D. S. Cannell. *Phase diagram of isobutyric acid and water in dilute silica gel*. Phys. Rev. Lett. **77**(14): 2969–2972 (1996).
- [65] L. D. Gelb and K. E. Gubbins. *Liquid-liquid phase separation in cylindrical pores: Quench molecular dynamics and Monte Carlo simulations*. Phys. Rev. E **56**(3): 3185 (1997).
- [66] H. Greberg and G. N. Patey. *Demixing and the force between parallel plates immersed in binary liquid mixtures*. J. Chem. Phys. **114**(16): 7182–7188 (2001).
- [67] M. Sliwinska-Bartkowiak, R. Sikorski, S. L. Sowers, L. D. Gelb, and K. E. Gubbins. *Phase separations for mixtures in well-characterized porous materials: Liquid-liquid transitions*. Fluid Phase Equilib. **136**(1-2): 93–109 (1997).
- [68] M. Sliwinska-Bartkowiak, S. L. Sowers, and K. E. Gubbins. *Liquid-liquid phase equilibria in porous materials*. Langmuir **13**(5): 1182–1188 (1997).
- [69] A. J. Liu, D. J. Durian, E. Herbolzheimer, and S. Safran. *Wetting transitions in a cylindrical pore*. Phys. Rev. Lett. **65**(15): 1897–1900 (1990).
- [70] L. Monette, A. J. Liu, and G. S. Grest. *Wetting and domain-growth kinetics in confined geometries*. Phys. Rev. A **46**(12): 7664–7679 (1992).
- [71] L. D. Gelb and K. E. Gubbins. *Kinetics of liquid-liquid phase separation of a binary mixture in cylindrical pores*. Phys. Rev. E **55**(2): R1290–1293 (1997).
- [72] M. Y. Lin, S. K. Sinha, J. M. Drake, X.-I. Wu, P. Thiyagarajan, and H. B. Stanley. *Study of phase separation of a binary fluid mixture in confined geometry*. Phys. Rev. Lett. **72**(14): 2207–2210 (1994).
- [73] E. Kierlik, P. A. Monson, M. L. Rosinberg, L. Sarkisov, and G. Tarjus. *Capillary condensation in disordered porous materials: Hysteresis versus equilibrium behavior*. Phys. Rev. Lett. **87**(5): 055 701 (2001).
- [74] E. Kierlik, M. L. Rosinberg, G. Tarjus, and P. Viot. *Equilibrium and out-of-equilibrium (hysteretic) behavior of fluids in disordered porous materials: Theoretical predictions*. Phys. Chem. Chem. Phys. **3**: 1201–1206 (2001).
- [75] S. Klapp, H. Bock, D. J. Diestler, and M. Schoen. *Phase transformations in slit-pores: The role of metastable phases*. J. Phys.: Condens. Matter **14**: 5673–5697 (2002).
- [76] E. Paschinger, D. Levesque, G. Kahl, and J. J. Weis. *On the phase separation of a binary fluid in a porous medium*. Europhys. Lett. **55**(2): 178–183 (2001).
- [77] E. Schöll-Paschinger, D. Levesque, J. J. Weis, and G. Kahl. *Phase diagram of a symmetric binary fluid in a porous matrix*. Phys. Rev. E **64**: 011 502 (2001).
-

-
- [78] K. Bucior, A. Patrykiewicz, O. Pizio, and S. Sokołowski. *Capillary condensation of a binary mixture in slit-like pores*. J. Colloid Interface Sci. **259**(2): 209–222 (2003).
- [79] A. Martinez, O. Pizio, A. Patrykiewicz, and S. Sokołowski. *Phase behaviour of symmetric binary mixtures with partially miscible components in slit-like pores. Application of the fundamental measure density functional approach*. J. Phys.: Condens. Matter **15**: 2269–2283 (2003).
- [80] D. A. Lavis and G. M. Bell. *Statistical Mechanics of Lattice Systems: Closed-Form and Exact Solutions*, volume 1 (Springer, Berlin Heidelberg New York, 1999), 2nd edition.
- [81] H. Bock, D. J. Diestler, and M. Schoen. *Phase behavior of fluids confined between chemically decorated substrates*. J. Phys.: Condens. Matter **13**: 4697–4714 (2000).
- [82] L. Sarkisov and P. A. Monson. *Lattice model of adsorption in disordered porous materials: Mean-field density functional theory and Monte Carlo simulations*. Phys. Rev. E **65**(1): 011 202 (2001).
- [83] W. Fenz and R. Folk. *Binary mixtures of magnetic fluids*. Phys. Rev. E **67**: 021 507 (2003).
- [84] A. Patrykiewicz, L. Sałamacha, S. Sokołowski, H. Dominguez, and O. Pizio. *Phase behavior of lattice associating binary mixtures: A Monte Carlo study*. Phys. Rev. E **67**: 031 202 (2003).
- [85] J. Stirling. *Methodus differentialis, sive tractatus de summation et interpolation serierum infinitarum* (London, 1730), 1st edition.
- [86] W. A. Steele. *The Interaction of Gases with Solid Surfaces* (Pergamon, Oxford, 1974).
- [87] H. T. Davis. *Statistical Mechanics of Phases, Interfaces and Thin Films* (VCH, New York, Weinheim, Cambridge, 1996).
- [88] P. Ehrenfest. *Phase changes in the ordinary and extended sense classified according to the corresponding singularity of the thermodynamic potential*. Acad. Sci. Amsterdam **36**: 153–157 (1933).
- [89] A. B. Pippard. *Elements of Classical Thermodynamics* (C.U.P., Cambridge, UK, 1967).
- [90] M. E. Fisher. *Theory of equilibrium critical phenomena*. Rep. Prog. Phys. **30**: 257–272 (1967).
- [91] J. D. van der Waals. *Die Continuität des Gasförmigen und Flüssigen Zustandes*, volume 2 (Barth, Leipzig, 1899-1900), 2nd edition.
- [92] D. Furman, S. Dattagupta, and R. B. Griffiths. *Global phase diagram for a three-component model*. Phys. Rev. B **15**(1): 441–464 (1977).
- [93] L. Z. Boshkov. *On the description of closed-loop phase-diagrams of 2-component solutions, based on the one-fluid equation of state*. Doklady Akad. Nauk SSSR **294**(4): 901–905 (1987).
-

- [94] P. H. E. Meijer. *Influence of the chain-length of long molecules on the equation of state in binary gas-liquid mixtures*. J. Stat. Phys. **53**(1-2): 543–548 (1988).
- [95] A. van Pelt and T. W. de Loos. *Connectivity of critical lines around the van Laar point in t, x projections*. J. Chem. Phys. **97**(2): 1271–1281 (1992).
- [96] P. Clancy, K. E. Gubbins, and C. G. Gray. *Thermodynamics of polar liquid-mixtures*. Discuss. Faraday Soc. **66**: 116 (1978).
- [97] G. Jackson, J. S. Rowlinson, and C. A. Leng. *Phase equilibria in model mixtures of spherical molecules of different sizes*. J. Chem. Soc. Faraday Trans. 1 **82**(11): 3461–3473 (1986).
- [98] X. S. Chen and F. Forstmann. *The demixing and gas-liquid instability of a binary Yukawa fluid*. J. Chem. Phys. **97**(5): 3696–3703 (1992).
- [99] M. J. Blair and G. N. Patey. *Gas-liquid coexistence and demixing in systems with highly directional pair potentials*. Phys. Rev. E **57**(5): 5682–5686 (1998).
- [100] P. C. Hemmer and D. Imbro. *Ferromagnetic fluids*. Phys. Rev. A **16**(1): 380–386 (1977).
- [101] B. Groh and S. Dietrich. *Ferroelectric phase in Stockmayer fluids*. Phys. Rev. E **50**(5): 3814–3833 (1994).
- [102] H. Zhang and M. Widom. *Global phase diagrams for dipolar fluids*. Phys. Rev. E **49**(5): 3591–3593 (1994).
- [103] E. Lomba, J.-J. Weis, N. G. Almarza, F. Bresme, and G. Stell. *Phase transitions in a continuum model of the classical Heisenberg magnet: The ferromagnetic system*. Phys. Rev. E **49**(6): 5169–5178 (1994).
- [104] B. Groh and S. Dietrich. *Long-ranged orientational order in dipolar fluids-reply*. Phys. Rev. Lett **74**(13): R2617 (1995).
- [105] J. M. Tavares, M. M. Telo da Gama, P. I. C. Teixeira, J.-J. Weis, and M. J. P. Nijmeijer. *Phase diagram and critical behavior of the ferromagnetic Heisenberg fluid from density functional theory*. Phys. Rev. E **52**(2): 1915–1929 (1995).
- [106] J.-J. Weis, M. J. P. Nijmeijer, J. M. Tavares, and M. M. Telo da Gama. *Phase diagram of Heisenberg fluids: Computer simulation and density functional theory*. Phys. Rev. E **55**(1): 436–446 (1997).
- [107] A. Oukouiss and M. Baus. *Phase diagrams of the classical Heisenberg fluid within the extended van der Waals approximation*. Phys. Rev. E **55**(6): 7242–7252 (1997).
- [108] G. M. Range and S. H. L. Klapp. *Density functional study of the phase behavior of asymmetric binary dipolar mixtures*. Phys. Rev. E **69**: 041 201 (2004).
- [109] T. Bellini, M. Buscaglia, C. Chiccoli, F. Mantegazza, P. Pasini, and C. Zannoni. *Nematics with quenched disorder: What is left when long range order is disrupted*. Phys. Rev. Lett. **85**(5): 1008–1011 (2000).
- [110] Y. V. Kalyuzhnyi and G. Kahl. *Phase coexistence in polydisperse liquid mixtures: Beyond the van der Waals approximation*. J. Chem. Phys. **119**(14): 7335–7343 (2003).
-

-
- [111] G. M. Range and S. H. L. Klapp. *Demixing in simple dipolar mixtures: Integral equation versus density functional results*. Phys. Rev. E **70**: 031 201 (2004).
- [112] C. K. Hall and S. George. *Decorated-lattice model of magnetic or host-impurity systems*. Phys. Rev. B **11**(1): 224–238 (1975).
- [113] D. Roux, C. Coulon, and M. E. Cates. *Sponge phases in surfactant solutions*. J. Phys. Chem. **96**(11): 4174–4187 (1992).
- [114] D. Marx, P. Nielaba, and K. Binder. *Path-integral Monte Carlo study of a model adsorbate with internal quantum states*. Phys. Rev. B **47**(13): 7788–7804 (1993).
- [115] R. J. Baxter. *Exactly Solved Models in Statistical Mechanics*, volume 1 (Academic Press Inc., San Diego, CA 92101, 1990), 3rd edition.
- [116] G. Schneide. *Druckeinfluß auf die Entmischung flüssiger Systeme .4. Entmischung flüssiger n-Alkan-CO₂-Systeme bis 60 °C und 1500 bar. Messungen zum Problem der sog. Entmischung in der Gasphase*. Berich. Bunsen. Gesell. **70**(1): 10 (1966).
- [117] J. S. Rowlinson. *Liquids and liquid mixtures* (Butterworths, London, 1969), 2nd edition.
- [118] M. E. Fisher and M. C. Barbosa. *Phase boundaries near critical end points. I. Thermodynamics and universality*. Phys. Rev. B **43**: 11 177–11 184 (1991).
- [119] M. E. Fisher and P. J. Upton. *Universality and interfaces at critical end points*. Phys. Rev. Lett. **65**: 2402–2405 (1990).
- [120] X. S. Chen and F. Forstmann. *The phase instability of molecular fluid mixtures: dipolar and neutral hard spheres*. Molecular Phys. **76**(5): 1203–1211 (1992).
- [121] M. Chan, N. Mulders, and J. Reppy. *Helium in aerogel*. Physics Today 30–37 (1996).
- [122] D. J. Tulimieri, J. Yoon, and M. H. W. Chan. *Ordering of helium mixtures in porous gold*. Phys. Rev. Lett. **82**(1): 121–124 (1999).
- [123] P. G. de Gennes. *Wetting: statistics and dynamics*. Rev. Mod. Phys. **57**: 827 (1985).
- [124] S. Dietrich. In *Phase Transitions and Critical Phenomena*, (edited by C. Domb and J. L. Lebowitz), volume 12, 1 (Academic Press, London, 1988).
- [125] M. Schick. *Introduction to wetting phenomena*. In *Liquids at Interfaces (Les Houches Session XLVIII)*, (edited by J. Charvolin, J. F. Joanny, and J. Zinn-Justin), 415–498 (North Holland, Amsterdam, 1990).
- [126] R. Evans. *Microscopic theories of simple fluids and their interfaces*. In *Liquids at Interfaces (Les Houches Session XLVIII)*, (edited by J. Charvolin, J. F. Joanny, and J. Zinn-Justin), 1–98 (North Holland, Amsterdam, 1990).
- [127] D. Bonn and D. Ross. *Wetting transitions*. Rep. Prog. Phys **64**(9): 1085–1163 (2001).
- [128] D. M. Kroll, R. Lipowsky, and R. K. P. Zia. *Universality classes for critical wetting*. Phys. Rev. B **32**(3): 1862–1865 (1985).
-

-
- [129] M. P. Nightingale and J. O. Indekeu. *Examination of the necessity of complete wetting near critical-points in systems with long-range forces*. Phys. Rev. B **32**(5): 3364–3366 (1985).
- [130] C. Ebner and W. F. Saam. *Effect of long-range forces on wetting near bulk critical temperatures: An Ising-model study*. Phys. Rev. B **35**(4): 1822–1834 (1987).
- [131] E. Velasco and P. Tarazona. *Wetting and drying at a solid-fluid interface*. J. Chem. Phys. **91**(12): 7916–7924 (1989).
- [132] W. Fenzl. *Van der Waals interaction and wetting transitions*. Europhys. Lett. **64**(1): 64–69 (2003).
- [133] X. Zhang, D. Cao, and W. Wang. *The effect of discrete attractive fluid-wall interaction potentials on adsorption isotherms of Lennard-Jones fluid in cylindrical pores*. J. Chem. Phys. **119**(23): 12 586–12 592 (2003).
- [134] R. Lipowsky and U. Seifert. *Wetting by critical layers*. Phys. Rev. B **31**(7): 4701–4704 (1985).
- [135] L. Sigl and W. Fenzl. *Order-parameter exponent β_1 of a binary liquid mixture at a boundary*. Phys. Rev. Lett. **57**(17): 2191–2194 (1986).
- [136] D. Nicolaides and R. Evans. *Nature of the prewetting critical point*. Phys. Rev. Lett. **63**(7): 778–781 (1989).
- [137] D. E. Sullivan. *Interfacial density profiles of a binary van der Waals fluid*. J. Chem. Phys. **77**(5): 2632–2638 (1982).
- [138] P. Tarazona, M. M. Telo da Gama, and M. Robert. *Equilibrium structure of liquid wetting layers*. J. Chem. Phys. **86**(3): 1521–1532 (1987).
- [139] S. Dietrich and A. Latz. *Classification of interfacial wetting behavior in binary liquid mixtures*. Phys. Rev. B **40**(13): 9204–9237 (1989).
- [140] T. Getta and S. Dietrich. *Bulk and interfacial properties of binary liquid mixtures*. Phys. Rev. E **47**(3): 1856–1875 (1993).
- [141] R. Evans, J. M. Brader, R. Roth, M. Dijkstra, M. Schmidt, and H. Löwen. *Interfacial properties of model colloid-polymer mixtures*. Phil. Trans. R. soc. Lond. A **359**: 961–975 (2001).
- [142] B. M. Law. *Wetting, adsorption and surface critical phenomena*. Prog. Surf. Sci. **66**(6-8): 159–216 (2001).
- [143] A. Patrykiewicz, L. Sałamacha, S. Sokołowski, and O. Pisio. *Wetting behavior of associating binary mixtures at attractive walls: A lattice Monte Carlo study*. Phys. Rev. E **67**: 061 603 (2003).
- [144] S. Toxvaerd. *Molecular dynamics simulations of spinodal decomposition in films of binary mixtures*. Phys. Rev. Lett. **83**(25): 5318–5321 (1999).
- [145] S. Schemmel, D. Akcakayiran, G. Rother, A. Brulet, B. Farago, T. Hellweg, and G. H. Findenegg. *Phase separation of a binary liquid system in controlled-pore glass*. Mat. Res. Soc. Symp. Proc. **790**: P7.2.1 (2004).
- [146] H. Bohlen and M. Schoen. *Aspects of prewetting at nonplanar surfaces*. J.
-

- Chem. Phys. **120**(14): 6691–6700 (2004).
- [147] A. Martinez, A. Patrykiewicz, O. Pizio, and S. Sokołowski. *Phase diagrams for a binary mixture confined in narrow slitlike pores with energetically heterogeneous walls from a lattice mean-field approach*. J. Phys.: Condens. Matter **15**: 3107–3119 (2003).
- [148] K. Binder, M. M., and E. V. Albano. *Symmetric binary polymer blends confined in thin films between competing walls: Interplay between finite size and wetting behavior*. Phys. Chem. Chem. Phys. **3**: 1160–1168 (2001).
- [149] N. Choudhury and S. K. Ghosh. *Adsorption of Lennard-Jones fluid mixture in a planar slit: A perturbative density functional approach*. Phys. Rev. E **64**: 021 206 (2001).
- [150] J. Z. Tang and J. G. Harris. *Fluid wetting on molecularly rough surfaces*. J. Chem. Phys. **103**(18): 8201–8208 (1995).
- [151] K. Topolski, D. Urban, S. Brandon, and J. De Coninck. *Influence of the geometry of a rough substrate on wetting*. Phys. Rev. E **56**(3): 3353–3357 (1997).
- [152] J. De Coninck, S. Miracle-Solé, and J. Ruiz. *Is there an optimal substrate geometry for wetting?*. J. Stat. Phys. **100**(5-6): 981–997 (2000).
- [153] J. De Coninck, S. Miracle-Solé, and J. Ruiz. *Rigorous generalization of Young's law for heterogeneous and rough substrates*. J. Stat. Phys. **111**(1-2): 107–127 (2003).
- [154] C. Bruin. *Wetting and drying of a rigid substrate under variation of the microscopic details*. Physica A **251**(1-2): 81–94 (1998).
- [155] P. Bryk, D. Henderson, and S. Sokołowski. *The wetting transition associated with the adsorption of a gas on a rough surface*. Langmuir **15**(18): 6026–6034 (1999).
- [156] P. Bryk, O. Pizio, and S. Sokołowski. *Adsorption of a hard-sphere fluid in a slitlike pore with molecularly rough walls*. J. Chem. Phys. **109**(6): 2310–2315 (1998).
- [157] K. Rejmer and M. Napiórkowski. *Adsorption on a periodically corrugated substrate*. Phys. Rev. E **62**(1): 588–596 (2000).
- [158] G. P. Kubalski, M. Napiórkowski, and K. Rejmer. *The influence of substrate corrugation on wetting temperature*. J. Phys.: Condens. Matter **13**(21): 4727–4737 (2001).
- [159] S. Sacquin, M. Schoen, and A. Fuchs. *Fluids confined by nanopatterned substrates of low symmetry*. Mol. Phys. **100**(18): 2971–2982 (2002).
- [160] M. Schoen and S. Dietrich. *Structure of a hard-sphere fluid in hard wedges*. Phys. Rev. E **56**(1): 499–510 (1997).
- [161] R. J. Rowlinson and B. Eidom. *Molecular Theory of Capillarity* (Oxford University Press, Oxford, 1984).
- [162] H. E. Stanley. *Introduction to Phase Transitions and Critical Phenomena* (Oxford University Press, New York, 1971).
-

-
- [163] C. Ebner. *Film formation on a weakly attractive substrate within the lattice-gas model*. Phys. Rev. A **22**(6): 2776 (1980).
- [164] P. Roecken and P. Tarazona. *Capillary condensation in structured pores*. J. Chem. Phys. **105**(5): 2034 (1996).
- [165] P. Roecken, A. Somoza, P. Tarazona, and G. Findenegg. *Two-stage capillary condensation in pores with structured walls: A nonlocal density functional study*. J. Chem. Phys. **108**(20): 8689 (1998).
- [166] H. Bock and M. Schoen. *Phase behavior of a simple fluid confined between chemically corrugated substrates*. Phys. Rev. E **59**(4): 4122 (1999).
- [167] H. Bock and M. Schoen. *Thermomechanical properties of confined fluids exposed to a shear strain*. J. Phys.: Condens. Matter **12**: 1545 (2000).
- [168] H. Bock and M. Schoen. *Shear-induced phase transitions in fluids confined between chemically decorated substrates*. J. Phys.: Condens. Matter **12**: 1569 (2000).
- [169] A. Schreiber, H. Bock, M. Schoen, and G. H. Findenegg. *Effect of surface modification on the pore condensation of fluids: experimental results and density functional theory*. Mol. Phys. **100**(13): 2097–2107 (2002).
- [170] M. Schoen. *Capillary condensation between mesoscopically rough surfaces*. Colloids Surf. A **206**: 253–266 (2002).
- [171] A. Vishnyakov and A. V. Neimark. *Specifics of freezing of Lennard-Jones fluid confined to molecularly thin layers*. J. Chem. Phys. **118**(16): 7585–7598 (2003).
- [172] L. Sałamacha, A. Patrykiewicz, S. Sokołowski, and K. Binder. *The structure of fluids confined in crystalline slitlike nanoscopic pores: Bilayers*. J. Chem. Phys. **120**(2): 1017–1030 (2004).
- [173] E. Pitard, M. L. Rosinberg, and G. Tarjus. *Thermodynamics of fluids in disordered porous materials*. Mol. Simu. **17**: 399–419 (1996).
- [174] U. Marconi and F. van Swol. *Structure effects and phase-equilibria of Lennard-Jones mixtures in a cylindrical pore - a nonlocal density-functional theory*. Mol. Phys. **72**(5): 1081–1097 (1991).
- [175] A. Martinez, O. Pizio, and S. Sokołowski. *Phase behavior of symmetric binary mixture with partially miscible components in slitlike pores: Density functional approach*. J. Chem. Phys. **118**(13): 6008–6016 (2003).
- [176] A. Malijevsky, O. Pizio, A. Patrykiewicz, and S. Sokołowski. *Phase behavior of symmetric binary mixtures with partially miscible components in spherical pores. Density functional approach*. J. Mol. Liq. **112**(1-2): 81–89 (2004).
- [177] R. Salazar, R. Toral, and A. Chakrabarti. *Phase behavior of binary mixtures confined in a model aerogel*. J. Sol-Gel Sci. Techn. **15**(2): 175–181 (1999).
- [178] K. Bader and M. W. Roth. *Simulated behavior of krypton/argon mixtures confined between two graphite slabs: New terrain for familiar systems*. Surf. Sci. **538**(1-2): 30–44 (2003).
- [179] M. Cardenas and M. P. Tosi. *Wetting and demixing in a binary in a binary liquid*
-

- inside a disordered porous medium.* Physica B: **307**(1-4): 184–190 (2001).
- [180] E. Schöll-Paschinger, E. Gutleiderer, and G. Kahl. *The influence of thermodynamic self-consistency on the phase behaviour of symmetric binary mixtures.* J. Mol. Liq. **112**(1-2): 5–11 (2004).
- [181] J.-C. Lin and P. L. Taylor. *Exact results for phase separation in an asymmetric model of an interacting binary mixture.* Phys. Rev. E **49**(3): 2058–2061 (1994).
- [182] F. Formisano and J. Teixeira. *Appearance of critical fluctuations in a binary fluid mixture confined in vycor glass.* J. Phys.: Condens. Matter **12**(8A): 351–A356 (2000).
- [183] F. Formisano and J. Teixeira. *Critical fluctuations of a binary fluid mixture confined in a porous medium.* Eur. Phys. J. E **1**(1): 1–4 (2000).
- [184] M. M. Kohonen and H. K. Christenson. *Capillary condensation from vapors of n-hexane/perfluoro-n-hexane mixtures.* J. Phys. Chem. B **106**(26): 6685–6695 (2002).
- [185] P. G. De Gennes. *Liquid-liquid demixing inside a rigid network. Qualitative features.* J. Phys. Chem. **88**(26): 6469–6472 (1984).
- [186] H. Tanaka. *Wetting dynamics in a confined symmetric binary mixture undergoing phase separation.* Phys. Rev. Lett. **70**(18): 2770–2773 (1993).
- [187] M. Tasinkevych and A. Ciach. *Lattice model results for lamellar phases in slits.* Phys. Rev. E **60**(6): 7088–7097 (1999).
- [188] J. Candia and V. Albano. *Irreversible growth of a binary mixture confined in a thin film geometry with competing walls.* Phys. Rev. Lett. **88**(1): 016 103 (2002).
- [189] H. Furukawa. *Dynamic-scaling theory for phase-separating unmixing mixtures: Growth rates of droplets and scaling properties of autocorrelation functions.* Physica A **123**(2-3): 497–515 (1984).
- [190] P. Wiltzius and A. Cumming. *Domain growth and wetting in polymer mixtures.* Phys. Rev. Lett. **66**(23): 3000–3003 (1991).
- [191] G. Krausch, C.-A. Dai, and E. J. Kramer. *Real space observation of dynamic scaling in a critical polymer mixture.* Phys. Rev. Lett. **71**(22): 3669–3672 (1993).
- [192] R. Valiullin and I. Furó. *Phase separation of a binary liquid mixture in porous media studied by nuclear magnetic resonance cryoporometry.* J. Chem. Phys. **116**(3): 1072–1076 (2002).
- [193] B. Cui, B. Lin, and S. A. Rice. *Structure and phase transitions in confined binary colloid mixtures.* J. Chem. Phys. **119**(4): 2386–2398 (2003).
- [194] S. B. Dierker and P. Wiltzius. *Statics and dynamics of a critical binary fluid in a porous medium.* Phys. Rev. Lett. **66**(9): 1185–1188 (1991).
- [195] K. P. Travis and K. E. Gubbins. *Transport diffusion of oxygen-nitrogen mixtures in graphite pores: A nonequilibrium molecular dynamics (NEMD) study.* Langmuir **15**: 6050–6059 (1999).
-

- [196] R. Valiullin and I. Furó. *Low-temperature phase separation of a binary mixture in porous materials studied by cryoporometry and pulsed-field-gradient NMR*. Phys. Rev. E **66**: 031 508 (2002).
- [197] P. Gallo, P. R., and M. Rovere. *Single particle dynamics of a confined Lennard-Jones mixture in the supercooled regime*. Physica A **314**(1-4): 530–538 (2002).
- [198] P. Gallo, R. Pellarin, and M. Rovere. *Slow dynamics of a confined supercooled binary mixture. II. Q space analysis*. Phys. Rev. E **68**: 061 209 (2003).
- [199] C. R. Kamala, K. G. Ayappa, and S. Yashonath. *Distinct diffusion in binary mixtures confined in slit graphite pores*. J. Phys. Chem. B **108**: 4411–4421 (2004).
- [200] M. Kotelyanski and S. K. Kumar. *Surface transitions for confined associating mixtures*. Phys. Rev. Lett. **80**(6): 1252–1255 (1998).
- [201] F. Clarysse and C. J. Boulter. *Microscopic origin and relevance of surface parameters for confined ternary mixtures*. Physica A **303**(3-4): 295–307 (2002).
- [202] S. D. Overduin and G. N. Patey. *Forces between chemically patterned plates immersed in binary liquid mixtures*. J. Chem. Phys. **117**(7): 3391–3397 (2002).
- [203] K. Kanamori, K. Nakanishi, K. Hirao, and H. Jinnai. *Three-dimensional observation of phase-separated silica-based gels between parallel plates*. Langmuir **19**: 5581–5585 (2003).
- [204] B. J. Frisken, A. J. Liu, and D. S. Cannell. *Critical fluids in porous media*. MRS Bulletin **19**(5): 19–24 (1994).
- [205] D. A. Weitz. *Mesomorphic disorder*. MRS Bulletin **19**(5): 11–12 (1994).
- [206] G. Rother. *Adsorption und Phasentrennung binärer flüssiger Mischungen in Porensystemen*. PhD dissertation, Fakultät II, Technische Universität, Berlin, Germany (2002).
- [207] S. Schemmel. *Struktur und Dynamik flüssiger Mischungen in mesoporösen Gläsern: Untersuchungen mit Neutronenstreuverfahren*. PhD dissertation, Fakultät II, Technische Universität, Berlin, Germany (2004).
- [208] A. Hirtz, K. Bonkhoff, and G. H. Findenegg. *Optical studies of liquid interfaces in amphiphilic systems - how wetting and adsorption are modified by surfactant aggregation*. Adv. Coll. Interface Sci. **44**: 241–281 (1993).
- [209] J. Schulz, J. Bowers, and G. H. Findenegg. *Crossover from preferential adsorption to depletion: Aqueous systems of short-chain C_nE_m amphiphiles at liquid/liquid interfaces*. J. Phys. Chem: B **105**(29): 6956–6964 (2001).
- [210] J. R. Howse, E. Manzanares-Papayanopolous, I. A. McLure, J. Bowers, R. Steitz, and G. H. Findenegg. *Critical adsorption and boundary layer structure of 2-butoxyethanol + D_2O mixtures at a hydrophilic silica surface*. J. Chem. Phys. **116**(16): 7177–7188 (2002).
- [211] H. Grull and D. Woermann. *Preferential adsorption on porous glass near the liquid/liquid coexistence curve of a binary liquid mixture*. J. Chem. Phys. **105**(6): 2527–2532 (1996).
-

- [212] H. Gröll and D. Woermann. *Adsorption on hydrophobic porous glass near the liquid/liquid coexistence curve of a binary liquid mixture*. J. Chem. Phys. **106**(2): 732–737 (1997).
- [213] K. Kaneko. In *Adsorption and its Application to Industry and Environmental Protection: Surface Science and Catalysis*, (edited by A. Dobrowski), volume 2 (Elsevier, Amsterdam, 1998).
- [214] S. Gross. PhD dissertation, Fakultät II, Technische Universität, Berlin, Germany (1997).
- [215] P. A. Webb and C. Orr. *Analytical methods in fine particle technology*. Micromeritics Instrument Corp. (1997).
- [216] L. Peliti and S. Leibler. *Strong adsorption in critical binary mixtures*. J. Phys. C **16**(13): 2635–2640 (1983).
- [217] E. Gulari, B. Chu, and D. Woermann. *Critical exponents of a fluid mixture in the presence of isotope exchange: Isobutyric acid/D₂O*. J. Chem. Phys. **73**(5): 2480–2488 (1980).
- [218] P. Gansen and D. Woermann. *Phase diagram of a ternary fluid mixture in the vicinity of its critical line in the presence of isotope-exchange reactions*. J. Phys. Chem. **88**: 2655–2660 (1984).
- [219] L. S. Ornstein and F. Zernike. Physik. Z. **27**: 761 (1926).
- [220] P. Debye, H. R. Anderson, and H. Brumberger. *Scattering by an inhomogeneous solid II, the correlation function and its application*. J. Appl. Phys. **28**: 679 (1957).
- [221] G. Porod. *Die Röntgenkleinwinkelstreuung von dichtgepackten kolloiden Systemen .I.* Kolloid Z. **124**(2): 83–114 (1951).
- [222] V. F. Sears. *Neutron scattering lengths and cross sections*. Neutron News **3**: 26 (1992).
- [223] P. Tarazona. *Fundamental measure theory and dimensional interpolation for the hard spheres fluid*. Physica A **306**: 243–250 (2002).
- [224] C. Spöler and S. H. L. Klapp. *Phase behavior of stockmayer fluids confined to a nonpolar porous material*. J. Chem. Phys. **118**(8): 3628–3638 (2003).
- [225] J. Sommerfeld. *Phasenverhalten von Fluiden zwischen chemisch-dekorierten Substraten*. Diploma thesis, Fakultät II, Technische Universität, Berlin, Germany (2004).
-

Publications

- D. Woywod and M. Schoen, *Phase behavior of confined symmetric binary mixtures*.
Phys. Rev. E **67**(2): 026122 (2003).
- J. R. Silbermann, D. Woywod, and M. Schoen, *Wetting of a selective solid surface by an asymmetric binary mixture*.
Phys. Rev. E **69**(3): 031606 (2004).
- G. Rother, D. Woywod, M. Schoen, and G. H. Findenegg, *Confinement effect on the adsorption from a binary liquid system near liquid/liquid phase separation*.
J. Chem. Phys. **120**(24): 11864 (2004).
- D. Woywod and M. Schoen, *The wetting of planar solid surfaces by symmetric binary mixtures near bulk gas-liquid coexistence*.
J. Phys.: Condens. Matter **16**(28): 4761 (2004).
- D. Woywod, S. Schemmel, G. Rother, G. H. Findenegg, and M. Schoen, *Phase behavior and local structure of a binary mixture in pores: Mean-field lattice model calculations for analyzing neutron scattering data*.
J. Chem. Phys.: (accepted 2005).

Dank

Die vorliegende Arbeit wäre sicher nicht zustande gekommen ohne die Unterstützung und Geduld vieler Menschen, von denen ich nur einige im Besonderen aufzählen kann.

Meinem Doktorvater Prof. Martin Schoen danke ich für seine Betreuung, die mir stets genügend Freiraum ließ, für seine fachliche Hilfe und Geduld, die auch bei der einen oder anderen Irrung meinerseits niemals abnahm, und schließlich für seine stete Unterstützung, die während meiner gesamten Promotionszeit substanziell war.

Ich danke Prof. Gerhard H. Findenegg für seine Bereitschaft, Neugier und Geduld, theoretische Erkenntnisse mit experimentellen Daten zu verbinden, was ohne seinen Weitblick und seine Erfahrung nicht erfolgreich gelungen wäre.

Dr. Sabine H. L. Klapp hat mir während der ganzen Zeit immer wieder wichtige Denkanstöße und Anregungen gegeben, wofür ich mich sehr bei ihr bedanke. Für die herzliche Gastfreundschaft in Madrid sowie für die Einführung in die Dichtefunktionaltheorie bin ich Prof. Pedro Tarazona zu Dank verpflichtet. Weiterhin hat mir Prof. Peter Monson in Fragen des Benetzungsverhaltens viele wichtige Ratschläge gegeben und mich vor einigen Irrtümern bewahrt. Auf jeden Fall habe ich auch Prof. Dennis Diestler zu danken, der immer ein offenes Ohr für meine Arbeiten hatte und mir hinsichtlich der englischen Sprache viel geholfen hat.

Mein besonderer Dank gilt Gabriel Range für die unendliche Geschichte der einfachen Mischungen im Volumen. Weitere Kooperationen wären nahezu unmöglich gewesen, wenn nicht Jörg Silbermann, Gernot Rother und Sebastian Schemmel großen Einsatz und Motivation an den Tag gelegt hätten. Ich bedanke mich auch bei Holger Bohlen und Carsten Spöler für die gewohnt freundschaftliche Atmosphäre und das Vertrauen innerhalb der Arbeitsgruppen.

Meiner Familie, insbesondere meinen Eltern, Jana und Daniel danke ich für die allgegenwärtige Unterstützung und ihren Glauben an die Richtigkeit meines Tuns. Für die Festigkeit des sozialen Netzes, in welches ich stets weich fallen konnte, leisteten meine Freunde einen riesigen Beitrag. Ich bedanke mich bei ihnen, besonders bei Jörn, Micha, Jochen, Toady, Peter, Igor und Punk-Micha. Natürlich und zu guter Letzt bin ich Maika zu großem Dank verpflichtet für ihre Energie, ihr Interesse und ihr Dasein in allen Momenten.

I thank you.
